

Microwave Imaging for Stroke Diagnostics

Zur Erlangung des akademischen Grades eines

DOKTOR-INGENIEURS

von der Fakultät für

Elektrotechnik und Informationstechnik

des Karlsruher Instituts für Technologie (KIT)

genehmigte

DISSERTATION

von

Jochen Schmid, Dip.-Ing.

geb. in Tuttlingen

| | |
|-----------------------------|---------------------------------|
| Tag der mündlichen Prüfung: | 22. November 2016 |
| Referent: | Prof. Dr. rer. nat. Olaf Dössel |
| Korreferent: | Prof. Dr.-Ing. Thomas Zwick |



This document is licensed under the Creative Commons Attribution –
Share Alike 3.0 DE License

(CC BY-SA 3.0 DE): <http://creativecommons.org/licenses/by-sa/3.0/de/>

Zusammenfassung

In den vergangenen Jahren wurden technische Möglichkeiten studiert, die es in Zukunft ermöglichen könnten, die Hirnschlag Diagnose schon in der Ambulanz, also mobil durchzuführen. Dies wäre von großem Nutzen für alle Patienten die einen Schlaganfall erleiden, da die Behandlung ohne eine sichere Diagnose nicht begonnen werden kann. Als Standardtherapie wird beim häufigsten Typ, dem ischämischen Schlaganfall, eine Thrombolysetherapie durchgeführt. Diese muss aber in den ersten 4,5 Stunden erfolgen, da sonst keine Vorteile mehr erzielt werden können. Zudem gilt: Umso früher die Therapie begonnen wird, umso besser die Prognose.

Eine gute Möglichkeit, diese frühe Diagnose zu erreichen könnte hier die Mikrowellentechnologie sein, denn die dafür nötige Hardware wäre äußerst kompakt. Die Diagnose mittels Mikrowellen erfordert “nur” eine Anordnung von Antennen, ein Messsystem und einen leistungsstarken Computer für die Auswertung.

Damit diese Technologie aber erfolgreich eingesetzt werden kann, muss zuvor ein Diagnosealgorithmus entwickelt werden, der die Anforderungen erfüllt. Damit eine Thrombolyse angewendet werden kann, muss zweifelsfrei eine Blutung ausgeschlossen werden können. Da hierfür nicht zwingend eine Bildgebung erforderlich ist, wurde als ein erster Algorithmus ein einfacher Beamforming-Algorithmus getestet. Vorteil dieser Art von Algorithmen ist, dass sie enorm schnell Ergebnisse liefern können. Oft ist in weniger als einer Minute ein Resultat verfügbar. Da dieser Algorithmus aber nicht die nötige Robustheit unter den vorhandenen Bedingungen liefern kann, wurde ein zweiter Algorithmus auf Eignung getestet.

Der zweite Algorithmus nutzte die Gauss-Newton-Methode und FDTD Vorwärtsrechnungen um die Permittivitätsverteilung zwischen den Antennen zu rekonstruieren. Da dieser iterative Prozess aber bis zu eine Woche Rechenzeit für ein Ergebnis benötigte, wurde noch ein dritter Algorithmus implementiert.

Der letzte Algorithmus, *Contrast Source Inversion* genannt, verzichtet auf Vorwärtsrechnungen und verwendet anstelle dessen die Lippmann-Schwinger-Gleichung um das Feld und den zuvor definierten Kontrast unter Zuhilfenahme von sogenannten Kontrastquellen zu rekonstruieren. Als Kontrast wird hierbei eine Größe, berechnet aus der Permittivität des Hintergrundmaterials und der lokal gültigen Permittivität, bezeichnet.

Alle betrachteten Algorithmen zeigten eine potentielle Eignung zur Schlaganfalldiagnose, allerdings wurden am Ende zwei aufgrund ihrer Nachteile verworfen. Die *Contrast Source Inversion* erscheint geeignet und nach weiterer Erforschung in der Lage, alle Bedingungen zu erfüllen.

Danksagungen

An dieser Stelle möchte ich allen Kollegen und Mitarbeitern am Institut für Biomedizinische Technik für ihre Unterstützung danken. Vor allem danke ich aber Herrn Professor Dr. rer. nat. Olaf Dössel für die hervorragende Betreuung. Mein Dank gilt auch meinen Studenten, die mich in meiner Dissertation, mit ihren Beiträgen unterstützt haben. Des Weiteren möchte ich Herrn Professor Dr.-Ing. Thomas Zwick vom Institut für Hochfrequenztechnik und Elektronik für die Übernahme des Korreferats danken.

Außerdem danke ich den Mitarbeitern am Institut für Hochfrequenztechnik und Elektronik für ihr mitwirken. Ebenfalls dankbar bin ich für die Arbeiten, die an den Werkstätten am Institut für Biomedizinische Technik sowie am Institut für Hochfrequenztechnik und Elektronik geleistet wurden. Ich danke auch ganz herzlich meiner Frau für die Unterstützung in dieser Zeit. Ein besonderen Dank auch an alle, die diese Arbeit Korrektur gelesen haben.

– Vielen Dank, euch allen –

Contents

| | |
|--|------------|
| Abstract | i |
| Acknowledgments | iii |
| 1 Introduction | 1 |
| 1.1 About This Work | 3 |
| <hr/> | |
| I Fundamentals | 5 |
| <hr/> | |
| 2 Propagation of Electromagnetic Waves | 7 |
| 2.1 Maxwell Equations | 8 |
| 2.2 Electromagnetic Waves | 10 |
| 2.3 Waves in Complex Materials | 12 |
| 2.4 Scattering Problem of Electromagnetic Waves | 16 |
| 3 The Human Head under Microwave Exposure for Microwave Imaging | 17 |
| 3.1 Microwave Imaging | 17 |
| 3.2 Human Head Anatomy and Effects on Microwaves | 18 |
| 3.3 Stroke Disease | 21 |
| 4 Optimization | 25 |
| 4.1 Newton-Raphson Method | 26 |
| 4.2 Line Search Procedure | 29 |
| 4.3 Conjugate Gradient Methods | 31 |

| | | |
|-----------|--|------------|
| II | Methods and Results | 33 |
| 5 | Basic Signal Analysis | 35 |
| 6 | Permittivity Phantom of the Human Head | 41 |
| 6.1 | Selection of the Materials | 42 |
| 6.2 | Development of the Phantom | 48 |
| 6.3 | A Mold to Form the Phantom | 53 |
| 6.4 | Phantom Verification | 55 |
| 7 | Three Algorithms for Stroke Diagnosis | 63 |
| 7.1 | Delay and Sum Beamforming for Microwave Imaging | 64 |
| 7.2 | Blackbox Reconstruction with a Gauss-Newton Optimization | 89 |
| 7.3 | Contrast Source Inversion for Stroke Imaging | 104 |
| 8 | Conclusion | 139 |
| 9 | Outlook | 141 |
| A | The Complex Root of the Permittivity | 145 |
| B | The G Operators of CSI | 147 |
| B.1 | Calculation Time | 149 |
| C | Differentiation of the MR Term | 151 |
| | References | 155 |
| | List of Publications and Supervised Theses | 161 |

Introduction

Heinrich Hertz was the first who showed that freely propagating electromagnetic waves really exist. His experiments in 1886 opened the door to a new age of telecommunication and global connectivity. Neither radio nor wireless LAN would be possible without electromagnetic waves. Since Dr. Hertz's first experiments a lot of new applications for electromagnetic waves have been introduced. We use them to locate objects on earth and space, to heat our meals and stay linked to colleagues and friends.

Year by year a great number of new ways on how to use electromagnetic waves are discovered. However, according to experts these electromagnetic waves can also be applied in the medical sector.

Microwave imaging is such a medical application and it is subject of current research programs. The interest on microwave imaging has steadily been growing over the last decades. One of the reasons for this is the fact that the necessary hardware can be produced in a very compact and cheap way. Due to the compact components necessary for such a device, the device will be applicable in a mobile way. In addition to that as a diagnostic medium microwaves are known to be non-harmful, if the power radiated by such a system is limited to a non-harmful level.

Assuming that microwaves could potentially penetrate the human head, an imaging technology based on them could improve the treatment and medical outcome of victims with acute cerebral diseases, such as strokes.

It is fact that the medical treatment of cerebral strokes is bound to a temporal limit. Medical course books offer a limit in time with a maximum of 4.5 *h*. If the medication is not started during this period of time nothing can be done to improve the health outcome after an ischemic stroke [1, 2]. Additionally, it is important to start the treatment as soon as possible. Among experts this fact is called “time is brain”. – So why not starting the medication right away? However, if there was an intracranial bleeding the thrombolytic drugs would have awful consequences and could lead to the death of the victim. This is the reason why a treatment is not advisable until the cause of the stroke is 100 % clarified.

A short glance at the statistics is enough to note that strokes are still one of the major causes of death world wide. In 2012, strokes appear on the second place, with a total of 6.7 million people, in statistics published by the World Health Organization (WHO) [3]. Even in countries with well-developed health systems and a good availability of stroke units like Germany, strokes remain one of the main causes of death and disability (until today it is still on the top ten list of death causes).

Stroke is a serious disease and even if the death of victims could be prevented, late complications are often linked with further problems such as disabilities and long periods of rehabilitation.

Due to likewise compact devices, microwave imaging will have the potential to be used in ambulances and thus could help to improve the medical outcome of stroke victims.

Facing the facts the growing interest in microwave imaging is not a surprise.

The project with the farthest development is the Strokefinder, a product of the company Medfield Diagnosis. The device (Strokefinder) is mostly build on the findings of A. Fhager. The decision of a hemorrhage existence is made by a computer learning algorithm. Detailed information is not accessible, as the device is supposed to be a product [4].

Another device, named MARIA and produced by the company Mircrima, was originally based on research projects of the University of Bristol. It is as well as the Strokefinder already involved in clinical studies [5].

The researcher group of the university of Queensland should also be mentioned here. They are working on a technology which is based on microwaves to diagnose strokes and they published some interesting papers about phantoms [6].

1.1 About This Work

During the last four years hardware and software were introduced to examine algorithms as well as measurement techniques. They were verified and their limitations as well as their applicability on microwave-based stroke-imaging systems were examined. In total three algorithms were implemented. In addition to that a phantom for experimental measurements was developed and arrays for different purposes were introduced.

The first part of this thesis offers the very basic physical fundamentals, followed by a short chapter about some anatomical details of the human head and their fundamental influences on microwaves and finally a chapter about the basic mathematical algorithms used to reconstruct the images.

The second part starts with a chapter about the signal we can expect and a few preliminary studies of the problem. The second chapter is about the developed gelatin-sugar-water phantom and the last chapter is about the three implemented and tested algorithms. The first section of this chapter is about the so-called Delay And Sum (DAS) beamformer. The following section describes the investigation of the Gauss-Newton-based black-box inversion and the last section of that chapter is about the Contrast Source Inversion (CSI) algorithm and its usability on diagnosing strokes.

Since no strict separation between the methods and the results was possible, each section describing an algorithm starts with a detailed description of the method and ends with the achieved results.

Chapters on conclusions and outlook finalize this thesis.

PART I

FUNDAMENTALS

Propagation of Electromagnetic Waves

As microwaves are the basic medium employed in this thesis, this chapter is offering some basic natures of them.

In the case of microwave imaging a so called stimulus signal (a known signal) is transmitted from one sending antenna to a set of receiving antennas (sometimes including the sending antenna). By traversing the object under examination the wave is collecting information about the structural morphology and also about the current condition of the object. In the case of stroke-imaging the information which is of interest is the health condition of the brain tissues. However, the information achieved by a measurement with a microwave system contains much more information; for example about the head, the brain itself and even about the measurement system itself. This chapter briefly overviews the peculiarity of propagating waves to understand how the content of the information could be extracted later.

2.1 Maxwell Equations

The Maxwell equations are the fundamental definitions which hold for every electromagnetic field problem.

$$\nabla \cdot \mathbf{D} = \rho \quad (2.1)$$

$$\nabla \cdot \mathbf{B} = 0 \quad (2.2)$$

$$\nabla \times \mathbf{E} + \frac{\partial \mathbf{B}}{\partial t} = 0 \quad (2.3)$$

$$\nabla \times \mathbf{H} = \mathbf{J} + \frac{\partial \mathbf{D}}{\partial t} \quad (2.4)$$

With D , the electric displacement field, ρ , the charge density, H , the magnetic field, J , current density, E , the electric field and t for the time [7]. Knowing the materials properties (namely the polarization P and the magnetization M) every electromagnetic field problem with defined boundary conditions can be solved by finding a solution for this system of coupled partial differential equations. This is often not an easy task, and in most of the cases there even does not exist a closed solution at all. The only option to deal with such circumstances is to approximate the underlying problem and its solution. A common way to deal with differential equations is to approximate them numerically, by the method of finite differences.

2.1.1 Numerical Approximation of the Differential Equations

One of the oldest numerical approximations for electromagnetic field problems is the Finite Difference Time Domain (FDTD) method. As the name suggests this method approximates the derivatives by finite differences. This can be done by defining a sufficiently small step Δx and take the result of the approximated function Θ around the point of interest x . The approximated derivative at x for example can be written as

$$\frac{\partial \Theta}{\partial x} \approx \frac{\Theta(x + \Delta x) - \Theta(x)}{\Delta x}. \quad (2.5)$$

This in that way defined approximation of the derivative is called the forward difference. Two other such definitions exist, the backward difference

$$\frac{\partial \Theta}{\partial x} \approx \frac{\Theta(x) - \Theta(x - \Delta x)}{\Delta x} \quad (2.6)$$

and the central

$$\frac{\partial \Theta}{\partial x} \approx \frac{\Theta(x + \Delta x) - \Theta(x - \Delta x)}{2\Delta x}. \quad (2.7)$$

All finite difference methods are based on at least one of these approximations. Higher order derivatives can be derived by combining these difference operators.

2.1.1.1 Finite Difference Time Domain

It was Kane S. Yee who first defined a scheme to discretize the fields and solve Maxwell's equation numerically. He introduced the lattice shown in Figure 2.1. Since the components of the fields are calculated on different points, a separate calculation of the electric and the magnetic fields are possible.

This lattice is up to today the standard when models are discretized for Finite Difference Time Domain (FDTD) calculations.

Limitations Certain side conditions must be fulfilled, which are mainly set by the maximal wavelength, which is included in the set up simulation.

To achieve representative results with FDTD-simulations a maximum time step Δt , that fulfills the following inequality

$$\Delta t \leq \frac{1}{u \sqrt{\frac{1}{(\Delta x)^2} + \frac{1}{(\Delta y)^2} + \frac{1}{(\Delta z)^2}}}, \quad (2.8)$$

must be used. Here u denotes the velocity of propagation and Δx , Δy and Δz are the spatial dimensions of the smallest element of the grid of the simulation.[9]

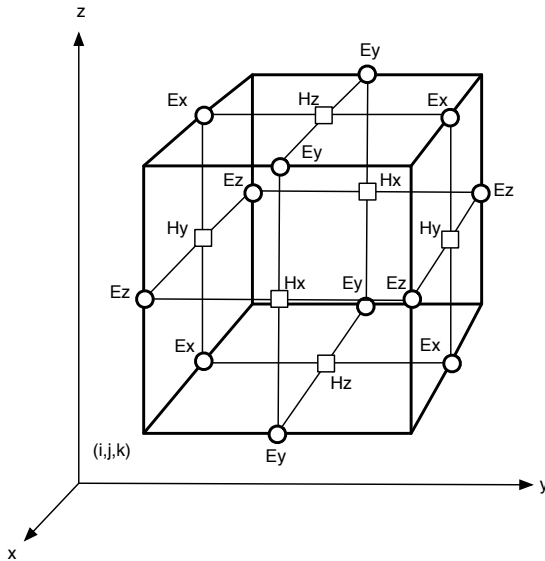


Figure 2.1: Lattice defined by Yee 1966. It shows various positions of field components. The components of the electric field (○) are calculated in the middle of the edges and the components of the magnetic field (□) centered on the surfaces [8].

2.1.1.2 Finite Difference Frequency Domain

The Finite Difference Frequency Domain (FDFD) method is also based on the grid defined by Yee for the FDTD method. In this method it is not needed to calculate multiple time steps to achieve a solution. The method is used to approximate a direct solution of Maxwell's curl equation at frequency domain. By using central differences to approximate the second-order-spatial derivatives it leads to a system of linear equations that can be represented by a sparse matrix. The linear system can then be solved by an iterative method, for example the biconjugate gradient method. [10, 11]

2.2 Electromagnetic Waves

An expanding time dynamic electric field in coherence with a time dynamic magnetic field is called an electromagnetic wave. All electromagnetic

fields and thus all electromagnetic waves depend on the fundamental rules formulated by Maxwell (2.1 -2.4).

Maxwell's equations can be decoupled by taking the curl of Faraday's Law (2.3) and Ampère's Law (2.4) at free space. An equation depending on the electric field can be derived from Faraday's Law by

$$\nabla \times \nabla \times \mathbf{E} = \nabla \times \left(-\frac{\partial \mathbf{B}}{\partial t} \right). \quad (2.9)$$

This can also be written as

$$\nabla(\nabla \cdot \mathbf{E}) - \nabla^2 \mathbf{E} = -\frac{\partial}{\partial t} (\nabla \times \mathbf{B}). \quad (2.10)$$

With Ampère's Law

$$\nabla \times \mathbf{B} = \mu_0 \epsilon_0 \frac{\partial \mathbf{E}}{\partial t} \quad (2.11)$$

and Gauss's Law

$$\nabla \cdot \mathbf{E} = 0 \quad (2.12)$$

in free space the decoupled equation is

$$\nabla^2 \mathbf{E} = \mu_0 \epsilon_0 \frac{\partial^2 \mathbf{E}}{\partial t^2}. \quad (2.13)$$

The achieved equation is now easily identified as wave equation¹. The propagation speed of the wave is then $1/\sqrt{\mu_0 \epsilon_0} = c_0$ (the speed of light). The equation depending on the magnetic field can be deduced in a similar way [7]. As only the electric field is of interest later, just these equations are offered here.

If only time harmonic problems are considered the equation (2.13) can be simplified as

$$\nabla^2 \mathbf{E} = -\omega^2 \mu_0 \epsilon_0 \mathbf{E}. \quad (2.14)$$

Here it should be noted that this equation is equal to the Helmholtz equation² and sometimes also called that way in literature.

¹Generally, a wave equation is a differential equation of the form $\frac{\partial^2 f}{\partial t^2} = v^2 \Delta f$ with Δ the Laplace operator, $f(t, \mathbf{x})$ an arbitrary function of time t and space (e.g. $\mathbf{x} \in \mathbb{R}^2$)

²The Helmholtz equation is a partial differential equation of the form $\nabla^2 \mathbf{A} + v^2 \mathbf{A} = 0$

2.2.1 Green's Functions

A fundamental solution considering the necessary boundary constraints in connection with the principle of superposition for electromagnetic fields is a powerful tool to solve more complex problems. Such fundamental solutions are also called Green's functions. The three-dimensional fundamental solution for an infinite small monochromatic point source at free space is

$$g(\mathbf{r}, t) = \frac{1}{4\pi \cdot |\mathbf{r}|} e^{i(k_0|\mathbf{r}| - \omega t)} \quad (2.15)$$

and the two-dimensional solution is known to be

$$g(\mathbf{r}, t) = \frac{-i}{4} H_0^{(2)}(k_0|\mathbf{r}| - \omega t). \quad (2.16)$$

Here \mathbf{r} is a vector and $|\mathbf{r}| = \sqrt{x^2 + y^2 + z^2}$ or $|\mathbf{r}| = \sqrt{x^2 + y^2}$ at two-dimensions, $k = \frac{2\pi}{\lambda}$ is the wave number in free space, $\omega = 2\pi f$ is the angular frequency and $H_0^{(2)}$ denotes the zero-order Hankel function of the second kind. The complex unit is i and the time is denoted by t .

The term ωt in both equation can be neglected if only time harmonic problems are regarded. Important equations for later examinations are

$$g(\mathbf{r}) = \frac{1}{4\pi \cdot |\mathbf{r}|} e^{i(k_0|\mathbf{r}|)} \quad (2.17)$$

and

$$g(\mathbf{r}) = \frac{-i}{4} H_0^{(2)}(k_0|\mathbf{r}|). \quad (2.18)$$

Both equations for time harmonic problems are satisfying the Helmholtz equation in $\mathbb{R}^3/\mathbf{0}$ and in $\mathbb{R}^2/\mathbf{0}$ respectively.

2.3 Waves in Complex Materials

Influencing effects on an electromagnetic wave, whenever propagating through homogeneous matter, are summarized by the values of permittivity ε_r and permeability μ_r . Here the index r indicates that these values are of relative meaning and denote the fraction $\varepsilon_r = \frac{\varepsilon}{\varepsilon_0}$ and $\mu_r = \frac{\mu}{\mu_0}$ respectively.

It should be mentioned that some authors use ε and μ without the index r to denote the relative permittivity and permeability. Within the theory

of magnetic fields the usage of the magnetic susceptibility $\chi_m = \mu_r - 1$ is more common as the permeability.

As almost every biological tissue is hard to magnetize the relative permeability is usually close to one. Hence, the relative permeability can be omitted on further considerations.

In order to get a feeling on how the complex permittivity influences the propagating wave we have a closer look at the fundamental solution on \mathbb{R}^3 (equation (2.17)). It is obvious that the propagation of the wave is influenced by the in that case complex wave number k . If now the considerations are limited to a single frequency the wave number is, as commonly known, definable by:

$$k = 2\pi \cdot \frac{f}{c} \quad (2.19)$$

where c is the speed of light in the medium and f is the frequency. The speed of the light is in general defined by:

$$c = \frac{1}{\sqrt{\epsilon\mu}}, \quad (2.20)$$

and in the case of a medium with $\mu_r = 1$:

$$c = \frac{c_0}{\sqrt{\epsilon_r}}. \quad (2.21)$$

By using that, the wave number can be written by:

$$k = 2\pi \cdot \sqrt{\epsilon_r} \frac{f}{c_0}. \quad (2.22)$$

If the matter is electrical conducting $\sigma > 0$ then the relative permittivity is a complex value:

$$\underline{\epsilon_r} = \epsilon'_r - i\epsilon''_r = \epsilon_r - i \frac{\sigma}{\omega\epsilon_0} \quad (2.23)$$

with the real and imaginary part ϵ'_r and ϵ''_r respectively.

For a better understanding on how the imaginary part of the permittivity influences the wave, we now have a closer look on the fundamental solution (2.17). The solution is still valid, even in complex matter, only the wave

number is replaced by a complex wave number \underline{k} , which contains the complex permittivity.

It is easy to separate the periodical part of the expression

$$g(\mathbf{r}) = \frac{1}{4\pi \cdot |\mathbf{r}|} e^{i(\underline{k}|\mathbf{r}|)} \quad (2.24)$$

from the damping part. This can be achieved by setting $\underline{k} = k + i\kappa$

$$g(\mathbf{r}) = \frac{1}{4\pi \cdot |\mathbf{r}|} e^{i((k+i\kappa)|\mathbf{r}|)} = \frac{1}{4\pi \cdot |\mathbf{r}|} e^{i(k|\mathbf{r}|)} \cdot e^{-(\kappa|\mathbf{r}|)}. \quad (2.25)$$

All parts of the wave number are real values except of the complex permittivity. Unfortunately this value is under the square root. After some calculations the square root of the permittivity could be written as

$$\sqrt{\underline{\epsilon}_r} = \sqrt{\frac{|\epsilon_r| + \epsilon_r''}{2}} - i\sqrt{\frac{|\epsilon_r| - \epsilon_r''}{2}}. \quad (2.26)$$

A derivation of the complex root can be found at appendix A. If we look at the result it is obvious that a positive σ does not only generate a damping effect but also influences the speed of the wave and therefore leads to a phase shift compared to a non-conducting medium. This is an important point and has to be considered when trying to detect strokes.

2.3.1 Reflection and Diffraction

As most objects under examination are compositions of not only one kind of material other influencing effects have to be considered, too. The effects mentioned here are called reflection and diffraction. Reflection is an effect preventing a part of or the whole electromagnetic wave to pass the interface between two materials. Instead, it reflects this part or the whole wave to the area where it came from. The diffraction leads to directional changes of the wave, depending on the angle of incidence and the difference in permittivity between two adjacent materials.

The influences of the described effects on the amplitude are formulated in Fresnel's equations. The amplitude of the reflected wave is given by

$$E_R = \left(\frac{\alpha - \beta}{\alpha + \beta} \right) \cdot E_I \quad (2.27)$$

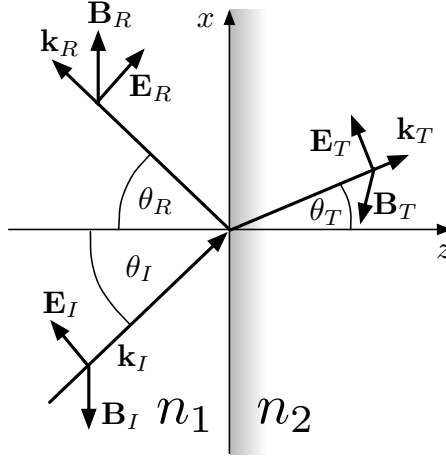


Figure 2.2: Schematic view of the relation between the incident wave (\mathbf{E}_I , \mathbf{B}_I and \mathbf{k}_I), the reflected wave (\mathbf{E}_R , \mathbf{B}_R and \mathbf{k}_R) and the transmitted wave (\mathbf{E}_T , \mathbf{B}_T and \mathbf{k}_T). (based on [7, Fig. 9.15])

and the amplitude of the transmitted wave by

$$E_T = \left(\frac{2}{\alpha + \beta} \right) \cdot E_I. \quad (2.28)$$

β is defined by

$$\beta \equiv \frac{\mu_1 n_2}{\mu_2 n_1} = \frac{n_2}{n_1} = \frac{\operatorname{Re}\{\sqrt{\epsilon_{r,2}}\}}{\operatorname{Re}\{\sqrt{\epsilon_{r,1}}\}} \quad \text{with} \quad \mu_1 = \mu_2 = 1 \quad (2.29)$$

and α by

$$\alpha \equiv \frac{\cos \theta_T}{\cos \theta_I} \quad (2.30)$$

where θ_I is the incident angle and θ_T the angle of the transmitted wave. Figure 2.2 gives a visible impression of the relationship between the wave directions and angles.

It must be kept in mind that the transmitted wave is always in phase with the incident wave. This is in contrast to the reflected wave, which is only in phase with the incident wave if $\alpha > \beta$, otherwise it experiences a phase shift of 180° [7, p. 491-498].

2.4 Scattering Problem of Electromagnetic Waves

If an electromagnetic wave is penetrating a region of non-homogeneous permittivity the wave experiences diffraction and refraction as well as the wave is split into transmitted and reflected partial waves. This process is in general called scattering. In electromagnetics a scattering problem can be written as

$$\nabla^2 \mathbf{E}(\mathbf{r}) + k^2 n(\mathbf{r}) \mathbf{E}(\mathbf{r}) = 0 \quad \text{in } \mathbb{R}^3, \quad (2.31)$$

$$\mathbf{E}(\mathbf{r}) = \mathbf{E}_{\text{inc}}(\mathbf{r}) + \mathbf{E}_{\text{scatt}}(\mathbf{r}) \quad (2.32)$$

where \mathbf{E}_{inc} denotes the incident field and $\mathbf{E}_{\text{scatt}}$ the scattered field. The field must satisfy the Sommerfeld radiation condition:

$$\lim_{|\mathbf{r}| \rightarrow \infty} |\mathbf{r}|^{\frac{n-1}{2}} \left(\frac{\partial}{\partial |\mathbf{r}|} - ik \right) \mathbf{E}(\mathbf{r}) = 0 \quad (2.33)$$

with n , the dimension of the space (here 2 or 3).

2.4.1 Lippmann-Schwinger-Equation

A wide range of direct scattering problems can be rewritten using the method of integral equations, whereby the resulting integral is called Lippmann-Schwinger-Equation. This integral equation describes the scattering problem (2.31 - 2.33) and is given by

$$\mathbf{E}(\mathbf{r}) = \mathbf{E}_{\text{inc}}(\mathbf{r}) - \underline{k}^2 \int_{\mathbb{R}^3} g(\mathbf{r} - \mathbf{v}) m(\mathbf{v}) \mathbf{E}(\mathbf{v}) \, d\mathbf{v} \quad \mathbf{r} \in \mathbb{R}^3 \quad (2.34)$$

with $m := 1 - n(\mathbf{r})$ and $n(\mathbf{r}) := \frac{c_0^2}{c^2(\mathbf{r})}$ [12].

The Human Head under Microwave Exposure for Microwave Imaging

The human head and its complex structures in conjunction with the different permittivities of the tissues it consists of is responsible for signals with extremely complex morphologies if examined by microwaves. Due to the high level of individual differences concerning brains, not only between different persons, but also between different locations within the head, the extraction of the responses from for example a stroke diseased tissue, is very difficult. In addition to that, the two halves of the neopallium are not perfectly symmetrical, and that restricts the other side of the head to be used as a reference signal.

This chapter gives an overview of the structures of the human head and their influences on signals used for microwave imaging. Furthermore it is an introduction to the general setup of microwave imaging systems.

3.1 Microwave Imaging

All microwave imaging systems have a similar setup if the technical design is compared. The elements that are always present are a variable number

of antennas, a signal-generating and measuring unit as well as a computing system to evaluate the signals. For scientific purposes usually a network analyzer is used to generate and measure the signals. The network analyzer usually measures the static case of a monochromatic wave so that successive samples of discrete frequencies would be measured if it is used to measure ultra-wide band signals. Often these values are delivered as so-called scattering parameters (S-parameters)

$$S_{j,i} = \left. \frac{b_j}{a_i} \right|_{a_j=0} \quad (3.1)$$

where b_j denotes the arriving wave at port j and a_i is the wave injected over port i . The square of b and a have the quantity of power.

The set of antennas is usually distributed around the object in such a way to maximize the coverage. In other words, there have to be enough differing views of, at the best case, every angle at the object.

The object is then illuminated by a microwave signal, called a stimulation signal. The signal is sent by a subset of the antennas (often this subset is a single antenna). Two different types of measurement strategies are distinguished; the mono-static measurement and the multi-static measurement. If the mono-static measurement is chosen, the same set of antennas which send the simulating signal are also used to receive the signal. In contrast the measurement of multi-static signals is performed by the remaining non-sending antennas. Figure 3.1 gives a schematic view of a microwave measurement setup.

3.2 Human Head Anatomy and Effects on Microwaves

The human head is a difficult-to-image object if wave-based techniques like ultrasonic or radio frequency microwave imaging should be used.

This section points on the effects the occurring tissue layers have on the signals measured with microwave imaging techniques as well as on a few anatomical details that are important when the results of those algorithms are interpreted.

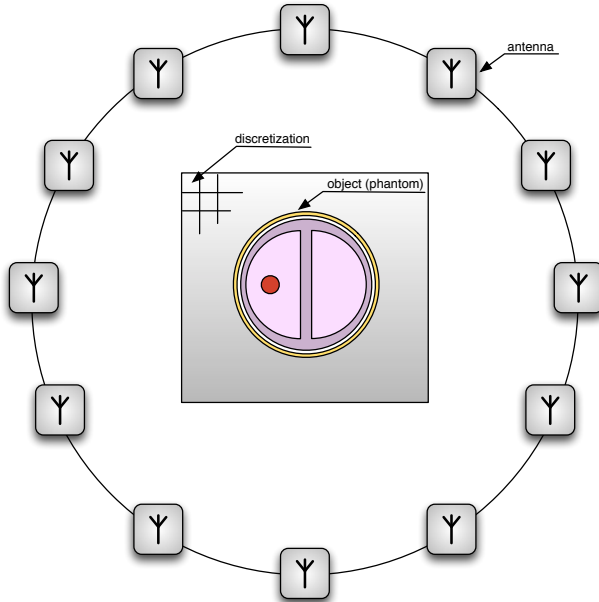


Figure 3.1: Schematic design of a microwave imaging system. The object under examination is a phantom similar to the phantom later described (chapter 6). Often the object domain is discretised. The distance between the domain D and S can even be narrow.

3.2.1 The Scalp

The skin and the tissues underneath, surrounding the head, are called the scalp. The scalp is the first layer the microwaves have to pass through. The exact composition of the scalp is not relevant due to the frequency range used. Hence, we limited our view to the effect a layer with an average permittivity would have (the layer was assumed to have the permittivity of skin). In addition to its conductivity, it delivers a high contrast in conjunction with air. The skin over the cranium is varying in its thickness from three up to seven millimeters. This is especially interesting for the later introduced delay and sum algorithm and the robustness test made on it.

3.2.2 The Skull

The cranium or skull is a composition of bones, shielding one of the most important and highly sensitive organs, the brain. Its original task is to protect the soft tissues of the brain from mechanical violence, but unfortunately (for our purposes) it is also a good protection against electromagnetic and even ultrasonic waves. The protecting effect is a result of the high conductivity and the high relative permittivity of the cerebrospinal fluid (CSF) in conjunction with the comparably low permittivity and low conductivity of the cranial bones. This high contrast leads to a reflecting barrier for microwaves, hence only a comparably small amount of energy can penetrate and even less can leave the brain. The cranial bone has an average thickness of about $6.0\text{ mm} \pm 1.5\text{ mm}$ [13].

3.2.3 The Morphology of the Brain

The brain is a highly complex organ in functionality and morphology. The morphology is unique for every person (an important fact for later discussions). In the following subsections the main structures of the brain and their location are described.

For the simplified phantom, developed during this work, the differences in permittivity were most important. Schematically, the materials can be separated in two main tissue types:

- The grey matter: The outermost layer of the neocortex and part of the midbrain are consisting of it. Grey matter is containing mostly the somata (the body of the pyramidal cell neurons with long axons connected to other parts of the brain).
- The white matter is a substance mostly consisting of the axons of neurons and glial cells.

3.2.3.1 The Cerebrum

The cerebrum is thought to be the part of the brain, where our memories are saved and it is also the part where most of the so-called higher functionality is originated. The neocortex (the outermost layer of the cerebrum) of humans is one of the biggest of all animals, only dolphins have a bigger

one. Its surface is up to 1100cm^2 [14, 215]. The folds, called gyri, and grooves, named sulci, are a direct result of these huge dimensions. The sulci and gyri arise during the rapid expansion of the neocortex at the embryonic development. It is organized in two hemispheres, each of it folded in a slightly different manner. The asymmetry of the halves could be an effect of the lateralization of brain functions and thereby seems to have a genetic origin. This is still subject of research [15].

3.2.3.2 The Cerebellum

The cerebellum is important to coordinated complex moves, where multiple muscles are involved. Despite its small dimension, if compared to the cerebrum, the cerebellum contains about 50% of all neurons of the whole brain. This is possible due to the high density of neurons at the thin grey matter layer on the surface of the cerebellum.

The morphology of the surface is comparable to the neocortex and of complex nature. It is divided in two hemispheres. The separating fold is not as pronounced as it is at the cerebrum. The horizontal folds all over the surface are, similar to the gyri of the cerebrum, necessary to room the enormous surface.

3.3 Stroke Disease

Clinically a stroke is defined to be a “sudden, non-convulsive focal neurological deficit” [16].

About 80% of the occurring strokes are of ischemic type meaning that blood supply is interrupted. The remaining 20% of strokes are caused by ruptures of vessels within the brain. These patients are suffering a hemorrhagic stroke [1].

One problem concerning imaging stroke by microwaves is the absence of information about the changes in permittivity caused by the stroke. It is hard to get data of newly affected tissues (within the first hour), especially if it must be recorded by a not-sufficiently-tested device.

The only paper describing the change in permittivity in the transition from live to death published 2003 by Schmid et al. and Burdette et al. 1986. Schmid et al. observed a change of the real part of permittivity of

about 3 – 4% and of conductivity by 11 – 15% at a frequency range of 800 – 1900 MHz. Whereby the team of Burdette measured a different drift. Burdette et al. were observing a deviation of about 9% of real part of permittivity and 18% of conductivity. Three differences in measurement techniques could explain the inconsistency. First, and also mentioned by Schmid et al., Burdette et al. measured the tissues after removing the arachnoid skin layer, second the measurements of Burdette et al. were taken of a different frequency (2450 MHz) and at last the measurements of Burdette et al. were made on canine brain whereas the measurement of Schmid et al. were made on porcine brain tissues [17, 18].

Another paper published by Schmid et al. about measurements on human patients 30 minutes before and up to 10h (at different subjects) after death was also not able to offer specific differences in permittivity occurring when the tissues were dying [19].

It seems to be complex and not a question to be answered easily. As a result of all these studies we can only assume that the differences between living tissues and dead tissues are significant but small. For this project this meant: a device is needed which is able to recognize these small differences of a few percent. Or if only bleeding should be excluded, even comparably small amounts of blood must be found within the brain.

3.3.1 The Hemorrhagic Stroke

Although the hemorrhagic stroke is the less common one it is the one preventing the doctors from a fast treatment.

Most of the treatments that are technically fast performable, as for example the lysis therapy¹, would have devastating consequences on patients suffering from a hemorrhagic stroke.

The main risk factor for the occurrence of a hemorrhagic stroke is thought to be hypertension. Assumably 15% of all occurring strokes are caused by the so-called sudden intracerebral hemorrhage. The high pressure within the arteries leads to ruptures at typical locations, mostly in the subcortical white matter or at the pons.

¹Medication with a fibrinolytic agent. Main complications are sudden internal bleeding.

Pre-existing illnesses are thought to be responsible for the remaining 5% of the hemorrhagic strokes [1].

3.3.2 Ischemic Strokes

Embolism of vessels supplying the brain with blood in general are the reason for a patient to suffer an ischemic stroke. About 50% of the ischemic strokes are caused by macroangiopathy and another 25% by microangiopathy. Similar to hemorrhagic strokes hypertension is also the main risk factor for ischemic strokes. Especially, the systolic pressure is the value with the highest sensitivity [1].

A treatment with trombolitic drugs is thought to be effective within the first 4.5 *h*. After that time nothing can be done to improve the outcome.

The reason for the closing window lies in tissues with affected supply which surrounds the stroke core. They start to die over time while the stroke core is growing.

Optimization

A wide range of applications in modern science are related to problems with only partially measurable parameters. The models however demand for the remaining non-measurable parameters. They have to be estimated, in case there is a linear relation between the measured data and the hidden parameters e.g. linear regression analysis is a preferred method. In case of non-linear relation an optimization method is needed.

Another reason why research projects are linked to parameter estimations is that parameters which are indeed measurable have to be known but they can not be measured without causing breaking the object of interest (in our case the patient suffering a stroke). Thus, they have to be estimated from indirect measurements.

A good point to begin with the understanding of mathematical optimization theory is a basic optimization algorithm. A Fundamental and easy to understand method is generally known as Newton's or Newton-Raphson method.

Over the years many modifications were introduced, especially to avoid the second derivative of the problem. One of these methods (also used in the work) is the Gauss-Newton method.

The following sections explains Newton's method, the modifications the Gauss-Newton method provides, the computation of the step length within these methods and the efficient method of conjugated gradients. All of these algorithms are treated in detail in [20].

4.1 Newton-Raphson Method

As generally known Newton's Method is a numerical algorithm to approximate the solution of $f(x) = 0$. Thereby the solution is found by iteratively calculating the root of a Taylor expansion of the current point x_n .

$$T(x) = 0 = f(x_n) + f'(x_n)(x - x_n) \Rightarrow x_{n+1} = x_n - \frac{f(x_n)}{f'(x_n)} \quad (4.1)$$

Thus, to start the algorithm a start point x_0 must be chosen. The start point should be close to the root to guarantee the convergence of the algorithm, or mathematically spoken, within a convex region around the minimum. If for example an other extremum is between the root and the starting point the algorithm will converge to a wrong solution or even worse find no solution at all.

This is also true for multivariate systems $f(\mathbf{x}_n)$, where the update formula could be written by

$$\mathbf{x}_{n+1} = \mathbf{x}_n - \mathbf{J}^{-1}(\mathbf{x}_n) \cdot f(\mathbf{x}_n), \quad (4.2)$$

with \mathbf{x}_n the current vector of unknowns and \mathbf{x}_{n+1} the new arguments vector and \mathbf{J} a matrix containing the partial derivatives, namely Jacobi matrix (some time just called Jacobian). If $f: \mathbb{C}^n \rightarrow \mathbb{C}^m$ is complex-valued then \mathbf{J} will be a $m \times n$ matrix and therefore not invertible. To overcome this a pseudoinverse \mathbf{J}^+ is utilized.

A commonly used pseudoinverse is the Moore-Penrose pseudoinverse [21]. For a matrix \mathbf{A} with linear independent rows, and its Hermitian transposed \mathbf{A}^H , the pseudoinverse is

$$\mathbf{A}^+ = \mathbf{A}^H (\mathbf{A} \mathbf{A}^H)^{-1} \quad (4.3)$$

and for matrices with linear independent columns it is calculated by:

$$\mathbf{A}^+ = (\mathbf{A}^H \mathbf{A})^{-1} \mathbf{A}^H. \quad (4.4)$$

Now, if Newton's method is used for the task of parameter estimation it will operate on the derivative of the function and no longer on the function itself. The reason for this is obvious: For practical purposes it is usually

not possible to know an exact model of the problem, hence this is even linearized ($\mathbf{g}(\mathbf{x}) \leftarrow \mathbf{A}^+\mathbf{x}$) and if measurements are used the values usually contain noise. These errors have to be considered. So what we are usually looking for is a minimum of a so-called loss or objective function for example.

Hence, the update formula for a newton algorithm, operating on the derivative, is written by

$$\mathbf{x}_{n+1} = \mathbf{x}_n - \mathbf{H}^{-1}(\mathbf{x}_n) \cdot \mathbf{J}(\mathbf{x}_n), \quad (4.5)$$

with \mathbf{H} , the Hessian matrix. Where the Hessian is the second derivative

$$\mathbf{H}(\mathbf{x}_n) = \nabla^2 f(\mathbf{x}_n) \quad (4.6)$$

of a multivariate function.

Especially, if the optimization problem considers a high number of unknowns a calculation of the inverse Hessian will be a highly time expensive operation. To avoid this some brilliant minds introduced a number of modifications of the default Newton method. One of these modified methods is the Gauss-Newton method. As this method was also used during this work a small introduction is given at the next section.

4.1.1 Gauss-Newton Method

As mentioned before the Gauss-Newton method is a modified version of the default Newton method. Originally introduced for optimization problems it avoids the direct computation of the Hessian. A general objective function for a nonlinear least squares problem can be written as

$$f(\mathbf{x}_n) = \frac{1}{2} \|\mathbf{g}(\mathbf{x}_n) - \mathbf{y}\|_2^2 = \frac{1}{2} \|\mathbf{r}_n\|_2^2 \quad (4.7)$$

with \mathbf{r}_n the residual vector. The indices of the matrices and vectors are simplified notations and are standing for $\mathbf{A}_n := \mathbf{A}(\mathbf{x}_n)$.

Now with that we can define the Jacobi matrix to be

$$\mathbf{J}(\mathbf{x}_n) = \begin{bmatrix} \frac{\partial r_1(\mathbf{x}_n)}{\partial x_1} & \dots & \frac{\partial r_1(\mathbf{x}_n)}{\partial x_K} \\ \vdots & \ddots & \vdots \\ \frac{\partial r_M(\mathbf{x}_n)}{\partial x_1} & \dots & \frac{\partial r_M(\mathbf{x}_n)}{\partial x_K} \end{bmatrix} = \begin{bmatrix} (\nabla r_1(\mathbf{x}_n))^H \\ \vdots \\ (\nabla r_M(\mathbf{x}_n))^H \end{bmatrix}. \quad (4.8)$$

Based on this definition the gradient of the objective function can be written as

$$\nabla f(\mathbf{x}_n) = \sum_{j=1}^M r_j(\mathbf{x}_n) \nabla r_j(\mathbf{x}_n) = \mathbf{J}_n^H \cdot \mathbf{r}_n \quad (4.9)$$

and the expression for the Hessian as

$$\begin{aligned} \nabla^2 f(\mathbf{x}_n) &= \sum_{j=1}^M \nabla r_j(\mathbf{x}_n) (\nabla r_j(\mathbf{x}_n))^H + \sum_{j=1}^M r_j(\mathbf{x}_n) \nabla^2 r_j(\mathbf{x}_n) \\ &= \mathbf{J}_n^H \mathbf{J}_n + \sum_{j=1}^M r_j(\mathbf{x}_n) \nabla^2 r_j(\mathbf{x}_n) = \mathbf{H}_n. \end{aligned} \quad (4.10)$$

Within many applications the first term of (4.10) dominates the second. This is especially the case if we are close to the minimum, and this is exactly the approximation that was used. By neglecting the second term, the Hessian can be approximated by

$$\mathbf{H}_n = \mathbf{J}_n^H \cdot \mathbf{J}_n, \quad (4.11)$$

so that we do not need to compute any second derivatives. The benefit of this approximation is obviously reduced computational cost.

With that simplification the system to solve can be rewritten as

$$\mathbf{J}_n^H \mathbf{J}_n \mathbf{d}_n = -\mathbf{J}_n^H \mathbf{r}_n, \quad (4.12)$$

where \mathbf{d}_n is the search direction.

Depending on the optimization problem it can occur that the Hessian is singular or near to it, which can be the same due to limited numerical accuracy, so that a solution for \mathbf{d} can not be computed. Generally, problems with such conditions are called ill-posed. To overcome that a regularization is usually used. The most common one is the additive Tikhonov regularization. Hence, the system to solve can then be expressed by

$$(\mathbf{J}_n^H \mathbf{J}_n + \lambda \mathbf{E}) \mathbf{d}_n = -\mathbf{J}_n^H \mathbf{r}_n, \quad (4.13)$$

where \mathbf{E} is the identity matrix and λ a scalar parameter that has to be optimized as well. This approach will add the Tikhonov-Regularization

parameter λ to each entry on the main diagonal of the approximated Hessian matrix.

If the Jacobi matrix has full rank and the gradient is not zero the direction d will be a descent direction. But the knowledge of the direction alone is often not enough to guarantee fast convergence of the algorithm. If we deal with nonlinear problems the derivative of the objective function will often vary from point to point. This and the numerically approximated derivative in combination with the regularization influences the obtained direction. Thus even if we know that we have a descending direction we do not know how far we have to go. Here, choosing one as step width would rarely be a good choice, consequently the update of the step has to be written as

$$\mathbf{x}_{n+1} = \mathbf{x}_n - \alpha \cdot \mathbf{d}_n. \quad (4.14)$$

Now, to evaluate a sufficient step length a line search algorithm is often used.

4.2 Line Search Procedure

A line search is a way to estimate a good step length and a good algorithm is often a way to save a lot of computation time, since each function evaluation means performing a complete forward calculation. This is especially true for multivariate and nonlinear systems, where the derivative is only numerically calculable.

Over time many different line-search strategies were developed. Here, an algorithm based on a secant decrease will be introduced, and later used in section 7.2.

The search takes place on the single valued objective function

$$g(\alpha) = f(\mathbf{x}_n - \alpha \cdot \mathbf{d}_n). \quad (4.15)$$

Starting with an initial guess $\alpha_0 = 1$ in combination with the current value $\alpha = 0$ and the average value $\alpha_{m,0} = \frac{\alpha_1 + 0}{2}$, the first derivative g' at $\alpha = 0$ and $\alpha = \alpha_0$ as well as the second derivative g'' at the average value $\alpha_{m,0}$ is approximated. These values are used to compute a Newton like

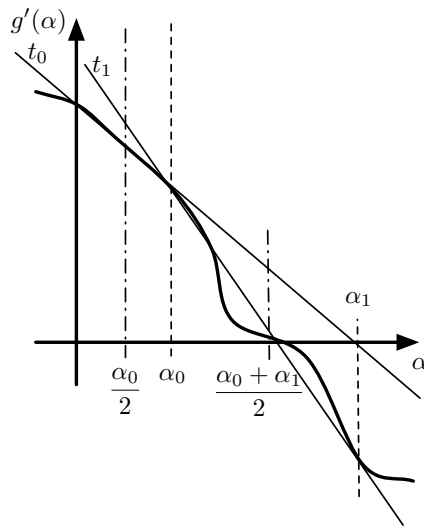


Figure 4.1: Schematic of a line search strategy which is based on a Newton like parameter estimation and the numerical approximation of the first and the second derivative. The interval to approximate the derivatives depends on the last and the current value to save computation time.

update step

$$\alpha_{n+1} = \alpha_n \pm \frac{g'(0)}{g''(\alpha_{m,0})}. \quad (4.16)$$

From there the described steps are repeated at the new interval $[\alpha_0, \alpha_1]$. Figure 4.1 gives a graphical view of the procedure.

Naturally, there are some traps that must be avoided. The plus-minus symbol is already a hint. The symbol indicates that we can't always be sure that the achieved direction is a decreasing one. Another problem is a resulting low convergence rate of the sub-problem (finding an optimal step length for a given search direction). To avoid endless computations it is wise to define a maximum number of iterations in the implementation of the line search as well as a minimum accuracy threshold used as an abort criterion.

4.3 Conjugate Gradient Methods

The conjugate gradient (CG) is a method introduced 1950 by Hestenes and Stiefel to efficiently solve large linear systems with symmetric and positive definite coefficient matrices [20, p. 101]. If these conditions are met, the solution for an $N \times N$ System is computed at mostly N iterations, under the assumption of exact arithmetic.

The CG algorithm is an iterative algorithm solving the problem

$$\mathbf{Ax} = \mathbf{b}. \quad (4.17)$$

The updated solution \mathbf{x}_{n+1} is given by

$$\mathbf{x}_{n+1} = \mathbf{x}_n + \alpha_n \cdot \mathbf{p}_n \quad (4.18)$$

whereby \mathbf{x}_n is the old solution, α_n a step length and \mathbf{p}_n a descent direction out of a set of nonzero vectors $\{p_0, p_1, \dots, p_M\}$ having a property called *conjugacy*:

$$\mathbf{p}_i^T \mathbf{A} \mathbf{p}_j = 0 \quad \text{for all } i \neq j. \quad (4.19)$$

The α_n is the minimizer of the quadratic minimization problem that is equivalent to (4.17)

$$\arg \min_{\alpha_n} f(\mathbf{v}_n) = \frac{1}{2} \mathbf{v}_n^T \mathbf{A} \mathbf{v}_n - \mathbf{b}^T \mathbf{v}_n \quad \text{with } \mathbf{v}_n = \mathbf{x}_n + \alpha_n \mathbf{p}_n, \quad (4.20)$$

and can be explicitly calculated by

$$\alpha_n = -\frac{\mathbf{r}_n^T \mathbf{p}_n}{\mathbf{p}_n^T \mathbf{A} \mathbf{p}_n} \quad \text{with } \mathbf{r}_n = \mathbf{A} \mathbf{x}_n - \mathbf{b}. \quad (4.21)$$

The conjugate vectors are usually generated during the procedure. To start the algorithm an initial guess \mathbf{x}_0 must be given, where the first vector \mathbf{p}_0 is set to

$$\mathbf{p}_0 = -\mathbf{r}_0, \quad (4.22)$$

with the residual vector $\mathbf{r}_0 = \mathbf{A} \mathbf{x}_0 - \mathbf{b}$. The next conjugated vector \mathbf{p}_n is then calculated during the iterations by

$$\mathbf{p}_n = -\mathbf{r}_n + \beta_n \mathbf{p}_{n-1}. \quad (4.23)$$

The scalar β_n can be calculated with equation (4.23), if it is premultiplied by $\mathbf{p}_n^T \mathbf{A}$. By regarding condition (4.19) we obtain

$$\beta_n = \frac{\mathbf{r}_n^T \mathbf{A} \mathbf{p}_{n-1}}{\mathbf{p}_{n-1}^T \mathbf{A} \mathbf{p}_{n-1}}. \quad (4.24)$$

The CG method is valid for complex values to, but there the transposed parameters have to be replaced by the Hermitian transposed parameters.

Modified versions of the CG method can be used for systems with non-symmetric coefficient matrices as well as systems based on non-linear equations [20, 102-109]. The later introduced Contrast Source Inversion (CSI) method is for example a derivation of the CG method, too.

METHODS AND RESULTS

Basic Signal Analysis

Especially for ultra-wide band signals using beamforming algorithms it is interesting to know more about the signals. But also for the tomographic algorithms, mostly operating on monochromatic signals, a closer look can help to understand limits.

5.0.1 Composition of the Ultra-Wide Band Signals

As indicated before, signals for microwave imaging purposes usually are complex. If the principle of superposition is kept in mind, it is obvious that the achieved complex signals are compositions of reflections and refractions of the original stimulating signal. Due to the dispersive character of biological materials, the original signals are also transformed by simply propagating through the medium.

To illustrate this behavior and the development of such signals, an artificial signal was generated. Therefore the formulations of section 2.3.1 and the fundamental solution for the three-dimensional point source (2.17) was utilized. By choosing the three-dimensional solution, the signal experiences a stronger attenuation if compared to e.g. one- or two-dimensional solutions. Hence, a step to a little more realistic scenario was reached. The incident wave is therefor generated in a quite similar way, such as a network analyzer will usually do by simply using a discretized rectangle in

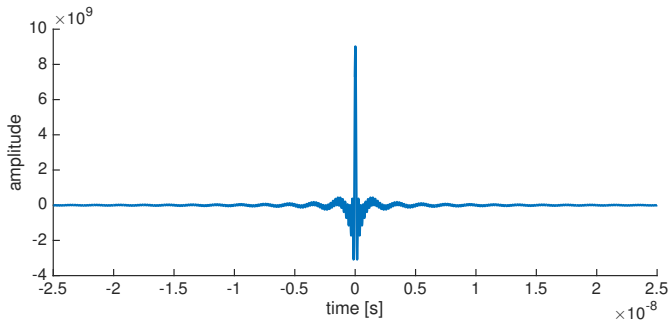


Figure 5.1: The incident wave, achieved by a rectangular signal at frequency domain with a frequency range of 0.5 to 5 GHz.

Table 5.1: Thickness of all materials in z direction, whereas they were infinite in $\pm x$ and $\pm y$ directions. The table contains the thickness in z dimension. The source was thought to be in direct contact to the first material.

| Material: | thickness: |
|---------------------|------------|
| skin | 5 mm |
| skull | 5 mm |
| cerebrospinal fluid | 1 mm |
| gray matter | 2 cm |
| white matter | 9 mm |
| blood | ∞ |

frequency domain. Hence, the time domain signal is a sinc function. The incident wave achieved in that way is shown in Figure 5.1.

To simplify the calculations a model with infinite plane boundaries between the different materials was assumed. The model includes five different material layers. The materials and their thickness are given in Table 5.1. The stroke was represented by a layer of the same dimension inside the white matter which had the permittivity of blood. The necessary permittivities therefor were taken from the tissue database of the Foundation for Research on Information Technologies in Society (IT²IS) [22].

The generated signal was an ultra-wide band signal with 100 discrete samples from frequencies of 500 MHz up to 5 GHz.

The whole calculation was performed in the frequency domain. Afterwards the signals were transformed back to time domain. As indicated

before, no morphology was imprinted on the stimulus signal, hence, the amplitude of all samples in frequency domain was 1 at the beginning. By summing up all first reflections, after they had been back-propagated to their origin, a signal as observable in Figure 5.2 could be reached. It

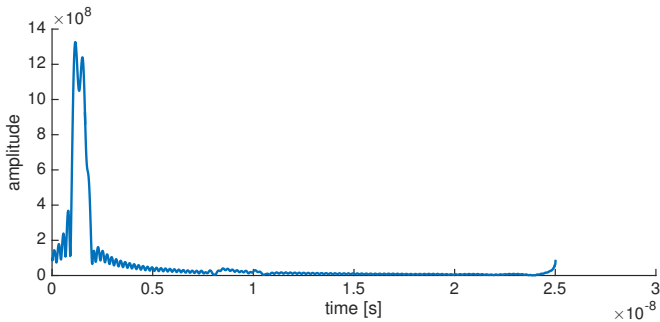


Figure 5.2: The sum of all first reflections occurring on a simple planar model with infinite extent. To simulate the propagation the three dimensional fundamental solution was used (equation (2.17)). The part of the signal I was interested in was not easily observable.

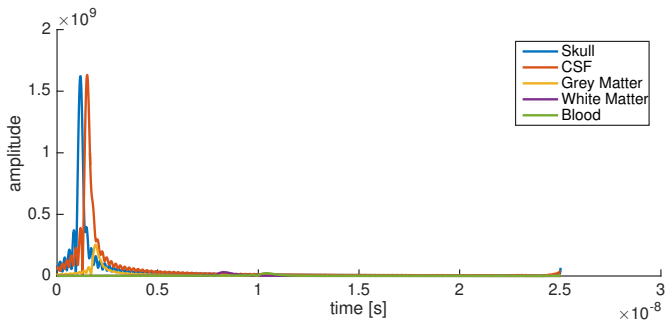


Figure 5.3: Separate parts of the signal observable at Figure 5.2. The curves represent the reflections after they were back-propagated to the source.

could be recognized that the signal part originally reflected at the blood boundary is hardly observable. It is better observable in the plot at Figure

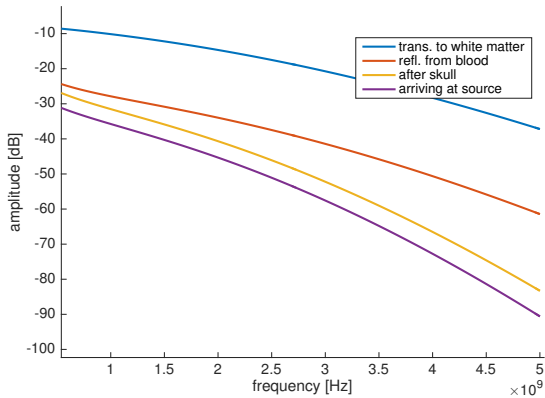


Figure 5.4: The signals experience a strong attenuation when propagating through the materials. This figure shows the attenuation of the signals when they arrive at the specified materials, where the blue colored line shows the signal as it arrives in white matter and the remaining lines demonstrates the signal on the way back to the source.

5.3, which shows the signals before they were summed up. Figure 5.4 depicts the weakening the signal experienced during the propagation through the model and backwards to the source. I was observing a decrease of the amplitude of up to -90 dB ¹. The curves are showing the signals in frequency domain as they arrived at the specified materials.

It should be kept in mind that signals on real three-dimensional setups experience an even stronger attenuation as the materials surfaces are usually smaller and curved in some way. This means a good portion of energy is missing the receiver.

In addition to that it must be mentioned that only first reflections were considered. This, in combination with the naturally complex morphology of the brain, will lead to many more responses and therefore to a significantly more complex output signal.

¹As we are talking about fields, the decibel definition with quadratic amplitudes was used: $G_{dB} = 10 \cdot \log \frac{|A_0|^2}{|A_1|^2}$

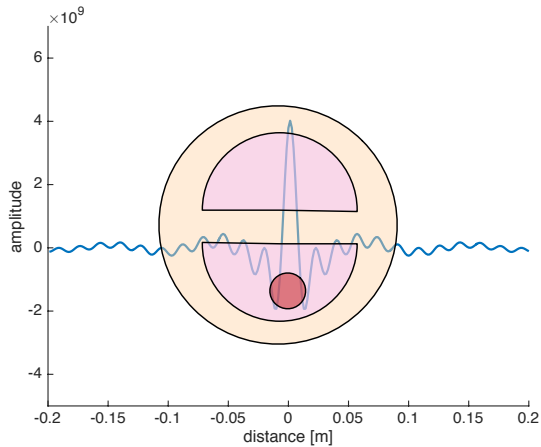


Figure 5.5: The wide band signal, as it was later used on the delay and sum algorithm (500 MHz to 2.5 GHz with one difference, there the signal was windowed with a Tukey window). On the x -axis the extent of the signal, calculated at a permittivity of $47.0 - i18.7$ is shown. In front of the signal a true-to-scale phantom is drawn.

5.0.2 Spatial Extent of the Signals

As the spatial resolution of algorithms presented here depend, among other things, on the frequencies involved, the spatial expansion of the signals is also of interest. To illustrate that two small figures were generated.

The first of them (Figure 5.5) shows a true-to-scale head model in front of the ultra wide-band stimulus signal. As later explained, it was not useful to include signal parts above 2.5 GHz, hence, the signal illustrated here, has a frequency range of 0.5 to 2.5 GHz. To calculate the distances, I used, similar as it was done for the delay and sum algorithm (section 7.1), an average complex permittivity of $47.0 - i18.7$ (of the phantom materials section 6.2.2.1) to calculate the speed of the electromagnetic wave within the medium (equation (2.21)). As mentioned above, the signal was of rectangular morphology in the frequency domain.

The second figure shows a monochromatic signal with its expansion over the same true-to-scale phantom (Figure 5.6). The frequency of the sinusoidal signal was 1 GHz. This frequency was selected as it shows the

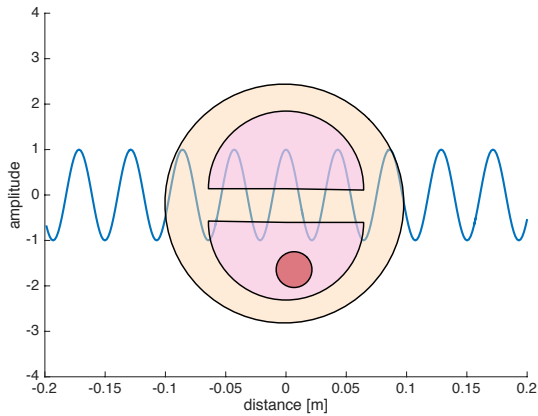


Figure 5.6: A monochromatic signal at 1GHz . The x -axis is presenting the spatial expansion of the sinusoidal signal. The extend was calculated on a permittivity of $47.0 - i18.7$. In front of the signal a true-to-scale phantom is drawn.

best results for the tomographic algorithms and in addition to that it was the frequency for which a Vivaldi-antenna, developed especially for that purpose, showed a good performance.

It is obvious that both signals are highly sub-sampling the details of the phantom and this is even worse with a realistic head.

Permittivity Phantom of the Human Head

Usually, it is not possible to achieve measurements of real subjects in an early state of research, especially if the technology, which should be tested, is without medical approval.

To circumvent the missing of data two ways are possible. The first way implies computer simulations. They are a good replacement for measurement data in the beginning. The benefits of it are a well-defined environment with usually well-known boundary conditions and therefore many errors can be avoided. Unfortunately, the computation of large problems is not possible in a reasonable period of time, especially if realistic details are integrated.

The second way to go is it to measure at a simplified setup usually with an artificial replacement for the patient. This replacement (called phantom) usually has only the major properties of a real patient. Important is that it is able to emulate the physical features and difficulties the algorithm needs to manage.

Hence, what our phantom must have is a comparable refraction between the layers. Therefore, the permittivity of the tissues of the head must be approximated.

The examinations and findings described in the following sections were obtained by two students while they were working on their bachelor thesis

under my guidance. Since, the findings were in many cases a product of a close cooperation and fruitful discussions, the pronoun “we” was used. During the bachelor thesis of Carl Christian Marzi [23] the examination of materials and a first draft of the phantom was developed. The verification of the phantom as well as further developments were the contribution of the bachelor thesis of Natalie Bauer [24].

6.1 Selection of the Materials

What was needed, was an easy to use and not-expensive material, so that phantoms with different shapes, with strokes of different types and with individual morphologies at different locations within the model can be created. Thus, ceramics with defined permittivity, so-called electronic ceramics were excluded. Over the last decades a number of material mixtures with different compositions have been proposed as a replacement for the soft tissues (skin, grey and white matter). Most of these mixtures are based on water.

It is commonly known that water has a very high permittivity of around 80 at 20°C, but the permittivity can be reduced by choosing a second material for the mixture having a significantly lower permittivity (could be called a filler). In most publications sucrose, glucose and/or starch (corn flour) were proposed as filler for head phantoms. An early example of a sugar-gelatin-based phantom was introduced by Marchal et al. 1989 [25]. The phantom was proposed for low frequencies applications. A more related publication was offered 2013 by Chew et al.[26]. The introduced phantom is thought to be used at microwave frequencies in the range of 1 to 6 GHz [26]. And as a last relevant publication it is important to mention the one by Mohammed et al. of 2012 [6]. The material they chose was a mixture of water, corn flour and oil. Figure 6.1 shows a compartment with the SAM (Specific Anthropomorphic Mannequin) head phantom [6].

If the two suggested materials for the soft tissues are compared we have to notice that the possible fitting of the mixtures made of sugar, water and gelatin by Chew et al. cannot be as accurate as it could be with the mixture containing corn flour and oil by Mohammed et al.. The slope

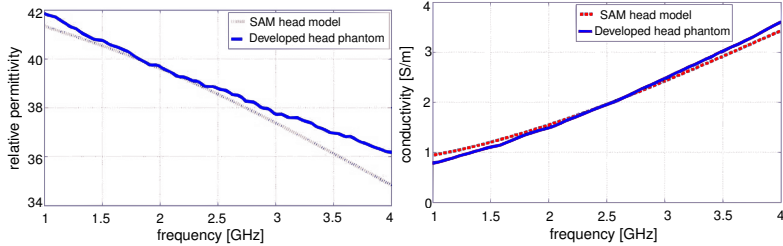


Figure 6.1: Relative permittivity (left) and conductivity (right) of the phantom material introduced by Mohammed et al. (a mixture primarily of oil, corn flour and water) in comparison to a SAM phantom.[6]

of the dispersion of the sugar-water-gelatin mixture is stronger than it should be (Figure 6.2), so an exact fit is not possible. Unfortunately, some

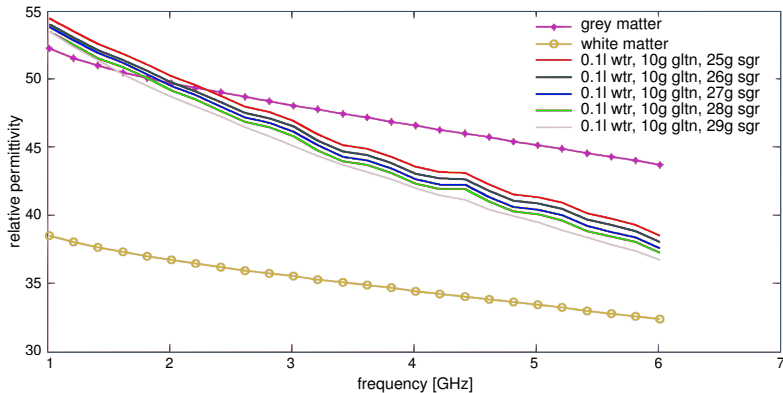


Figure 6.2: The sugar (sgr), water (wtr) and gelatin (gltn) based phantom material introduced by Chew et al.. The graphs were achieved during the investigations made when fitting the mixture to grey matter. [26]

preliminary tests showed that the mixture with oil and corn flour cannot be easily handled. In most of our samples the oil containing part of the mixture separated from the watery part as visible in Figure 6.3. The remaining samples of this mixture type showed measurable differences concerning the permittivity between the top of the sample and its bottom.



Figure 6.3: Investigations on mixtures containing oil, corn flour, gelatin and water. The part containing oil was separating before the mixture could solidify.

In the end our choice was the material without the corn flour and the oil. In detail we have chosen a mixture of common sugar, distilled water and porcine gelatin. The easy-to-manufacture mixture and the feature that it contains only simple commercial materials enables the phantom to be used for student experiments. Additional to the advantage mentioned above, the low number of components enables the phantom to easily fit the mixture ratios so that additional tissue types can be approximated.

The phantom with the selected material does not provide exactly the same reflecting properties as a real head. Hence, the approximation would only be suitable for algorithms working on monochromatic waves.

In general the stronger slope of the dispersion will influence the morphology of the signals in a stronger way as it would be with real tissues. The reason for the stronger influence on the morphology originates in the bigger differences between the respective propagation speeds (dispersion) of the frequencies involved. Due to the short propagation distance, if compared to the wavelength, this was not thought to be of significance for the later introduced UWB-Beamformer.

6.1.1 Material as Replacement for Bone

The cranial bone surrounding the head, as explained before (section 3.2.2), is an important feature of the human head. Especially for microwave imaging purposes it is a major source of reflections. Hence, a phantom that

does not regard this feature cannot be a good test object for the development of the measurement setup.

Our search for materials lead us to a couple of candidates, which could be able to represent the cranial bone. Two of those materials we thought to be possibly good replacements. The first one was epoxy resin in combination with rutile (TiO_2) and as a second we suggested Al_2O_3 to be a good choice.

The naturally high permittivity of rutile (between 150 and 200 [27]) makes it an ideal filler, able to raise the permittivity of materials which do have a low permittivity. We suggested epoxy resin as a good basis for the skull-mixture. The reason for choosing epoxy resin was, in addition to the solid form after it had been processed it also provides a high relative permittivity (4 – 6.5) [28]. Most of the other plastics usually only have permittivities between 2 and 3 [29].

6.1.1.1 Experiments with Rutile and Epoxy Resin

The first thing we needed to know was how strong the influence of the filler within the basis would be. We started with a concentration of about 25% *vol.* of the filler. At this concentration the TiO_2 powder could be easily mixed with the epoxy resin. Unfortunately, the concentration of the filler seems not to be enough to achieve a significant raise of the permittivity. Hence, we decided to increase the amount of the filler to a maximum. At about 75% *vol.* the mixture was not stable any longer and we were not able to achieve homogeneous mixtures. The ratios between 75% *vol.* and 25% *vol.* were either not sufficiently raising the permittivity or the mixture was not homogeneous.

A cut through the middle of a sample with 50% *vol.* showed a large number of small air bubbles (Figure 6.4). We suggested that due to that bubbles we were not able to measure the permittivity of the mixture correctly. Due to these problems we decided to reject this type of material mixtures.

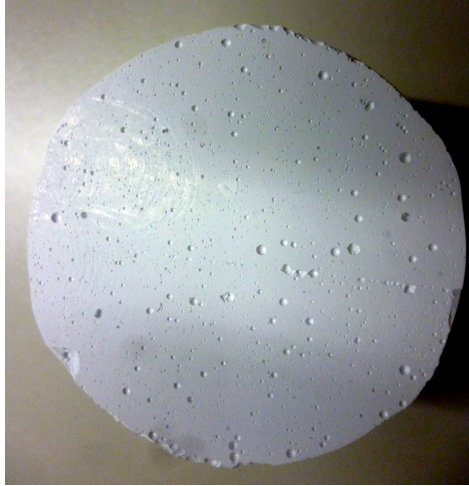


Figure 6.4: A cut through a mixture of epoxy resin and rutile with a ratio 50%. The image shows a large number of small air bubbles within the mixture. Hence, the material mixture was rejected.

6.1.1.2 Clay as Phantom Material for Bone

Al_2O_3 was mentioned above as a second material for the bone phantom. The natural occurrence of aluminum oxide does have different forms. The most common and natural form is a crystalline form called Corundum. Sapphire, ruby and emery are most commonly known as such types. Even if it is possible to manufacture synthetic crystals like corundum, it is still an expensive process and in addition to that the hardness of crystal makes a rework not affordable.

In its non-crystalline form, Al_2O_3 is the main component of pottery clay and therefore of ceramics. Even if ceramics with specific electrical properties can be manufactured and acquired by a handful of companies, we decided to take pottery clay itself to form the skull of our phantom. The so-called electrical ceramics are quite expensive. We decided that we could not make such purchases at this state of project.

In the beginning of our experiments we were concentrating on the relative permittivity and were ignoring the conductivity.

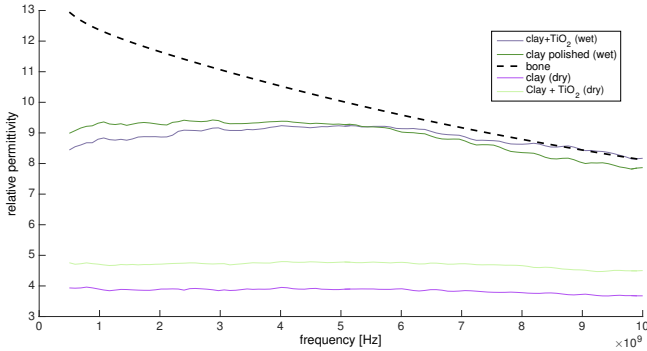


Figure 6.5: A comparison of the candidate materials for the skull phantom. The permittivity of wet fired clay is thought to be a sufficient approximation to the physiological bone.

Due to the porosity of fired clay and the unknown amount of other components of common pottery clay we could not expect the value for Al_2O_3 mentioned in literature. In addition to pure clay we were testing samples containing an amount of titanium oxide. Unfortunately, the rise in permittivity with titanium oxide was also not significant. This was especially the case with watered samples when the skull made of clay was a component of the whole phantom. Figure 6.5 shows the measured results. We have to mention that the result was strongly depended on the tight fit of the dielectric probe¹ on the sample. Due to the non-smooth nature of fired clay this could not be easily ensured. Polishing the sample helped to improve the situation but not to fix it completely. On poorly fitting locations the resulting measurements were usually lower as expected. An explanation would be that the comparably small amount of air between the probe and the sample would lead to the reduction of the average permittivity. Hence, we assumed that the highest measured permittivity would be the closest approximation to the real permittivity of the sample. Figure 6.5 contains the highest measured permittivity.

¹All measurements were taken by an Agilent E8363B Phase Network Analyzer in combination with the 85070E Dielectric Probe Kit.

Comparison The material we have chosen did not perfectly fit but for initial tests of the system and the algorithm it was sufficient. The complete phantom contained a hollow half sphere of pottery. Compared to the above mentioned published phantomes this was an even better approximation. For example, the phantom of Mohammed et al. contained a skull-phantom made of polyvinyl chloride (PVC). Even if this skull was in its morphology close to a realistic one, it was not if we look at the permittivity. The permittivity of PVC is somewhere between 2 – 5 and thereby far away to the permittivity of natural bone [30].

6.2 Development of the Phantom

First we had to decide how many details should be involved to achieve a good test in order to gain the first measurements. Every tissue layer of the head leads to a reflection and thereby to a reduction of the signal. Hence, our phantom should incorporate as many layers as possible. However, a too complex phantom complicates the interpretation of the results and thereby makes it hardly usable for algorithms under development. So we decided to omit the CSF and the most thin skin layers like the thin meninges. These thin meninges were thought to have a neglectable influence on the signal within the selected frequency range.

By regarding the above mentioned reasons we decided to include the scalp as the outermost layer, directly beneath it a layer for the bone, the skull, and inside the brain a layer for grey matter and another one for white matter.

All the layers were made of half-spherical shapes except of the innermost white matter layer. This one was used to approximate the hemispherical morphology of a realistic brain.

6.2.1 Finding the Correct Mixing Ratio

To obtain the correct permittivity the ratio in percent of the components of the mixture must be figured out. Therefore, a series of samples with different concentrations of sugar were manufactured. We started with a mixture without sugar and increased the sugar ratio up to the highest

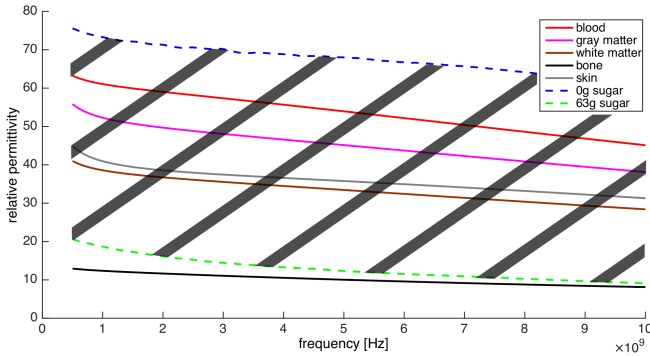


Figure 6.6: The reachable permittivity range when the sugar gelatin and water mixture is used. The reachable region is marked by the hatched area. The highest sugar concentration possible is at 63% and the lowest is with 0% sugar.

concentration possible, which was an amount of 63%² of sugar. With that concentration the mixture was losing its homogeneous property and pure sugar was visible on the surface of the sample. Furthermore, with this concentration it was very difficult to get rid of air bubbles brought in during the mixing process.

Hence, the reachable area of permittivities is set within a sugar concentration of 63% and 0%. Figure 6.6 illustrates this area.

6.2.2 Regression Graph for New Mixtures

To achieve the correct ratios for all materials a regression graph was fitted for the discrete samples achieved by the experiments described above. The fitting was done at a single frequency and thereby it is probably not a reliable solution for other frequencies. However, it is good enough to offer an initial idea for a new mixture representing a tissue having not been taken into account yet. The regression graph is given by the following formula:

$$\epsilon'(\omega) = \epsilon'_{min} + \frac{\epsilon'_{max} - \epsilon'_{min}}{1 + e^{-a(-\omega+b)}}. \quad (6.1)$$

²all percents are in weight percent.

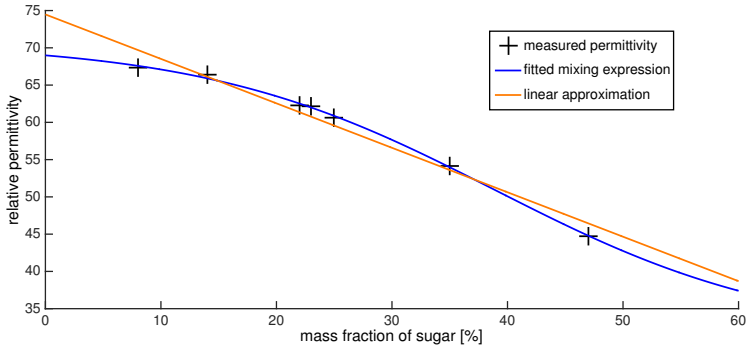


Figure 6.7: The graph contains a graphical representation of a linear fitting compared to the fitting of the mixing formula (6.1).

Table 6.1: The resulting parameters after having fitted the mixing formula (6.1) to the measurements.

| Formula | a | b | ε'_{max} | ε'_{min} |
|-------------------|---------|-------|----------------------|----------------------|
| logarithmic grows | 0.07947 | 38.89 | 70.71 | 31.18 |
| linear regression | -0.5965 | 74.48 | - | - |

Here the values ε'_{max} and ε'_{min} are an upper limit and a bottom limit respectively and the values a and b are free parameters without any physical meaning. The limits are naturally given by the permittivity of pure sugar and pure water. It has to be mentioned that only the real part of the complex permittivity was taken into account for the fitting. Due to the naturally given boundaries we selected a mathematical expression inspired by the formula for limited logarithmic growth. The parameter estimation itself was then made by a Trust-Region-Reflective algorithm provided by MATLAB. Figure 6.7 shows the resulting mixing graph in comparison to the measured samples and a linear approximation

$$\varepsilon'(\omega) = a\omega + b. \quad (6.2)$$

Table 6.1 contains the parameters we achieved with the fitting. To achieve the results visible in Figure 6.7 we decided to estimate all parameters (including ε'_{max} and ε'_{min}).

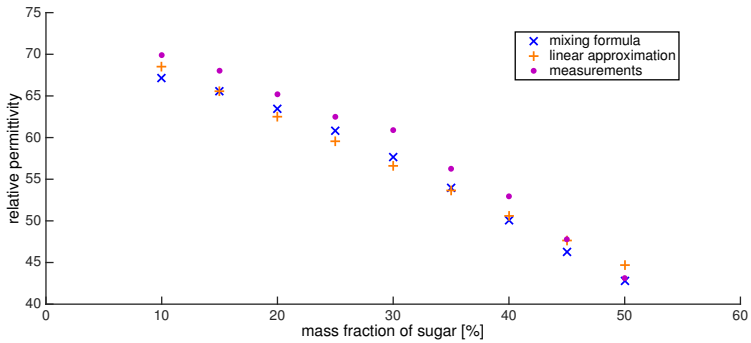


Figure 6.8: This graph is illustrating the measurements of a new series of samples and the proposed values of the mixing formula (6.1) and the linear approximation (6.2)

For the verification of the achieved results a second series of samples with different sugar concentrations were manufactured and measured. The precalculated potential permittivity was compared to the measurements. As visible in Figure 6.8 the manufactured samples did have the proposed permittivity, except from a systematical error. The deviation was about 2 in relative permittivity but still within systematic accuracy.

6.2.2.1 The Resulting Phantom Materials

After the investigations described above it was simple to obtain the correct ratio for the mixtures. The percentual ratio for every considered tissue can be read from Table 6.2. During our experiments a procedure to achieve reproducible homogeneous air-free results was developed. The procedure is mentioned below:

1. First the amount of water is measured and filled in a test glass on a heating device which also contains a magnetic stir unit.
2. The device was switched on and the sugar was intermixed. It was important that the device operates with a rotation high enough, otherwise the sugar could be burnt at the bottom of the test glass.
3. After having added the sugar but before the mixture was getting too hot the gelatin was intermixed.
4. Now the test glass was closed with a piece of cling film to prevent the water from evaporation.

Table 6.2: The percentual ratio for the phantom materials to achieve the permittivity visible at Figure 6.9

| phantom materials | water | sugar | gelatin | salt |
|-------------------|-------|-------|---------|-------|
| skin | 49 % | 45 % | 6 % | - |
| grey matter | 59 % | 35 % | 6 % | - |
| white matter | 47 % | 47 % | 6 % | - |
| blood | 80 % | 14 % | 6 % | 0.9 % |

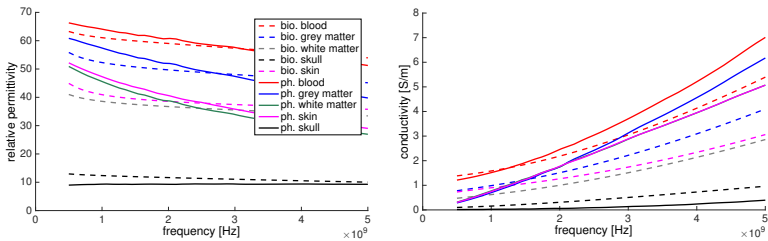


Figure 6.9: Comparing the phantom material to the real biological permittivities of the tissues we determined a difference especially concerning the slope of the real permittivity and concerning the conductivity.

5. After that the mixture was heated up to a temperature of around 70°C. But it must not boil.
6. When the temperature was reached it had to be held until all the gelatin particles were melted.

The resulting mixtures compared to their biological counterparts are plotted in Figure 6.9. The deviations from the right slope and the not well-fitted conductivity graphs are the main obvious defects. If neglecting the mixture for the hemorrhage the consistently too high conductivity increases the damping of the signals and thereby (if compared to a real head) an algorithm for imaging the inside has to manage it. However, the mixture simulating the hemorrhagic stroke had a too low conductivity compared to biological blood. Thus, a small amount of salt was necessary to reach the correct conductivity. We assumed that the generally higher conductivity would not be a problem.

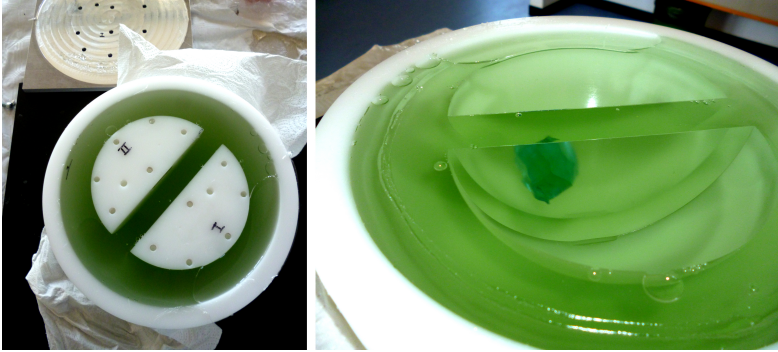


Figure 6.10: The left image shows the mold filled with grey matter mixture and the dummies for the white matter hemispheres. In the background there is the aluminum plate used to adjust the white matter hemispheres and to cover the mold. In the left image the blood clot placed within the white matter space is visible.

6.3 A Mold to Form the Phantom

As the materials were fluid during the process of manufacturing, a mold and a well-defined procedure was needed to form a solid phantom. We developed a mould with a diameter of 20 cm to achieve approximately the correct size of a head. The material chosen for the mold was polyoxymethylene (POM). The advantage of it was that the product can be taken out without any release agent. This was possible as POM is a plastic with an almost wax-like and hydrophobic surface. Due to the high level of water in our mixtures the product came off easily.

The layer in contact and therefore the outermost layer is the skin or scalp. The skin layer should have a thickness of between 3 to 7 mm . To ensure this thickness and to achieve a fit of the following layer, which is good enough, a centering device was necessary. The layer following on the skin was the skull and as this layer was made of fired clay we were able to use it directly to form the inner surface of the scalp layer. The natural properties of fired clay made it impossible to achieve an exact shape. That means the bone layer was not exactly spherically shaped but more in a non-smooth, elliptical shape so that we achieved a huge tolerance at the

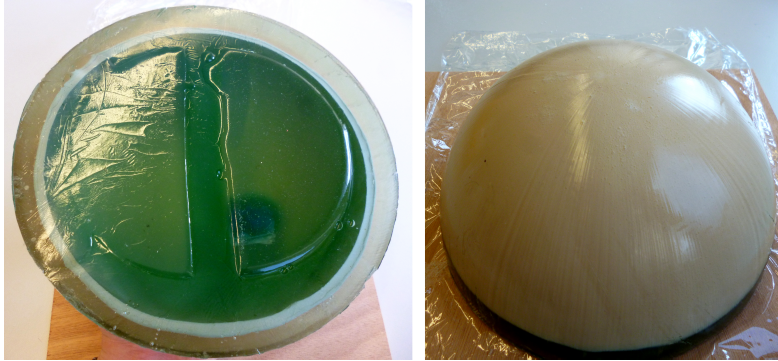


Figure 6.11: The complete phantom with a layer for skin, skull, grey matter, white matter and with a clod of blood. Left; the bottom view and right the top view of the phantom. The phantom was colored with a green coloring agent to make it easier to separate the layers.

thickness of the skin layer. To prevent the adjacent layers of the phantom from dehydration the clay as mentioned above was watered.

The next layer after the skull of our phantom was the grey matter. As a mold for that layer the skull made of clay was used. The room for the white matter was achieved by a dummy made of POM. The dummy was set on an aluminum plate. The plate was also used as a centering mechanism and to cover the POM mold after having filled in the grey matter mixture. Figure 6.10 shows a test cast with mixtures for grey and white matter as well as for blood. On the left side the dummy for the white matter within the grey matter is visible and on the right side the clot of blood within the white matter area can be seen. In the background of the left image the aluminum plate is also visible. What can be noticed is that the aluminum plate does have many holes. These holes were introduced as a reservoir for the mixture filled up before closing the mold. This was necessary as the mixtures were contracting when cooling down as otherwise it would leave the mold filled incompletely. It has to be noted that with the last step, when filling the white matter, it was quite important that the temperature was within a small range between 36°C and 40°C . This was necessary to achieve a sufficient adherence without melting the grey matter or the blood

clod, if present. A complete phantom containing all tissue layers and a hemorrhage is visible in Figure 6.11.

If a hemorrhage was integrated it had been placed either within the grey matter or within the white matter layer. To form the hemorrhage a sample of the blood mixture was manufactured and afterwards an approximate sphere was cut out.

6.4 Phantom Verification

After the development of the phantom we had to know about the durability and the reliability of the achieved compositions. This was important especially if errors were searched in a later step.

A reasonable assumption regarding watery mixtures always is that substances or even the water itself leaves its intended position and propagates into other mixtures. Therefore, an investigation was necessary. This was of interest as we had to know if and for how long we can use the approximated tissues.

6.4.1 Addition of a Separating Layer

As mentioned above we were assuming some kind of diffusion processes between our mixtures. If that was the case even smaller parts like the blood clod would vanish before anything could be measured. Hence, we started examinations of the permittivity from samples consisting of two mixtures each of the two with a different sugar concentration.

In total two different experiments were made to assess the influence and the amount of diffusion inside the phantom.

The first experiment The first experiment was made to verify whether there was a diffusion process at all. Therefore, two samples were manufactured. The first one was made by casting a white matter layer directly onto an existing grey matter layer. For the second sample (the reference sample) two layers were also made and stored separately. After having been stored four weeks at 7°C and wrapped in cling film the samples were compared by an optical examination and by measuring the permittivity on

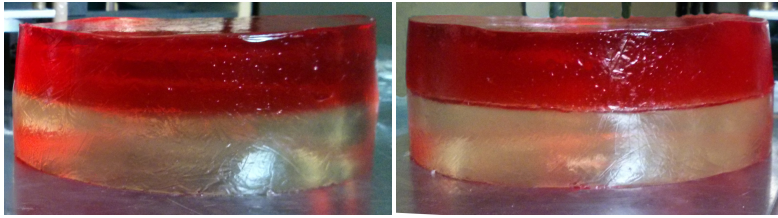


Figure 6.12: On the left the sample with the adhere layers and on the right the samples separately stored. The samples were stored for 4 weeks at a temperature of 7°C.

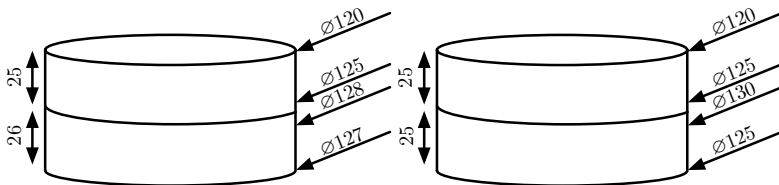


Figure 6.13: Schematic view of the samples. Left the sample with adhered layers and on the right the samples separately stored. The measured dimensions were thought to be a result of the diffusion process and the way they are stored (up Side of the layer is smaller).

both sides (top and bottom). With the optical comparison (Figure 6.12) a difference between the samples was clearly observable. The white matter part of the sample seemed to have increased. It looked as if it had absorbed a part of the water from the grey matter layer above. A deformation was also observed at the reference sample. The reason for it was thought to be a result of the evaporation of water and of the place the sample was stored in within the refrigerator. Some parts of the deformation, visible at the test sample, surely have been caused by the same reasons as they have been at the reference sample. Therefore, a pure optical analysis was not sufficient. A schematic representation of the deformation is given in Figure 6.13. Figure 6.14 represents the measured permittivities. A considerable difference between the sample with separately stored layers and the sample with adhesive layers is observable. Especially, the grey matter layer shows alterations even on the surface opposite to the white matter layer.

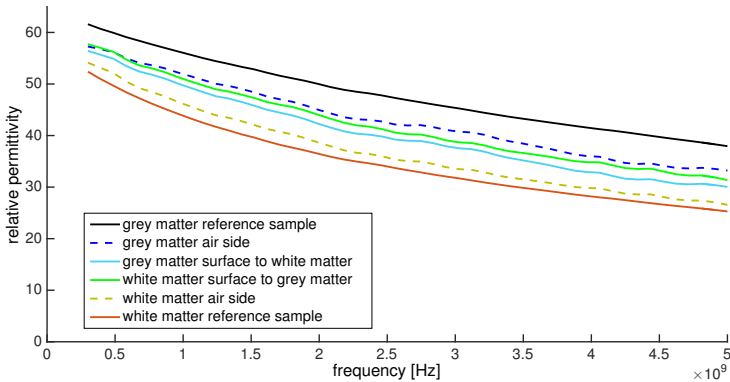


Figure 6.14: Measured permittivity of the sample with adhered layers and the reference sample (layers separately stored).

Second Examination The results of the first experiment which was made to examine the durability inspired a second experiment.

The second experiment was made to examine how long the diffusion lasts and how deep the diffusion zone would be. Due to the comparably long manufacturing process needed for a single sample, a measurement could at the earliest be made 4 hours after the start of the production. With all the layers the production in total lasted three days. Thus, the material has to last at least an additional fourth day in order to have one day to measure.

A series of 7 samples were made to examine the duration. Each day a new sample was produced and on the last day after the final sample solidified. We separated the layers from each other and measured the permittivity at the interface surfaces. By observing Figure 6.15 we can notice that the diffusion process is almost finished after the completion of the sample.

A last questions still remained open: Is the diffusion zone only a very localized phenomenon on the contacting surface or does it happen all over the sample?

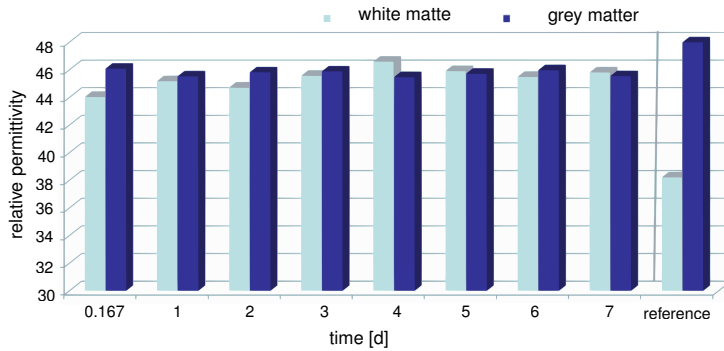


Figure 6.15: The resulting permittivity measured at 2GHz . The measurement was taken on the surface where the layers were connected. The reference is the permittivities of the separately stored layers.

Depth of the Diffusion Zone The penetration depth of the diffusion zone was examined on a sample with adhering layers. The samples were sliced into discs of 2.5mm thickness. After every cut the permittivity was measured. The result of the experiment for a single frequency is visible on the left side of Figure 6.16. We noticed that the diffusion zone reaches nearly all the way through the sample.

At this point we decided to introduce a non-conducting waterproof separating layer.

6.4.1.1 Investigation on the Influence of a Non-Conducting Layer

The first experiments with the aim to find out if a non-conducting layer can be used was made with a polyethylene film (cling film) with a sub millimeter thickness of about $16\mu\text{m}$. But we kept in mind that we later would need a material that could be easily fitted on a spherical surface. Furthermore, it could become important that at a later point of time a more realistically shaped phantom would be needed and thereby the non-conducting layer have to be affixed on a complex shaped surface. Hence, we examined a second material: Latex milk.

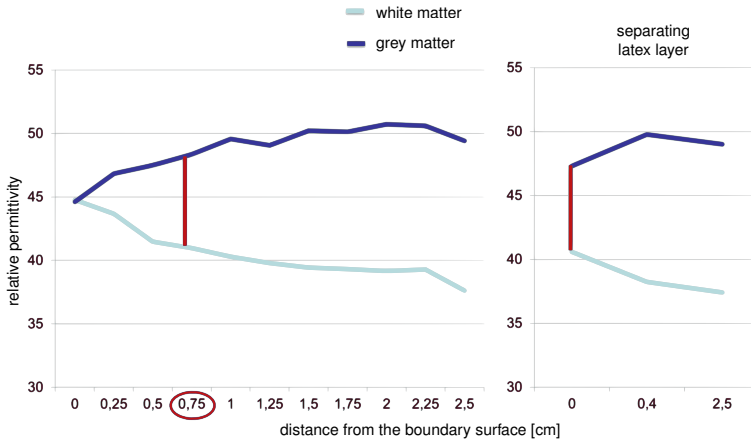


Figure 6.16: Examination of the penetration depth of the diffusion zone. The left diagram shows the measurement of a sample of two layers cast on each other with a white matter and a grey matter layer. The right diagram is of the same structure, except a film made of latex which is between the grey and white matter layer.

Simulation on the Non-Conducting Layer Before the above mentioned non-conducting layer could be included, another experimental test was needed. We had to verify, that the layer did not have a significant influence on the measured signals. Therefore two simulations were made. One of it contained a small PE film and the other did not.

The simulation was made with the same dimensions that we used during the real experiments described above. The sample consisted of a layer of a grey matter-representing material and another one representing white matter. The layers were of 6 mm thickness and had a diameter of 130 mm . The permittivity for the simulation was taken from the measurements described above. As a simulation environment we used SEMCAD³. The field was transmitted and received by bow tie antennas developed by M. Jalilvand [31]. The influence of the layer can be read from the scattering parameters. A reflection would influence the S_{11} and S_{22} parameters and deviations in the transmissions would be visible at the S_{21} and S_{12}

³A software for simulating electromagnetic field problems. The software is a product of the SPEAG Company, Zürich, Switzerland.

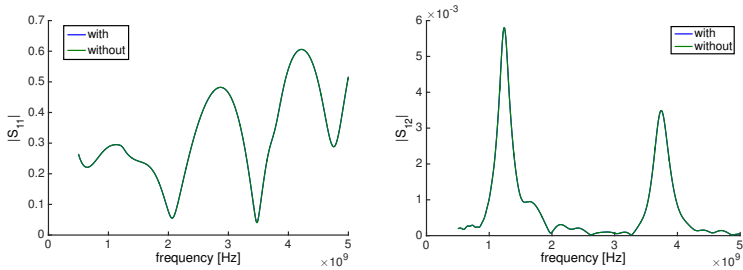


Figure 6.17: The S_{11} (left) and the S_{21} (right) parameters of the simulation made to verify that a very thin non-conducting layer (around $16 \mu m$) does not have an influence on propagating waves. The simulation was made by SEMCAD with a homogeneous permittivity neglecting dispersion.

parameters. In Figure 6.17 the results of the simulations can be examined. There was no difference between the simulations found. The graphs are exactly congruent. One limitation should be mentioned here that non-dispersive materials were used in the simulation. Hence, the complex permittivity we used was the permittivity at $2.5 GHz$. This could explain the second peak $3.8 GHz$ passing through the sample, an effect we could not detect during a real experiment (compare Figure 6.19).

Experimental Verification on the influence of Non-Conducting Layers. The same experiment as simulated above was repeated with real samples having the same dimensions. A cling film was used as separating layer. In our first experiment (shown in Figure 6.18) there were still some differences noticeable. So we made further experiments. We had to learn that the observed deviations were caused by small differences between the sample mixtures and their shapes. To examine this we started a new experiment where we introduced a gelatinous mass (later called matching liquid) with approximately the same permittivity as the skin mixture. The matching liquid was later used to improve the fitting of the antenna on the surface and to achieve a distance between the antenna and the sample. For this experiment we used the sample without the PE film in between and added a layer of the matching liquid with a thickness of $1 cm$ on top. A new PE film was brought in place between the matching liquid and the sample. After the first measurement the film was removed and the

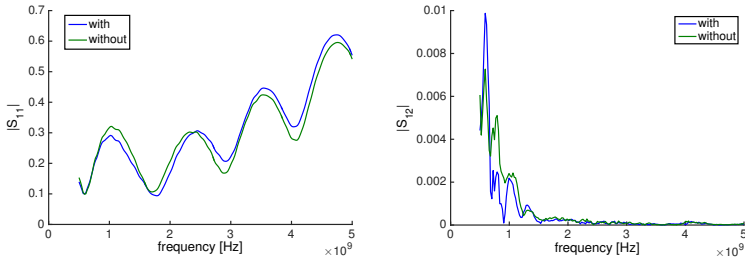


Figure 6.18: The S_{11} (left) and the S_{21} (right) parameters of the experiment made to verify, that a very thin (around $16\ \mu\text{m}$) non-conducting layer does not have an influence on propagating waves. Two samples were produced each with two layers made from mixtures for grey and white matter of $6\ \text{cm}$ thickness. In one of the samples the layers were separated by a PE film.

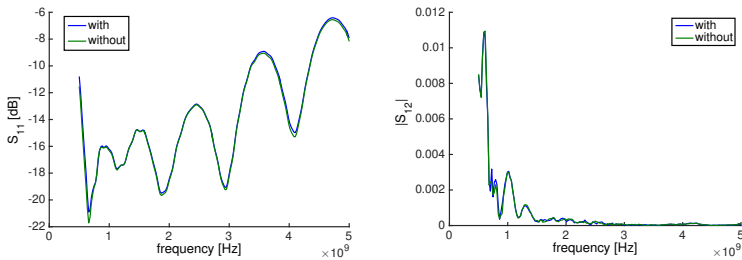


Figure 6.19: The S_{11} (left) and the S_{21} (right) parameters of the experiment, which was made to verify that a very thin (around $16\ \mu\text{m}$) non-conducting layer does not have an influence on propagating waves. The experiment was made with the sample without a barrier of PE film. During one of the measurements a new PE film was brought between the antenna and the sample. Therefore a layer of matching liquid was used to guarantee a good fitting of the antenna.

matching liquid level was compensated with more matching liquid. Then a second measurement was made. Figure 6.19 shows the result. We could not detect any difference between the two measurements. So we can state that we do not have to consider such thin layers during reconstructions and evaluations.

Remaining Diffusion on Latex Milk As we intended to use latex milk instead of PE film we had to redo the experiment with a layer of latex as

separator. Due to the way latex is processed, the layer we were generating was never completely waterproof. So we considered that a light diffusion could be remaining. The layer will hardly become waterproof as the vaporizing ammonia is leaving pores behind. To measure the extent of the remaining diffusion we sliced the sample after the experiment into discs as we did with the sample which was cast together (described above). The result is also plotted in Figure 6.16 (on the right). The red line marks at which depth the difference between the white and grey matter-mimicking material is equal to the sample directly cast together.

Three Algorithms for Stroke Diagnosis

Microwave imaging in the context of stroke diagnosis can only be useful if it is able to deliver fast results. Microwave imaging was never thought to be a replacement for well-established medical imaging systems like CT or MRI, rather it should result in a technology to support the ambulant preclinical treatment of victims suffering a stroke or even an anyhow-caused head injury with the risk of an intracranial hemorrhage. Therefore, it is important that the investigations focus on fast and reliable algorithms. The probably fastest algorithms for that task are beamforming algorithms. These kind of algorithms are mainly used in the field of ultrasound, acoustics or radar. In our opinion this is a good reason to take such algorithms into account.

Unfortunately, beamforming goes hand in hand with many approximations and simplifications and therefore the resulting images (later in this chapter) do not always lead to clearly interpretable results. Moreover, in case of an error, it is hard or even impossible to identify wrong results and separate them from good ones. A reason for us, to introduce a second algorithm and examine its ability to image strokes.

Hence, the second section of this chapter describes the functionality, implementation and verification of a Gauss-Newton-based reconstruction algorithm. This algorithm does not need to have additional (often unknown) information about wave propagation or underlying physical effects. This is

possible due to the encapsulation of field-specific calculation into separate simulations. Nevertheless, this benefit is usually traded against great computational efforts. Thereby, the required demand of hardware and computational performance to achieve a fast reconstruction is hard to fulfill.

Hence, a last algorithm is introduced (section 7.3). An algorithm, namely Contrast Source Inversion, that may serve both a minimum of approximations and a comparably fast reconstruction.

7.1 Delay and Sum Beamforming for Microwave Imaging

The idea behind beamforming is quite simple and in case of e.g. radar does not require too many approximations: If for example electromagnetic waves are propagating through a homogeneous medium, the velocities of the waves will be equal and independent from the direction as well as the orientation of propagation. Hence, the waves will spread in a spherical manner from the particular sources. For the beamforming, the homogeneity of the background is assumed. Moreover, the same velocity is used for all mediums and only single scattering is regarded. These assumptions are used in different ways for beamforming algorithms:

1. They are used to form a globally defined wave front of a different morphology, for example a plane wave. Therefore, the transmissions of the senders are synchronized in such a way that the superposition of the single waves will generate the intended global wave.
2. The assumptions are also used to focus on a single point within the examined object and therefore maximize the amount of microwave energy exactly there. By doing so, a selective warming of the aimed point can be reached. This is a technique that is actually under research and is intended to treat for example intracranial cancer [32].
3. The assumptions are also used to focus on unknown sources by delaying the received signals and therefore locate the sources themselves.

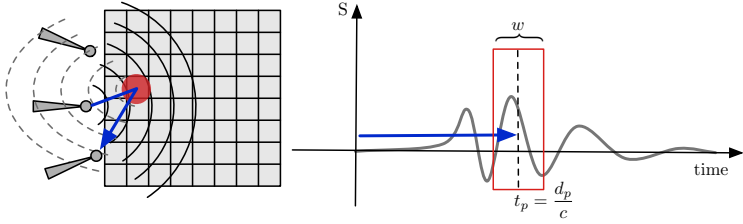


Figure 7.1: A schematic representation of the Delay And Sum (DAS) algorithm. The distance between the discrete points in the resulting image and the antenna pairs (transmitting and receiving antenna) are used to delay a time window. The window is then used to cut out the corresponding time sequence of the received signal. All cut-out signal parts are summed up and the achieved value is written through the corresponding point.

Combinations of the strategies described above are used for ultra sonic imaging, radar or even for microwave imaging.

7.1.1 The Delay and Sum Algorithm

The algorithm I was using did combine point two and point three of the above mentioned statements. First, the signals transmitted by all antennas were delayed in such a way that a single point was focused. However in our case not to heat the tissue but rather to achieve a strong reflection from exactly that point. In a second step the reflections from the previously focused point were windowed in time domain to cut out the potential reflection. As a last step, the cut-out signal parts were summed up.

Due to the principle of superposition, the measurement for each sending antenna can be made separately. The separate measurements are then saved in the form of scattering parameters and the whole procedure can be described in the following way:

1. Measure the scattering parameters in frequency domain for each transmitting antenna (marked with the index m) and each receiving antenna (marked with the index n) $S_{n,m}$ with $n, m \in \{1, 2, \dots, N\}$ and N the number of antennas. Inverse Fourier transform the signals to time domain ($\mathcal{F}^{-1}\{S_{n,m}\}$).

2. When all signals are acquired the area which should be imaged is discretized. Therefore a $K \times L$ -grid is defined for a two-dimensional example.
3. In the next step the distance between each discrete point $p_{k,l}$ (with $k \in \{1, 2, \dots, K\}$ and $l \in \{1, 2, \dots, L\}$) and each antenna position a_n is calculated.
4. In this step the propagation time $t(a_n, p_{k,l})$ to each point from every antenna is calculated which is not possible without a strong approximation (the homogeneity of the velocity). Usually the propagation times are therefore calculated with the velocity c of a wave that propagates through a medium with the average permittivity ϵ_a of all expected tissues:

$$t(a_n, p_{k,l}) = \frac{|a_n - p_{k,l}|}{c}, \quad \text{with} \quad c = \frac{\text{Re}\{\sqrt{\epsilon_a}\}}{c_0}, \quad (7.1)$$

where c_0 is the speed of light in vacuum.

5. Now, the propagation times are used to calculate the delay time $\tau_{n,m}(p_{k,l})$ for every point and antenna combination. The delay time is the sum of the propagation times from the source antenna to the actual focus point and the propagation time from that point to the receiving antenna.
6. The calculated delay times are used to move a time window w and cut out the correct signal parts.
7. All cut-out signal parts for the corresponding point are summed up and form the value $I_{k,l}$ in the result image.

Figure 7.1 provides a schematic visualization of the delay and sum algorithm.

Following the steps above, we can write

$$I_{k,l} = \sum_{n=1}^N \sum_{m=n+1}^N w(t - \tau_{nm}(p_{k,l})) \cdot \mathcal{F}^{-1}\{S_{n,m}\} \quad (7.2)$$

with

$$\tau_{n,m}(p_{k,l}) = \frac{1}{c} \cdot (|a_n - p_{k,l}| + |a_m - p_{k,l}|). \quad (7.3)$$

Having a closer look at equation (7.2) we notice that the second summation always starts with an index greater by one than the index of the

first summation. This was done to illustrate two things: First, each pair of antennas needs only one antenna to be transmitting. Due to the reciprocity theorem, the second direction (if the other antenna is transmitting) does not add any information. Hence, we do not have a benefit of adding these signals (except an improvement of Signal to Noise ratio by $\sqrt{2}$). Second, I used multi-static¹ signals. Additionally, it must be mentioned that the analytic signal without modification was directly used in equation (7.2). Using the analytic signal improved the spatial resolution, but also aggravated the robustness of the algorithm.

In addition to, or in some cases as a replacement for the window w , a weighting a is introduced to optimize the results. The weighting is for example used to compensate system-specific differences between propagation paths within the object and therefore to unify the responses achieved from the selected location [33]. This approach is used to include a priori knowledge.

The implemented beamformer used the described time window as well as a weighting for the values.

Weighting The weighting $a(\tau_{nm})$ was defined to amplify the data according to the time the corresponding part of the wave was propagating through the tissues:

$$a(\tau_{nm}) = (1 + r) \cdot e^{-Im\{\epsilon_a\} \tau(p_{k,l}) \cdot c}. \quad (7.4)$$

Due to the common definition of permittivity ϵ_a , its imaginary part is always negative. Hence, the term amplified the values exponentially over the calculated distance.

It must be mentioned here that I was not able to achieve good results when the weighting was active. The reason for this was that the side lobes gained strong influence due to the spatial expansion of the signals. Hence, I neglected the weighting. Better results were achieved using the time window only.

¹There are two ways signals can be measured: The so-called mono-static way, where the sending antenna is also used to receive the signal or the multi-static way, where the signal is received by a second not-sending antenna.

Time Window In general, the width of the time window d can be determined freely (from one single sample up to the whole signal). Generally, the goal of such a windowing is to improve the robustness of the algorithm compared to the usage of discrete points in time. Anyhow, I decided to define it depending on properties of the input signals. For my purposes I defined the width of the window depending on the frequency range B . In detail I summed up parts of the signals having the width of the main lobe of the sinc function. As I was operating on discrete signals I defined the discrete window width $d(B, \Delta t)$ by

$$d(B, \Delta t) = \text{round} \left(\frac{1}{B \cdot \Delta t} \right), \quad (7.5)$$

with Δt being the time step.

Frequency Window Another windowing was used for the algorithm. The signals were windowed in frequency domain. This window was always needed when scattering parameters were used in the frequency domain to limit the spatial expansion of the signals or moreover to attenuate the side lobes of the signal in the time domain. Therefore a Tukey window with a cosine lobe of about 10% of the total width on each side was used.

A Priori Knowledge Integration by Calibrating A priori knowledge can be integrated in different ways, not only by the above mentioned weighting. Another way to integrate a priori knowledge about the illuminated object is for example by using so-called differential signals. This kind of signal can be achieved by measuring at a different location and subtracting the signal there from the signal measured at the original location. It is only useful to do so if the object delivers comparable signals on both locations except for the deviation which should be imaged. We intended and also tried to use this procedure to subtract the scattering parameters of the right hemisphere from the one of the left hemisphere. Thus we used a calibration like this:

$$\mathbf{S} = \mathbf{S}_{\text{left}} - \mathbf{S}_{\text{right}}. \quad (7.6)$$

This type of calibration can also be interpreted as a background subtraction. It is capable of removing every scatter which is not needed as

long as the reference signal is good enough and the algorithm is robust enough to compensate for the remaining errors.

The ideal reference signal would be gained by a measurement of the now affected region made on exactly the same location, but before the stroke. Such a scenario is possible if simulations are used to generate the signals. To test the performance of this algorithm I simulated the set up twice, first with and then without the stroke. In that way I generated the measurement and the reference.

If not stated otherwise, a calibration of this kind was used for the results.

7.1.2 Implementation of the Algorithm

The algorithm was implemented in MATLAB's scripting language. Due to the rich number of ready-to-use functions and tools, MATLAB is an excellent environment for the development of this kind of algorithms.

The whole implementation can be separated into four main parts:

1. **Loading the Data:** To have the algorithm working a loading scheme for different data from different files was needed. The minimum amount of data necessary were the measurement data (including the calibration data) and data about the geometry of the used aperture or array. In addition to that a number of other data were necessary e.g. for preprocessing purposes.
2. **Preprocessing:** The calibration of the data was performed. For some experiments, it was necessary to transform the data from other data types so that the algorithm could work on one specific data type. Another thing implemented in the preprocessing part was the coordinate transformation of the antenna positions. As some simulations contained differing orientations of the coordinate axis it was necessary to alter the visualized area. To avoid this, a function to automatically transform the coordinates was introduced. An additional benefit of the automatic transformation was the fact that the tools to display the results no longer needed to be fitted. For the transformation, an additional file with translation and rotation information was introduced.

3. **Algorithm:** The delay calculation as well as the calculation of the image required helper calculations like the Fourier-Transform of the measurement data were made within the algorithm part. The Fourier-Transform was necessary due to the fact that the network analyzer as well as the simulations were usually returning frequency domain data.
4. **Displaying:** The displaying of the data was separated from the beamforming procedure. After the beamforming had been completed, the results were directly written to a file. This also offered the ability to remotely run the algorithm on more powerful machines.

All routines of the algorithm were written in separate functions. This allowed for easier debugging and a good modularity so that routines of the algorithm could be replaced easily.

7.1.2.1 Performance and Parallelization

Often it is possible to improve the computational performance of an algorithm by parallelization of the written code. This is especially true if the implemented algorithm contains many independent steps. In many cases a parallelization goes hand-in-hand with an increased amount of memory. This is especially true for MATLAB. The reason for this is the fact that many variables are copied for each separate process. The copying and conflating of variables cause a growing communication overhead which is reducing the benefit of parallelization.

Anyhow, with machines having multiple cores the fully provided performance is unreachable without parallelization. The easiest way to parallelize a task in MATLAB is to use the command `parfor`. It is a parallelized version of the default `for`-loop. Hence, wherever a `for`-loop shows up it can be replaced by the parallel version. But, due to reasons mentioned above, this is not useful for every case. Especially short tasks do not show any benefit when using `parfor` instead of `for`.

It is not always easy to predict, whether a replacement of the `for`-loop is beneficial. Hence, only try and error is often possible to figure that out. Certainly, a good rule of thumb is to parallelize loops with a long duration and a comparably low memory request for each loop run.

Table 7.1: Examination of the speed up achievable by parallelization. The table contains the measured times for each loop with and without parallelization. The unit of the values are seconds.

| Parallelization | DFT-loop | Index-loop | DAS-loop | total |
|-----------------|----------|------------|----------|---------|
| none | 0.824 | 0.368 | 418.777 | 419.979 |
| DFT-loop | 2.872 | 0.379 | 413.917 | 417.180 |
| Index-loop | 0.821 | 0.7821 | 400.335 | 401.948 |
| DAS-loop | 0.977 | 0.432 | 262.579 | 263.998 |

Performance Test on an Array with 27 Antennas The example I used to examine the performance of the parallelized code is introduced in section 7.1.3. The necessary measurement data were taken from a computer simulation. The simulation was performed in CST Microwave Studio 2015² and was computing 1001 frequency samples from 5 to 2.2GHz. The reconstruction was conducted on multi-static signals and a resolution of the reconstructed area was $100 \times 100 \times 50$ voxels corresponding to $200\text{mm}(x) \times 200\text{mm}(y) \times 100\text{mm}(z)$. Time windowing as well as calibration was activated (see section 7.1.1). For the timings stated later only the algorithm (step 3), neglecting loading and preprocessing, was measured.

The above mentioned algorithm as part of the computation contained three different tasks where each of them was performed by a separate loop. The first task was to transform the signals from frequency to the time domain by a Discrete Fourier Transformation (DFT), later called DFT-loop. To be more precise, the Fast Fourier Transformation (FFT) algorithm was used for the transformation. In a second loop the time delays for each point were computed and transformed to indices (later called Index-loop). The last loop comprised the time windowing and the calculation of the value for each point (later called DAS-loop). Now each of the described loops was computed one time with a normal `for`-loop and in another run with a `parfor`-loop. Here it should be mentioned that the computation steps often comprised multiple nested loops. All of the loops, even the nested ones, were tested. The best of each nested loop was then used in the comparison between parallel and serial computations of the DAS-Algorithm. Table 7.1 contains the result of this examinations. It can be observed that only the parallelization of the DAS-loop offered an improved

²A software to perform electromagnetic field simulation. The software is a product of the CST Computer Simulation Technology AG, Darmstadt, Germany

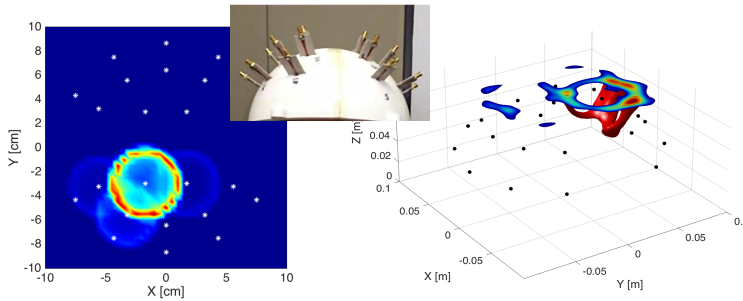


Figure 7.2: The result generated by mono-static signals. On the left there is the reconstruction of a single slice with the first implemented version and on the right there is the result of the new implementation. The uppermost slice on the right is the same layer as can be viewed on the left. In the middle there is an image of the array which was used for the measurement. The unit of the axes are cm and in the right image m . The right image is a surface plot illustrating 70% of the maximum value, where the black dots denote the antenna positions.

performance. The variation in the timings for the non-parallelized loops are thought to be a result of system-owned background processes.

7.1.3 An Array for the Algorithm

A first implementation of the algorithm was offered by M. Jalilvand et al. [34]. She worked at the Institute of Radio Frequency Engineering and Electronics (IHE) and developed the antennas as well as a first array (the small image in the middle of Figure 7.2). The array included twelve antennas on each hemisphere, with the antennas being of bow tie type. The antennas were a development by X. Li [35] and later improved by M. Jalilvand [36]. The measured object was a phantom as described in chapter 6. The result of the measurement is shown in the left image of Figure 7.2. The measured results were calibrated as described above.

Due to the fact that the algorithm provided by M. Jalilvand was not very flexible hindering the integration of new features the decision was made to implement a new version as described above. Additionally, the new version of the algorithm was capable of reconstructing a complete 3D area whereas the old version was only able to reconstruct single 2D slices. This advantage enabled me to view the result from more as one direction.

The reconstructed results yielded by the new implementation did not show the same image (Figure 7.2 in the right) as the results of the first version. It rather resembled a mismatch of single antennas. If it was a mismatch, the reason for it was probably the way the signals were measured. It has to be mentioned here that the signals were measured by hand and the antennas were not fixed to the array. Hence, deviations in location and orientation were possible. An improper fit of the antenna on the phantom surface was also possible.

Usually, a better interpretable response can be achieved by a better spatial resolution. One way to achieve that is to include more frequencies and thereby use a wider frequency band. If the findings of chapter 6 are recognized this is hardly helpful as the frequency range usable is limited by natural effects. The growing attenuation and the thereby limited penetration depth would remove most of the acquired additional information.

Another way to improve the response is to increase the sample rate on the surface of the object. In my case that means to improve the coverage by more antennas. As the beamformer works on reflections only I could move the antennas from one side of the array and use more antennas on the other side of the array.

With a python script arranging the antennas on a spherical surface, a new array was generated directly inside SEMCAD, the simulation software used at that time. The antennas were placed as close as possible to each other. The distances were similar as visible in Figure 7.3. Due to the fact that the surface of a sphere is not easily dividable into parts with the same shape and size I decided to define the distance between the antennas on the angles as they are known from spherical coordinates. The antennas, which have to be selected before, were arranged in rows and columns. Therefore, the increment for the polar angle was calculated by

$$\Delta\theta = \pi - \arccos\left(\frac{-r + h \cos(\alpha)}{\sqrt{h^2 + r^2 - 2 \cdot h \cdot r \cdot \cos(\alpha)}}\right), \quad (7.7)$$

with

$$h = \sqrt{3} \cdot r \cdot \Delta\phi_0 \quad \text{and} \quad \alpha = \frac{\pi - \Delta\phi_0}{2}. \quad (7.8)$$

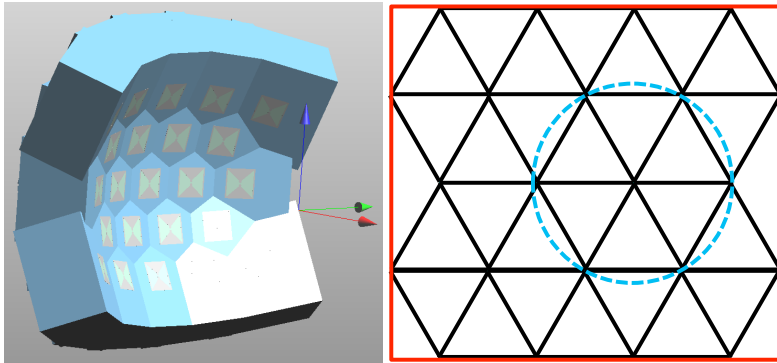


Figure 7.3: On the left, there is the figure of an example array with 23 antennas. It was defined by a strategy leading to nearly equilateral triangles. On the right a schematic view is given. It can be observed that this leads to the hexagon surfaces (marked with blue).

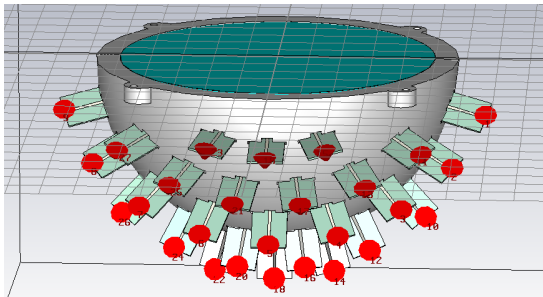


Figure 7.4: The new semiautomatically generated array with 27 bow tie antennas on the surface of a quarter sphere.

The increment was defined by the height of an equilateral triangle projected on the surface. Here, $\Delta\phi_0$ is the increment of the azimuth angle at $\theta = \frac{\pi}{2}$ and r is the radius of the spherical surface. $\Delta\phi$ was updated for each angle θ by

$$\Delta\phi = \frac{\Delta\phi_0}{\cos\left(\left|\theta - \frac{\pi}{2}\right|\right)}. \quad (7.9)$$

The extent of the array was defined by a maximum azimuth angle. By using the positions defined in that way an agglomeration of antennas at an

azimuth angle of $\pm\pi$ occurred. The redundant antennas were afterwards removed by hand. Figure 7.4 shows the array achieved in that way. In total, the new array had 27 antennas and was able to cover one of the hemispheres of the phantom (one half of the brain).

7.1.4 Examinations Made on the Way to Simulate the New Array

As mentioned before, the software used for initial simulations was SEMCAD. SEMCAD operates with voxel grids and calculates the electromagnetic field using the FDTD algorithm.

Due to the freely rotated antennas and their small conducting parts the simulations were growing very large and it was no longer possible to simulate the developed setups within a reasonable time. Another effect preventing a proper simulation was also related to the rotated antennas: They were no longer aligned with the axes of the coordinate system and hence, the waveguide source which was available in both simulation environments could no longer be used. The so-called waveguide source was used to simulate the behavior of a coaxial cable connected to the antenna. Without this port the only source usable for the antenna was the so-called “edge source”.

The Removal of the Feeding The edge source was able to provide a current or an electric potential to conducting parts connected to the source, whereas the waveguide port provided an electromagnetic wave itself. Hence, the waves an edge source would provide were highly depending on properly conditioned conducting parts (the antenna). As the antennas contained a feeding (meant to compensate the unsymmetrical behavior of the usually connected coaxial cables) experiments were needed to examine if the new source in combination with the antenna was working as expected. The experiment made to examine if the edge source could be applied properly comprised two simulations with respective experimental counterparts. Figure 7.5 shows images of the simulated setups. For the first simulation a sample with one layer of white matter between the two

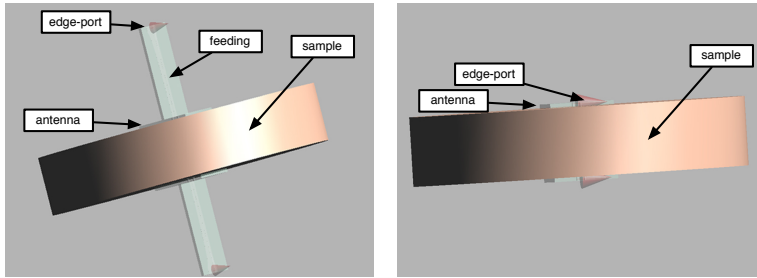


Figure 7.5: Images of the simulated setup. The left image contains a simulation with antennas and their feedings connected to edge source. The right image shows the same setup without the feedings of the antennas. The feeding was removed and the edge source was directly connect to the bow tie. In some simulations the cylindrical sample between the antennas was made of two materials.

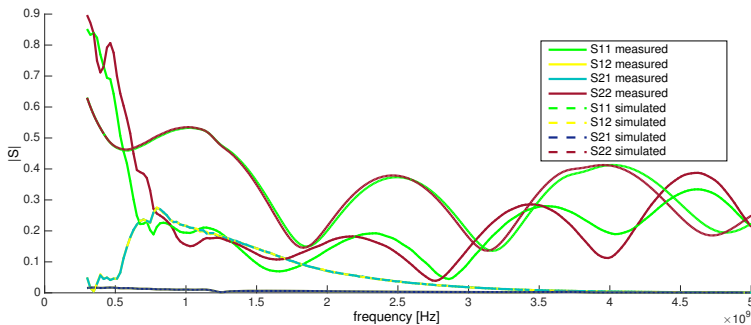


Figure 7.6: Comparison of a simulated scenario and a real measurement. The simulation contained the full antenna with the feeding in combination with an edge source. It can be observed that the energy passing trough the sample (S_{12} and S_{21}) in the simulated scene was almost zero which was not the case for the measurement.

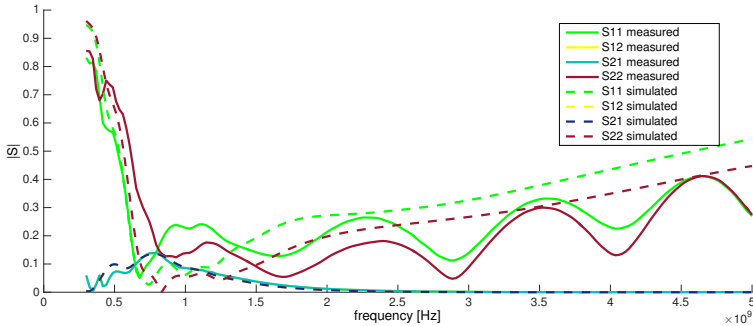


Figure 7.7: The results of the comparison between a real measurement and a simulation. The feeding of the antenna was neglected in the simulation. This leads to comparable amounts of passing energy through the sample of grey and white matter. Without the feeding no ripple over the frequencies was observed.

antennas was used. Both antennas contained their feedings. The sample was made of the materials as introduced in section 6.4. Then, a second simulation with a similar setup as the first one was conducted. However, the sample there was a two-layered sample of white and grey matter as described in section 6.4. A comparable setup is visible in the right image of Figure 7.5. To achieve more realistic results the simulated materials were dispersive. The measured permittivity of the manufactured real-world samples were used to set up the simulated materials. Of course, measurements of the real setup corresponding with the simulations described above were conducted: One measurement with a one-layered sample of white matter-like material and one measurement with a two-layered sample of white and grey matter-like material. The experimental setup is visible in Figure 7.8.

If we compare the scattering parameters (Figure 7.6) of the simulation with complete antennas and the scattering parameters of the corresponding measurement we can observe that in contrast to the experimentally measured S-parameters the simulated S-parameters do not show a proper amount of passing power (S_{21} and S_{12}). A similar result can be observed when comparing the amount of reflected power (S_{11} and S_{22}); a significantly higher amount of the introduced power was reflected. This was



Figure 7.8: The experimental setup of the two setups measured to examine if the feeding could be neglected in simulations. In the left image there is the setup used for the comparison with the simulation containing the feeding and in the right image there is the setup for comparing with the simulation where the feeding was neglected.

especially true for lower frequencies which otherwise showed a better ability to penetrate the phantom materials.

Comparing the simulation without the feeding and the corresponding measurement (observable in Figure 7.7) remarkable similarities can be observed. The transmitted power between the simulation and the measurement (S_{12} and S_{21}) is almost equal even if the reflected power (S_{11} and S_{22}) shows significant differences. For example the simulated S-parameters did not show the characteristic ripple. Generally, there were differences observable between the morphology of the reflected signals. The reflected signals of the simulation showed a higher amount of power, which can be interpreted to mean that the total amount of radiated power was lower compared to the real measurement. Due to the fact that the arriving power on the adjacent antenna (if compared with the measurement) is almost equal, it was assumed that the missing power was laterally radiated in the feeding. Due to the qualitative imaging character of the algorithm in combination with the calibration and despite the deviations observed I assume that neglecting the feeding would be a valid simplification for my purposes.

How to Simulate the Whole New Array Unfortunately, all the above introduced simplifications were not enough if FDTD was used and a simulation comprising the whole array should be made within reasonable

time. A simulation for a single excitation of one antenna took three days, which means that a whole simulation with all 27 antennas would take 81 days with the available computing power. In addition to that, we need to consider that a single simulation was not enough to achieve results. Hence, a second simulation for the calibration data was necessary and therefore another 81 days.

Due to this immense computational effort I was searching for alternatives. As the Karlsruhe Institute of Technology provides a license for another software to simulate electromagnetic fields (CST Microwave Studio) I then examined the abilities of this product. After some tests I found a way to go: To simulate the whole array with a complete phantom the reduced order model technique integrated into the frequency domain solver of CST was used. This solver operated on a triangle mesh and therefore did not need such a huge number of elements. By using this configuration the whole simulation was possible in less than a week.

7.1.5 Using Mono-Static Signals

Due to the unclear results achieved with measurements using the old 24 antennas array the experiment with the newly developed array was redone, using simulated data. Hence, errors, as expected during the experimental measurements described above, could be avoided. For the mentioned experiment, a second set of measured data for calibration purposes was needed. Therefore, a second simulation without the simulated stroke was performed. On the left side of Figure 7.9 the result of the reconstruction with mono-static signals is shown. It is hard to observe any response of the simulated stroke. Due to these results multi-static signals were used on further investigations. The right side of Figure 7.9 shows the results achieved by multi-static signals. The response of the stroke is clearly visible.

This even worked with ischemic brain tissues (Figure 7.10). To examine this, a simulation as described above was made but this time with a simulated stroke having the permittivity of ischemic tissues. The ischemic tissues were achieved by modifying the original permittivity of the stroke

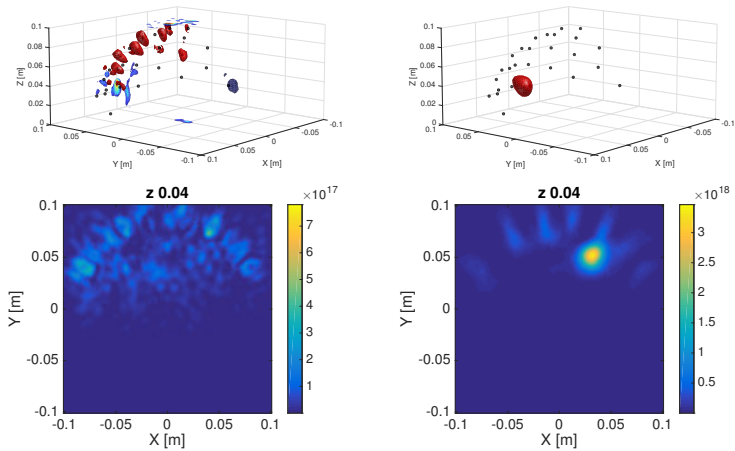


Figure 7.9: On the left side there are the reconstructions of multi-static signals and on the right side there are the reconstructions of mono-static signals. It should be mentioned, that the images in the lower part display views from the bottom upwards. The unit of all axes is m . The upper row are a surface plots illustrating 70% of the maximum value, where the black dots denote the antenna positions (Delay and Sum on simulated data and calibrated with a head without a stroke).

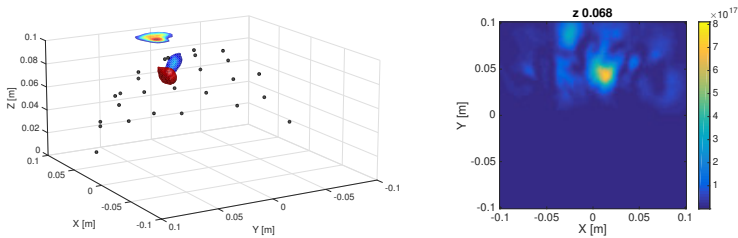


Figure 7.10: Reconstruction of an ischemic stroke located in the lower-middle part of the full phantom. The signals were calibrated by data of the same simulation without a stroke. The unit of the axes is m . The left image is a surface plot illustrating 70% of the maximum value, where the black dots denote the antenna positions.

region as described in section 3.3. The location of the stroke was also different. The stroke was located in the lower-middle of the array.



Figure 7.11: The array produced with the 3D-Printer. Unfortunately, the precision of the device was limited, so the work piece had hols and protrusions (left image). Hence, a rework was necessary.

7.1.6 Measurements on the New Array

Inspired by the findings from above, I built the new array as a real device. To do so I used the existing 3D construction from CST and exported it to a *step* file. This format was directly compatible with a 3D-Printer, which was available at the IHE. Hence, only minimal changes made within the CST simulation were needed to fulfill tolerances and then the array could be printed. Due to the imprecision of the device a rework on some areas was necessary (Figure 7.11).

Due to the limited dimension of the printer, the array was printed in two hemispheres: first the part with all the antennas and then the second part without antennas. The antennas had a loose fit within the array. Hence, to prevent a shifting of the antennas the antennas were clogged with silicone. At last, a holder for the array was constructed. The existing holder of the old array was not stable enough. The new holder had to be able to hold the weight of the array and the constructed phantom with about two kilograms. The holder was designed with the software, Inventor³ and manufactured by the workshop of the IBT (Figure 7.12).

Robustness of the Antennas After some experiments I noticed that the antennas were easily broken. This was often the case during the removing and fixing of the coaxial cables. To improve this, additional parts to hold the antennas were manufactured (on the right side of Figure 7.12, the black

³Inventor is a CAD software form Autodesk Inc.



Figure 7.12: The developed holder, which was able to hold the array and the phantom. It was stable enough to endure a great number of experiments. The holder was designed using the CAD software Inventor from Autodesk Inc..

and blue parts). Unfortunately, that was not sufficient. Hence, another solution had to be found. Three technical possibilities were intended:

- Improve the stabilization of the antennas.
- Improve the fixation of the cables.
- Use cables with less weight and less stiffness.

The first point could be reached by casting the whole antenna with epoxy resin. This was tested with two antennas of this kind. Therefore, the epoxy Epox 4305 together with the hardener 313 of the online shop PHD-24 was used. The relative permittivity of a sample of this material was measured to be 2.3. The material showed almost no dispersive effects and a very low conductivity. The measured permittivity value was used for a simulation of the epoxy embedded antenna. The comparison of the fields and the scattering parameters between a simulation with a normal antenna and a simulation with the embedded antenna did not show significant differences. Hence, the embedding was assumed to be valid. Two of these antennas were also manufactured and used for some student experiments. One example is the experiment to examine the non-conducting layer as described in section 6.4.1.1. However, the integration into the array was

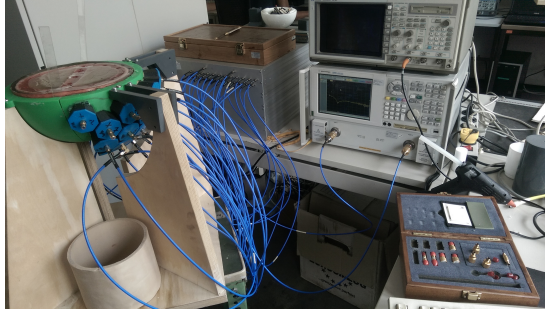


Figure 7.13: The complete measurement setup: in the rear left is the switch matrix, in front of it is the array and in the right is the network analyzer.

only possible if the array was rebuilt. Another disadvantage of casting the antennas into epoxy was the fact that the reusability of the antennas was limited. The second point, which meant to improve the fixation of the cables, could not easily be realized. Therefore, either spherically shaped metal sheet or alternatively a new set of smaller cables and a flat metal sheet attached to the holder would have been necessary. After having evaluated all options the technical possibility mentioned last was selected. The cables were replaced by more flexible and lighter ones. The final setup is visible in Figure 7.13.

7.1.6.1 Measurements Using the New Array

The measurement was coordinated by a software originally developed at the IHE. The software was written on C++ and Qt. It ran on a Laptop with a Microsoft Windows operating system. The tasks of the software was to control the measurement system, to switch the ports of the switch matrix bought for this project and to store the measured results into a text document. Nevertheless, some modifications were made to improve the usability and performance of the software. Thereby, the modifications were always related to findings I discovered during the experiments.

Calibration of the Switch Matrix The first feature addressed a problem with the mentioned switch matrix. This device was purpose-built for this

project. Unfortunately, some disadvantages were discovered. The paths of the signals through the device were not equally long. Hence, a method to compensate this was needed. First I intended to calibrate each channel combination with a SOLT⁴ calibration. Due to the 24 ports and by leaving out the equal port combinations, the number of separate calibrations were $24 \times 23 = 552$. As one calibration was at best taking 4 min, the calibration of the whole switch matrix took at least 36.8 hours. As this was thought to be a one-off event, it was done. Therefore, a feature was integrated to automatically open the calibration widget, switch to the correct port pair and after closing the widget, save the correction data to a specific file. The benefit of this feature was that the user does not need to define the file name by hand and therefore errors could be prevented. Unfortunately, this effort was useless. When the calibration process was completed, I discovered that the achieved correction data were no longer valid. The problem I observed was that the properties of the switch matrix were changing over time. Hence, a faster way to calibrate was necessary.

For the new procedure only one pair of ports was calibrated. After that, a measurement of the complete switch matrix without connecting anything was made. Due to the frequency range used the amount of radiated energy could be neglected, and hence, ports were approximated as ideal open ports. By dividing all achieved scattering parameters by the scattering parameters of the calibrated pair a set of correction data were generated. For this method temporally stable relative deviations between the paths were assumed.

Measurement Results During the last years several experiments with the measurement setup and the developed phantom were made. Unfortunately, I was not able to achieve sufficient results with this setup. The good results achieved by the simulations could not be replicated.

Nevertheless, two of the reconstructions and a description of the underlying experiments are offered here: For the first experiment, a full phantom with a hemorrhagic stroke located in the middle of the outermost area on one of the white matter hemispheres and in direct contact with the grey

⁴SOLT is the abbreviation of short-open-load-through and is a full 2-port-calibration.

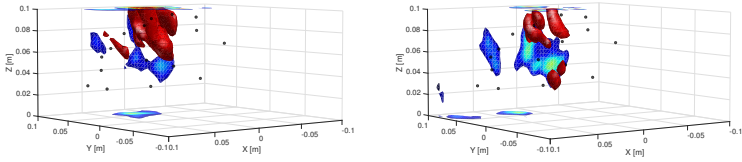


Figure 7.14: Both results were obtained by using the 60° measurements as reference for the calibration. The left image was achieved by the data of the 0° measurement and the right image by the data of the 30° measurement. Neither the response of the stroke is clearly observable nor the rotation between the two reconstructions. The unit of the axes is m . The images are surface plots, which illustrate 70% of the maximum value, where the black dots denote the antenna positions.

matter was measured. The first measurement was taken with the stroke in the middle (in a 90° angle to the gap between the two hemispheres). Then the phantom was rotated clockwise in steps of 30° size. After every step a measurement was taken. Hence, I obtained six measurements on a turn of 180° .

For the reconstructions I used one of the measurements to calibrate another data set. Two examples of the results are visible in Figure 7.14. The left image shows the result obtained by using the measurement of the 60° -rotated phantom as reference for the calibration, together with the measurement at 0° . The right image was achieved with the 30° measurements together with the 60° measurement as reference. Both of the reconstructions showed responses. Unfortunately, the responses were not very clearly located and the rotation could not really be identified. Hence, I cannot clearly say that the response was from the stroke or from inaccuracies within the phantom or the measurement setup. It should be mentioned that I measured only 23 of the antennas due to the limited number of ports the switch matrix provided (in total 24 ports). Therefore, two of the 27 antennas on each side were left out. Hence, the symmetric shape of the array could be preserved.

In the second experiment mentioned here, exactly the same should be done as was done with the simulated data. Therefore, a new phantom without a stroke was manufactured. In a first step the unchanged phantom was measured. The orientation of the phantom was similar to the above

described experiment. After that measurement a small amount of distilled water was injected. The water was brought in by a pipette as visible in Figure 7.15. Again, directly after the insertion of the water a measurement

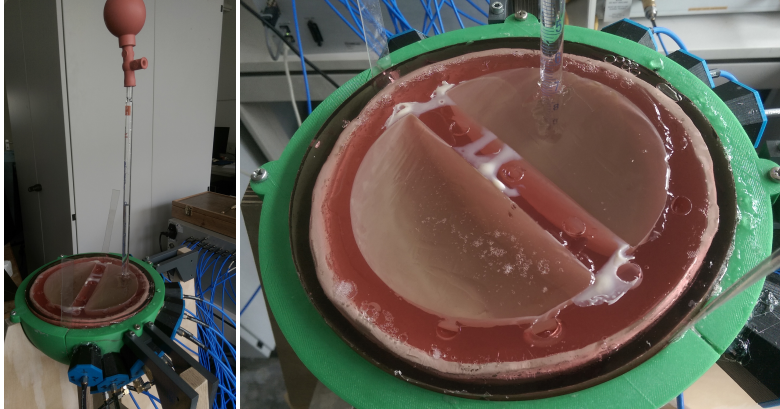


Figure 7.15: Measurement setup for an experiment where a small amount of water was applied through a pipette. The water was used to simulate a hemorrhagic stroke.

was made. Hence, nothing of the measurement setup was able to change much. Even if the water spread out or diffused into other tissues I ought have been able to visualize the differences.

For these measurements the full array with all 27 antennas was measured, despite the fact that the switch matrix had only 24 ports. To do so, three measurements were necessary at least. The first measurement was made as described above by neglecting four antennas. Then, the cables of four already measured antennas were removed and connected through the four antennas not included in the first measurement. After the second measurement the procedure was repeated with four antennas which were connected at both of the already-made measurements. After these three measurements all antenna combinations were at least measured one time.

The results are visible in Figure 7.16. It can be observed that a response at the correct position exists. Unfortunately, the response is not as clear as

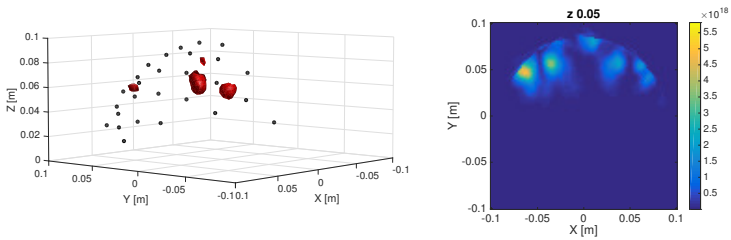


Figure 7.16: The results of the DAS algorithm from the measurement visible in 7.15. It can be observed that responses are visible at the correct position, even if they are not as good as on simulated data. The axes ticks are in m and the left image is a surface plot illustrating 70% of the maximum value, where the black dots denote the antenna positions.

I hoped it to find. If the way on how I received the results is recognized, better results should have been possible.

7.1.7 Robustness of the Algorithm

Due to the non-optimal results demonstrated in the section above further investigations to examine the robustness of the algorithm were made. The goal of the investigation was to learn more about how accurate the data for calibration has to be such that positive results could be achieved. Therefore several simulations were performed. Each of them contained different small deviations compared to the simulations made as measurement replacement. The deviations as mentioned before were of slightly different radii concerning the grey or the white matter. However, one of the parts contained a bit higher permittivity/conductivity than the other. This was done for a full phantom and also for a phantom including only grey and white matter both shaped as half spheres.

What was discovered during these examinations is visible in Figure 7.17 and Figure 7.18. Even small uncertainties within the data used to calibrate corrupted the results. This was especially true when a full phantom was used. Surprisingly, deviations in permittivity also showed a huge influence.

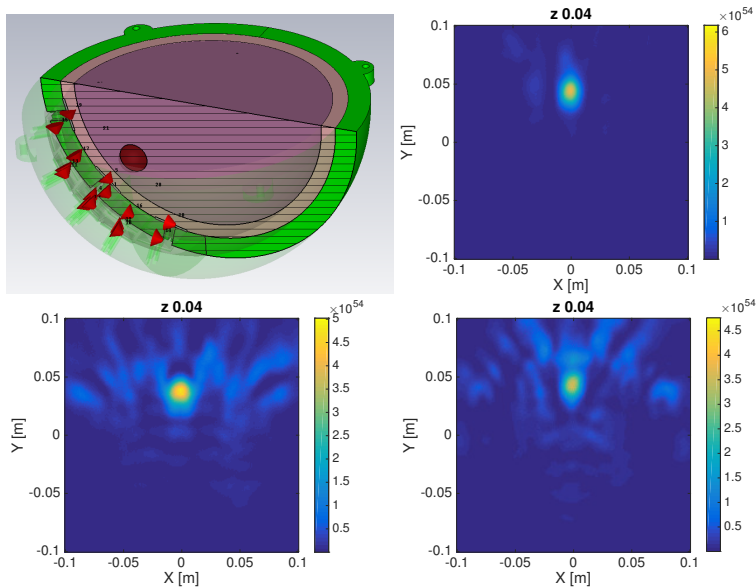


Figure 7.17: The results of an experiment with a more simplified phantom with a hemorrhagic stroke. The phantom does only have two layers. A cut through the simulation setup is shown in the upper left image. The simulation for the calibration was made with small disturbance in shape and also with deviations in permittivity. The upper right image was offered as a reference. It was calibrated without any deviations. For the lower left image the permittivity of the white matter was changed by 2%. And if calibrated with a phantom where the white matter was shifted by 7 mm the lower right image shows the result. The unit of the axes is m .

7.1.8 The DAS in the Context of Stroke Imaging

When reviewing all offered results of the DAS chapter the usability of the DAS algorithm for stroke detection is questionable. It must be kept in mind that strong simplifications were made for the phantom, especially the simplifications made concerning the morphology of the brain, which is unique for each human. Hence, the robustness would even be worse with real tissues. Thus, the usage of a simulation with a head model can possibly never be good enough to remove enough scattering.

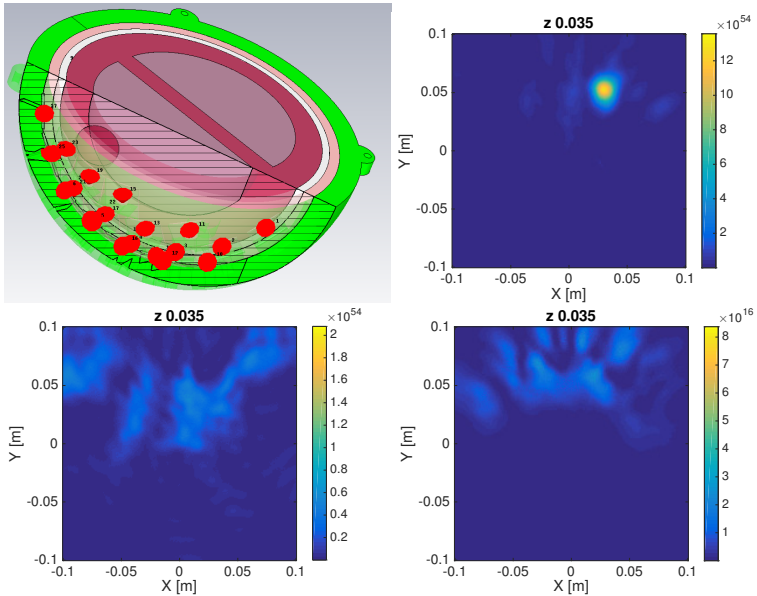


Figure 7.18: The same experiment as described in Figure 7.17, except of the phantom being a full one here. The upper images have the same content as before: on the left the measurement setup and on the right the reference. The lower left image was obtained with a calibration deviating regarding permittivity. Therefore, the white matter was changed by 2% and the lower right was made by a shift, but this time a shift of 0.5 mm was enough to disturb the image that much. The unit of the axes is m .

7.2 Blackbox Reconstruction with a Gauss-Newton Optimization

In contrast to the qualitative algorithm introduced in section 7.1 a quantitative reconstruction algorithm is introduced here. For the algorithm, a Gauss-Newton approach was used to reconstruct the permittivity distribution of a region between the antennas. Inspired by the publication of Rubæk et al. [37], an algorithm was implemented. For the implementation different software packages were included. In our implementation a framework called Meep⁵ for the electromagnetic field calculation [39],

⁵There is no unique definition for the term Meep. The authors offered different meanings, for example Maxwell's Equations for Every Person or Many Eggheads Earn

a framework called PETSc⁶ for the optimization [40–42] and the boost libraries [43] for the soft skill tasks, such as loading the settings and saving some results to a file, were used.

7.2.1 The Objective Function

The objective function f for my Gauss-Newton optimization was the L_2 -Norm of the difference between a measurement vector \mathbf{b} and the results obtained by simulations $\Phi(\mathbf{x})$. The simulations can also be called forward calculations. Thus, the objective function can be written as

$$f(\mathbf{x}) = \|\Phi(\mathbf{x}) - \mathbf{b}\|_2. \quad (7.10)$$

And the problem which should be solved can be written as

$$\mathbf{x} = \underset{\mathbf{x} \in \mathbb{D}^N}{\operatorname{arg\,min}} f(\mathbf{x}) \quad (7.11)$$

with $\mathbb{D} \subset \mathbb{C}$ and N the number of elements of the argument vector. Here, the elements are the complex permittivities of the voxels between the antennas. Hence, the definition range for the elements of $x_j := x'_j + ix''_j$ is

$$\begin{aligned} \{x'_j \in \mathbb{R} \mid 1 \leq x'_j < \infty\} \\ \{x''_j \in \mathbb{R} \mid -\infty < x''_j \leq 0\} \end{aligned} \quad (7.12)$$

with i the imaginary unit. An example can be seen in Figure 7.20 where the number of elements was $N = 49 \times 61 = 2989$.

Limitation of the Parameters Due to the physical meaning of the parameters a well-known domain of definition exists and has to be regarded. Otherwise, simulations or better forward calculations would diverge and never produce proper results.

Prestige. But probably the most common one is MIT Electromagnetic Equation Propagation. This definition offers also a hint to the origin of the framework (Massachusetts Institute of Technology) [38]

⁶PETSc is an abbreviation for „Portable, Extensible Toolkit for Scientific Computation“

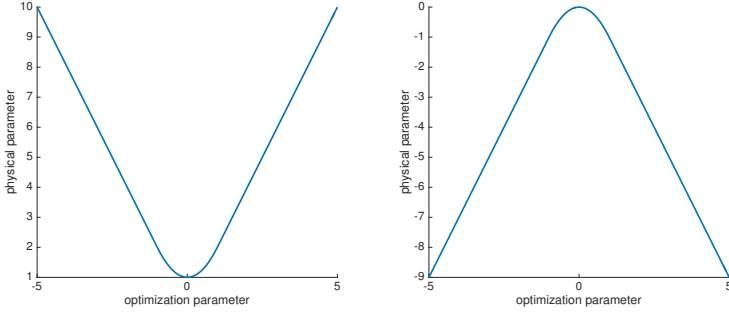


Figure 7.19: The introduced parameter transformations; on the left the transformation of the real part and on the right the transformation of the imaginary part. The transformation is quadratic on the interval $[1, -1]$ and linear on the remaining range.

Hence, a way had to be found to ensure that the parameters will stay inside the domain of definition with each iteration. With the first implementation of the algorithm, the values of the parameter were simply set to the value of the corresponding limit if the ranges were exceeded. As this left an edge to the otherwise smooth optimization function I intended to find a more mathematical definition for this. Therefore, a parameter transformation for the real part and the imaginary part was introduced, respectively. The real part was transformed by

$$\operatorname{Re}\{p_p\} = \begin{cases} 1 + \operatorname{Re}\{p_o\}^2, & |\operatorname{Re}\{p_o\}| < 1 \\ 2 \cdot |\operatorname{Re}\{p_o\}|, & |\operatorname{Re}\{p_o\}| \geq 1 \end{cases} \quad (7.13)$$

and the imaginary part was transformed as follows:

$$\operatorname{Im}\{p_p\} = \begin{cases} -\operatorname{Im}\{p_o\}^2, & |\operatorname{Im}\{p_o\}| < 1 \\ 2 \cdot (|\operatorname{Im}\{p_o\}| - 1), & |\operatorname{Im}\{p_o\}| \geq 1 \end{cases} \quad (7.14)$$

A graphical representation of the above-mentioned transformations is visible in Figure 7.19. I decided to use a transformation based on the absolute value of the corresponding part. The definition of the absolute value was used to avoid influencing the convergence of the algorithm by a quadratic transformation.

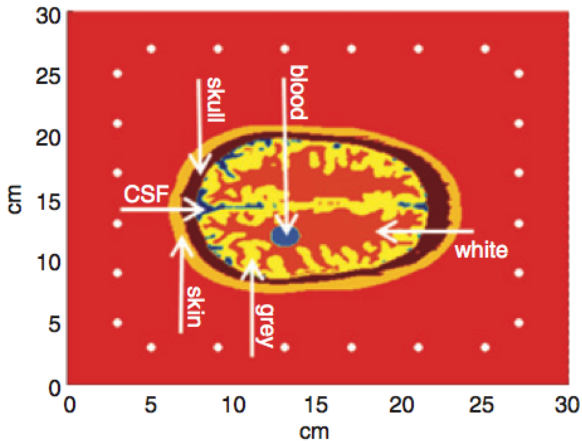


Figure 7.20: The setup used to generate the input data for the Gauss-Newton-based reconstruction. The white dots mark the source points for the waves.

7.2.2 The Forward Calculation with Meep

It should be mentioned here, that I did not start with an empty sheet when beginning with the implementation of this algorithm. Similar to the DAS project this project had also already been started by M. Jalilvand et al. [44]. The implementation was made in C++ and includes the framework Meep and the Boost libraries. In this section, we will concentrate on the way the simulations were achieved.

For the simulations a model of the measurement setup was needed. The model was represented by a single class. It delivered the relative permittivity and the conductivity of an arbitrary point within the area defined as simulation region whereas the data of the model was stored in a separate, independent two-dimensional voxel grid.

The setup contained a shape of a human head between and in the middle of the antennas. Figure 7.20 shows the simulation setup with the positions of the antennas and the head as it was used. The visible setup was bounded by multiple invisible voxel rows of absorbing material. The material, called perfectly matched layers (PML), was provided by Meep. We found a number of 10 rows as sufficient for our purposes. The head

Table 7.2: Material properties of the tissues we used for the forward calculation. The values were taken from the database of tissues provided by the ITIS Foundation[22], for the corresponding frequency of 1 GHz.

| tissues | relative permittivity | conductivity (S/m) |
|---------------|-----------------------|--------------------|
| skin | 45.71 | 0.88 |
| skull | 12.36 | 0.155 |
| CSF | 68.44 | 2.45 |
| grey matter | 52.28 | 0.98 |
| white matter | 38.58 | 0.62 |
| stroke(blood) | 61 | 2 |
| background | 45 | 0.5 |

was a single slice of the visible man (a computer model of a human being generated at the IBT [45]). As frequency we used 1 GHz, we also used the permittivity of the tissue (Table 7.2) at this frequency.

The 24 white dots mark the positions of the source points for the waves. To perform a simulation, the setup was separated into 24 independent subsimulations. In each subsimulation, a single point-source was active. A point-source was defined as a spotty sinusoidal electric current. Hence, the source point transmitted a two-dimensional circular and monochromatic wave. The wave had only an electric field component perpendicular to the simulation plane. For the first examinations an FDFD-solver available in Meep was used. This solver delivers the steady state after converging. Of course, the steady state cannot be reached exactly. It can only be calculated with a relative accuracy. For my simulations I selected an accuracy of $1e - 8$. It should be mentioned here that this is not the accuracy of the measured field but the accuracy used for solving the underlying linear problem.

After the calculation had converged the values of the fields were read out at the remaining, not-sending antenna positions. In total $M := 24 \times 23 = 552$ values for the result vector \mathbf{E} were obtained. The same was done for an empty reference simulation without the head but with the same antenna configurations. The elements of the reference vector \mathbf{E}_r were used to calibrate the elements of the result vector by subtracting

$$E_{S,j} = \frac{E_j - E_{r,j}}{E_{r,j}}. \quad (7.15)$$

7.2.2.1 Switching to the FDTD-Solver

Unfortunately, the available FDFD-Solver did not always converge properly and hence, the reconstruction was randomly aborting. To overcome this, I decided to switch to the more robust FDTD-Solver.

The implementation of the FDTD-Solver available in Meep is connected to a single function which, when called, calculates a single time step forward. Due to the way the solver had to be used, a stopping criterion was needed.

In general if the steady state is reached, the magnitude of the field does no longer change at any location. Hence, I used this and the fact that only discrete points were of interest to form the new criterion.

The algorithm was stopped if the sum of the difference between the absolute values of the field from current time step and the absolute values of the previous time step over a quarter period fell below a threshold. The error term for a single point $j \in 1, 2, \dots, N$ is

$$e_j = \sum_{k=a}^K (|E_j(t_{k-1})| - |E_j(t_k)|). \quad (7.16)$$

with K the number of discrete time steps within the quarter period and a the current time step. In detail, the values acquired in this manner were used to form an error vector \mathbf{e} and the element with the maximum value was then compared to the previously defined accuracy. As the transmitting point was ignored for the stop criterion and all other fields were zero in the beginning, the algorithm would have stopped before the field had arrived at any of the receiver points. In addition to the stop criterion a second criterion was introduced: The check was set to rest for a fixed time period after start.

Due to the simulation in the time domain and also due to the new stop criterion, the time periods of subsimulations were not longer equal and hence, the values lost their phase similarity. To correct the phase, the simulation time was used to “turn back” the values to time zero. This could be done by multiplying each value with

$$e^{i\omega T_s}. \quad (7.17)$$

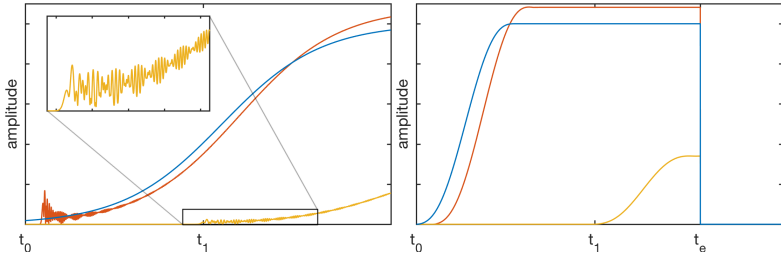


Figure 7.21: Excitation of a point source as available in the Meep framework. The left image shows the default excitation with the hyperbolic tangent function to smooth the switch in this event. The blue curve represents the current and the red graph the field at the source point. The field at a certain distance is colored in yellow. The right image shows the same experiment after replacing the smoothing function by a polynomial of fifth order.

T_s is the simulation time. Due to the definitions inside Meep, the correction was made with a positive time value.

7.2.2.2 Optimizing the Convergence Rate of the FDTD-Solver

After the introduction of the FDTD-Solver, as described in the previous section, a significant increase in convergence time was noticed. The findings of this section were originally achieved in cooperation with Micha Pfeiffer [46].

The amplitude of the field oscillated after the source had been switched on. This behavior was related to the implemented “switch on event”. A source was represented by the function $A \cdot e^{j\omega t}$. Thus, an event comparable to a step input to a system that is free to vibrate happened if the field or better the field inducing current was switched on. To circumvent this, the Meep library also offered the ability to smoothly switch on the source. In that case the step was smoothed by a shifted hyperbolic tangent. However, due to the asymptotic form of the hyperbolic tangent the magnitude A as well as the start value 0 can never be reached. Due to this smaller steps remained. The residual oscillations caused by the remaining steps increased the duration of the simulation. The residual oscillations can be observed in the left image of Figure 7.21. Due to the huge number of simulations which must be performed with each iteration a lot of time could

be saved by a faster convergence. To achieve that, the hyperbolic tangent was replaced by a polynomial of fifth order. The polynomial was fitted between zero and one. This polynomial guaranteed a smooth field function and also a smooth derivative of the function. With this modification the source function can be written as

$$s(t) = \begin{cases} h\left(\frac{t}{t_d}\right)Ae^{i\omega t}, & t \leq t_d \\ Ae^{i\omega t}, & t > t_d \end{cases} \quad (7.18)$$

with

$$h(t) = (-10 + (15 - 6 \cdot t) \cdot t) \cdot t^3 \quad (7.19)$$

for the polynomial and t_d for the switch-on-smoothing time.

This change allowed a much faster switch-on time nearly without oscillation. The result can be observed in the right plot of Figure 7.21.

7.2.3 The First Derivative of the Function

The first derivative of a multidimensional function can be written by a so-called Jacobi matrix. The elements of the Jacobi matrix are the partial derivatives of the function. If we are working with discrete values, the Jacobi matrix can only be approximated for discrete points. To approximate a derivative we need at least two points for a forward difference operator (section 2.1.1). To limit the computational effort the forward difference (equation (2.5)) to approximate the partial derivatives of the function was used. Due to the fact that the used function was a relation of the type $\Phi : \mathbb{C}^N \rightarrow \mathbb{C}^M$ at least 2989 complex derivatives were needed. As mentioned before a basic implementation already existed but with an approximation of the derivative by the following approach: If $x_j := x'_j + ix''_j$ was the current value we would approximate the partial derivative using forward difference by

$$\frac{\partial \Phi}{\partial x_j} \approx \frac{\Phi(x_j + h \cdot x'_j) - \Phi(x_j)}{2 \cdot h}. \quad (7.20)$$

Due to this definition of the approximation, the step width depended on the dimension of the real part of the complex permittivity. For the derivative the imaginary part was ignored. To achieve equally weighted derivatives

and to include the derivative of the imaginary part a more reliable definition of the derivative of a complex function was used [47]:

$$\frac{\partial \Phi}{\partial x_j} = \frac{1}{2} \left(\frac{\partial \Phi}{\partial x'_j} - i \frac{\partial \Phi}{\partial x''_j} \right). \quad (7.21)$$

Due to this modifications the computational effort needed for the Jacobi matrix was doubled. In addition to that, the number of unknowns was doubled, too and this led to an increased number of iterations necessary for convergence.

7.2.4 The Regularization

As the problem is generally ill-posed and the linear system to be solved in every iteration is often near to singular, a regularization to solve the underlying approximative linear system was necessary (equation (4.12)). The definition of the regularization that was used within the original implementation was inspired by a publication of N. Joachimowicz et al. [48]. The regularization parameter λ as mentioned in equation (4.13) was calculated by

$$\lambda = \alpha \cdot \frac{1}{N} \cdot \text{tr}(J^H J) \|\mathbf{r}\|_2^2, \quad (7.22)$$

where $\text{tr}(J^H J)$ denotes the trace of the matrix $J^H J$ and α was freely selectable.

But after the integration of the newly formulated derivative the linear problem, to obtain the optimization direction, was not always solvable despite the regularization. To overcome that a new regularization formulation was defined. The new formulation used the lower limit for the conditioning number

$$\kappa(J^H J) \geq \frac{\max_i |[J^H J](i, i)|}{\min_i |[J^H J](i, i)|}, \quad (7.23)$$

where $\max_i |[J^H J](i, i)|$ denotes the absolute value of the maximum element from the main diagonal and $\min_i |[J^H J](i, i)|$ denotes the absolute value of the minimum element. The limit was derived from Geršgorin's theorem [49] and the fact, that the condition number can be calculated by

$$\kappa(A) = \frac{|\lambda_{\max}(A)|}{|\lambda_{\min}(A)|} \quad (7.24)$$

for a normal matrix A . $|\lambda_{\max}(A)|$ and $|\lambda_{\min}(A)|$ are the maximum and the minimum eigenvalues of A respectively. Hence, my new regularization term was

$$\lambda = \alpha \cdot \frac{\max_i |[J^H J](i, i)|}{\min_i |[J^H J](i, i)|} \|\mathbf{r}\|_2^2. \quad (7.25)$$

After the introduction of the new regularization the linear problem to be solved in order to achieve the optimization direction, could be solved again.

7.2.5 Performance and Parallelization

Just from the beginning onward the parallelization of the code was unavoidable due to the huge number of simulations for each iteration and the expensive calculations linked with it. Even the first implementation was parallelized and hence, it included strategies for inter-process communication. The first implementation communicated with default output and therefore the communication was string based. To allow for this, pipes were used to link the different processes with local machines. To link the processes with remote machines, pipes over Secure Shell (SSH) were used. In addition to that, Meep is able to use the Message Passing Interface (MPI) to communicate between processes, which could be used to achieve a further scaling of the computations. This strategy was only usable for clusters with direct user access to each cluster node. The parallelization was also only used to parallelize the derivative (the Jacobi matrix). To improve the performance in a further way a new way of parallelization using MPI only was introduced. While changing the parallelization the framework PETSc was included.

Although this framework has many optimization abilities, the one I intended to use was missing. The framework did not provide a Gauss-Newton algorithm. Due to the fact that this algorithm had already been tested and that it worked properly, I decided to integrate it into the PETSc framework. The framework also provides parallelized solvers for linear systems and therefore offers the ability to switch from the serial LU factorization, as used in the first implementation, to a parallelized version or even to a parallelized Conjugated Gradient (CG) method.

For the parallelization of the simulations and the derivative a custom splitting procedure was implemented. The strategy I was following was not exactly comparable to the well known master-slave concept. Each node calculated its one portion to compute. The global MPI-communicator was split into subcommunicators for each antenna and therefore, also for each subsimulation. As the subsimulations were independent from each other, this reduced the communication overhead and hence, improved the overall performance. But this could only be done if the number of nodes at the global communicator was greater than the number of antennas. If this was not the case the program assigned the antennas to the available nodes.

A similar thing was done for the derivative and therefore for the number of unknowns. However, I did not have access to a cluster with enough nodes to reach the case where the number of nodes was greater than the number of unknowns.

7.2.6 Imaging results

The imaging was done by first simulating the setup described above with Meep forward and then by an inverse calculation with the described Gauss-Newton approach. The result M. Jalilvand obtained by the first implementation can be observed in Figure 7.22 and the results achieved by the new implementation are shown in Figure 7.23.

It should be mentioned here, that the background material for the test with the old software was different compared to the test made with the new software. The background material had a permittivity of $45 - i8.9876$ comparable to the permittivity of skin but with a lower conductivity. For the test with the new implementation the background was set to the permittivity of water ($70 - i8.9876$).

It is obvious that both implementations were capable to image the hemorrhagic stroke. But the performance was quite different: The new implementation was capable to compute on 96 cores and hence, to compute 15 iterations within 24 hours, even despite the doubling of necessary forward calculations. Whereas the old implementation was limited by

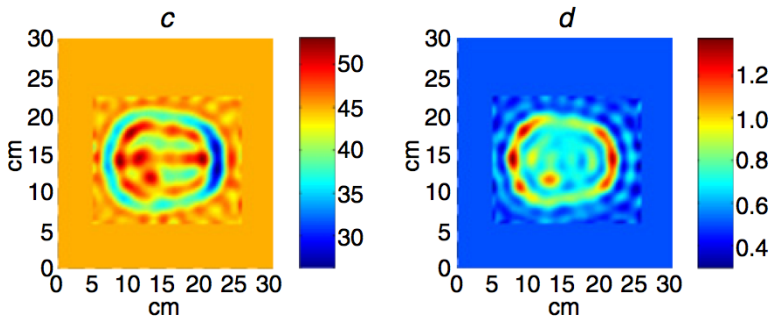


Figure 7.22: The resulting reconstruction after having forward calculated with the Meep and backwards with the first implementation of the Gauss-Newton-Method. The simulated measurement setup is visible in Figure 7.20. This image was reached after 10 iterations with a residuum of 0.0682052 (c is the real part of relative permittivity and d the conductivity)

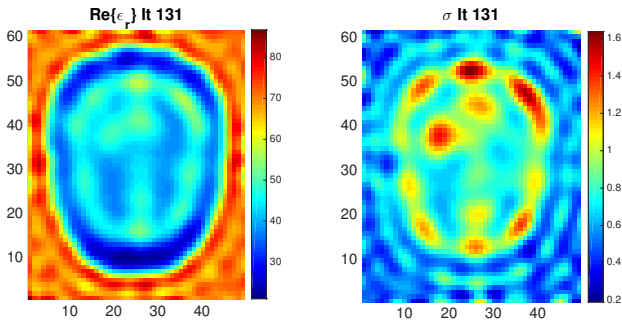


Figure 7.23: The results of the new implemented Gauss-Newton algorithm after 131 iterations. A residuum of 0.1285 was reached. The measurement setup was equal to the setup known from the first implementation despite of the background material. As background material water was chosen. The size of the quadratic voxels was $3,33\text{ mm}$ and the original permittivities can be taken from Table 7.2 except from the background permittivity (water $70 - i8.9876$)

several facts through a smaller amount of cores and therefore the fastest configuration required at least one week to calculate 15 iterations.

However, the results of the first iteration was achieved after 10 iterations with a residuum of 0.0682052. The second result was achieved after 132 iterations with a residuum of 0.1285. It must be mentioned that the residuum within the first implementation was normalized to the square root of the number of parameters. Without this normalization the residuum of the first implementation was 3.72889. Additionally, it must be mentioned that the result did not change much after iteration 60 with the new implementation.

7.2.6.1 Sensitivity of the Parameters

An expectation about the sensitivity of the parameters can be derived by examining the computed Jacobi matrix (Figure 7.24).

It can be noted that there are generally low values ($\times 10^{-4}$ on the color bar) in the Jacobi matrix and a great number of the values are almost zero (almost all of the matrix is colored in blue). An image as visible in Figure 7.25 can be achieved if a single row of the Jacobi matrix is extracted and reshaped to a 61×49 matrix. Those images can be used to analyze the influence, a small change of the voxel value would have on the field which

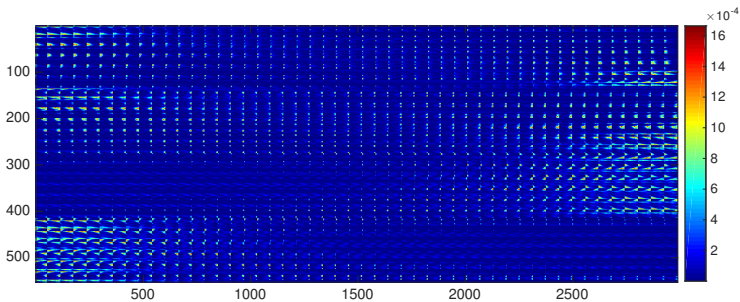


Figure 7.24: Illustration of the absolute value of the Jacobi matrix of the iteration 131 as it was calculated by the new implementation. When comparing with the color bar it can be noted that the Jacobi matrix generally contains low values ($\times 10^{-4}$). A great number of the values that are almost zero (all blue elements) is also notable. Hence, a change of one of the values does not have a great influence on the measured fields.

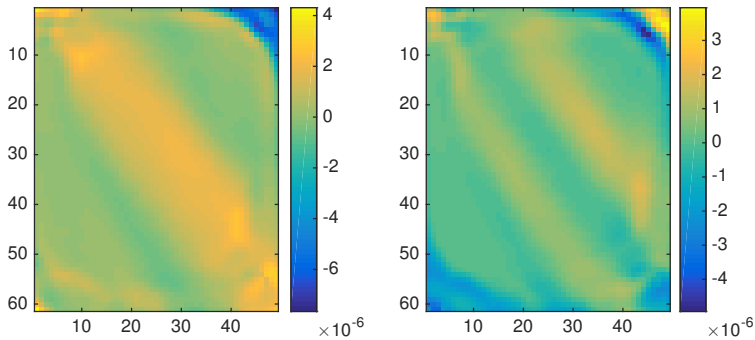


Figure 7.25: A reshaped graphical view of the eleventh row of the Jacobi matrix of iteration 0. It can be used to observe the influences small changes of voxel values would have on the signal of the corresponding antennas pair (opposite antennas; position 0 and 12). The left image shows the real part of the complex derivative and the right image the imaginary part. The size of the quadratic voxels were 3,33 mm.

can be measured by the corresponding antenna pair. If we look at Figure 7.25, for example it is obvious that this combination of antennas (opposite antennas; on position 0 and position 11) was comparably sensitive to the inside of the head. A different observation could be made by examining the images in Figure 7.26. This image illustrates the influence of adjacent antennas (position 0 and 1). The inside of the head had almost no influence on the measured field values. In general it could be observed that a single voxel did not have a significant influence on the signals at all.

As generally low values were observed, the sensitivity against small changes is low, too and therefore small differences in permittivity will be hard to visualize. An improvement was achieved with the usage of the matched background material but not significantly enough to enable a good imaging of ischemic tissues.

7.2.7 Results in the Context of Stroke Diagnosis

The main disadvantage of this algorithm was the huge amount of computational effort necessary to converge. This made the mobile application

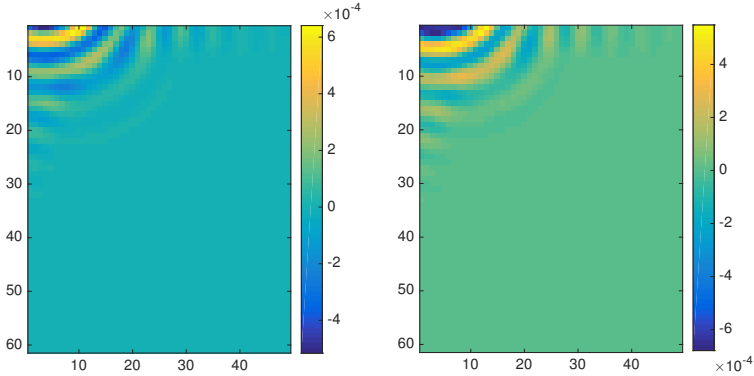


Figure 7.26: The reshaped graphical view of the first row taken from the Jacobi matrix 7.24. It can be observed that voxels from inside the head do have a minor influence on signals from these two antennas (adjacent antennas; position 1 and 2). The left image shows the real part of the complex derivative and the right image the imaginary part. The size of the quadratic voxels were $3,33\text{ mm}$.

of such an algorithm at least doubtful. Especially, if we remember that a two-dimensional example was reconstructed here. If the algorithm was used with data of 3D simulations, the results were poor and the details were smoothed out. The reason for this was that the incident fields were based on the two-dimensional fundamental solution and not on the three-dimensional fundamental solution. This means that the propagating fields experienced a different damping. Additionally, all 3D simulations contained antennas and a single point source cannot represent the complex field of the real antenna.

To overcome this, models of the antenna can be integrated into the forward calculation. However, this would increase the number of necessary voxels significantly.

7.3 Contrast Source Inversion for Stroke Imaging

The Contrast Source Inversion (CSI) method is the third and last method we examined for suitability for stroke diagnosis. The method was originally published by van den Berg and Kleinman [50]. The CSI method is tightly linked to methods named modified gradient methods and can be interpreted as a further development of them. The biggest advantage of those methods is that forward calculations via numerical solvers are avoided. This is usually at the cost of additional unknowns and a greater number of iterations is necessary for a convergence of the algorithm [51].

Publications of Abubakar et al. from 2000 and 2002 show good reconstruction results, both in numerical examples [52] and in a real measurement [53]. However, the setups used there only contained objects with simple permittivity distributions compared to a human head.

In the following section the investigations and findings of the CSI method used for stroke detection are presented. All of the findings were obtained while Micha Pfeiffer was working on his master thesis [46]. Since, close cooperation and fruitful discussions led to these results, I decided to use the pronoun “we” in this section.

7.3.1 Setup and Domains

The antenna setup is quite comparable to the one used with the Gauss-Newton-Method but with the difference that the antennas had a greater distance from the object and were arranged in a circle. Figure 7.27 gives an example setup as it was used here. The relevant domains are also noted in the figure. The data domain is limited to the circle where the antennas are located (marked with S) and the object domain comprises the whole space the square denotes (marked with D). Another similarity to the other introduced algorithms was the homogeneous background medium the object was surrounded by. Here we should keep in mind, that volume integrals are area integrals in the object domain and line integrals in the data domain.

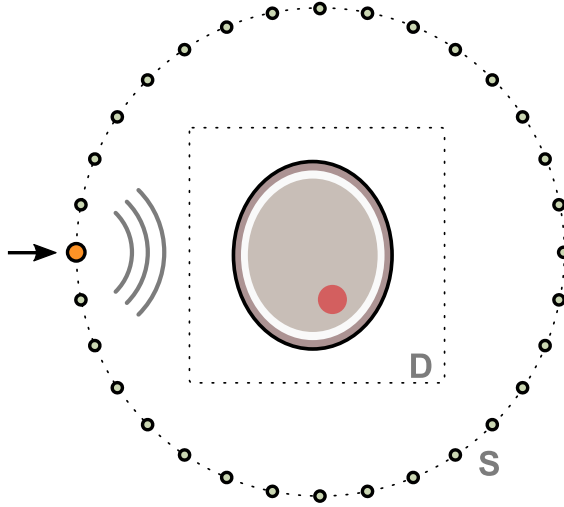


Figure 7.27: Schematic view of the setup as it was used for microwave imaging with the contrast source inversion method. The S marks the circular data domain and the D denotes the area of the squared object domain. The object here is a two-dimensional simplified head phantom.

7.3.2 The Contrast Source Inversion Algorithm

Due to the superposition principle we can write the field E_j , caused by antenna j , as a combination of the field without the object (called the incident Field) $E_{inc,j}$ and the scattered Field E_{scat} :

$$E_j(p) = E_{inc,j}(p) + E_{scat,j}(p). \quad (7.26)$$

The incident field can usually be analytically calculated, measured or determined by a numerical field simulation. The scattered field, assumed that way, can be calculated by

$$E_{scat,j}(p) = k_b^2 \int_D g(p,q) o_j(q) dv. \quad (7.27)$$

Where k_b denotes the complex wave number of the background medium, $g(p,q)$ denotes the Green's function with $r = |q - p|$ and $o_j(q)$ stands for the contrast source. For the contrast sources a contrast between the permittivity of the background medium ϵ_b and the permittivity of the still

unknown object $\varepsilon(p)$

$$\chi(p) = \frac{\varepsilon(p) - \varepsilon_b}{\varepsilon_b} \quad (7.28)$$

is calculated. These contrast sources $o_j(q)$ are a product of the contrast $\chi(p)$ and the total field of the antenna E_j :

$$o_j(p) = \chi(p) E_j(p). \quad (7.29)$$

If we keep in mind that the Green's function, as introduced in (2.17) or (2.18), only depends on the distance between the source point and another arbitrary point we can understand the equation (7.27) as a convolution integral. Hence, the contrast sources can be thought of as point sources. The scattered field is then a superposition of the fields from the contrast sources.

Within the following part we have a closer look at the total field: if the scattered field of equation (7.26) is replaced by the equation (7.27) the Lippmann-Schwinger Equation is reached:

$$E_j(p) = E_{\text{inc},j}(p) + k_b^2 \int_D g(p, q) o_j(q) dv. \quad (7.30)$$

For later definitions the following simplification was used:

$$G o_j(p) = k_b^2 \int_D g(p, q) o_j(q) dv. \quad (7.31)$$

Here G is a mathematical operator. This operator is often marked by an index. Whereupon the index is set to D if the location of the point p is in the object domain or to S if the point is in the data domain [53, 54].

7.3.2.1 The Objective Function

In contrast to the objective function known from the Gauss-Newton Method (GNM) the objective function for the CSI algorithm contains two terms

$$\frac{1}{\eta_S} \sum_j \|f_j - G_S(o_j)\|_S^2 + \frac{1}{\eta_D} \sum_j \|o_j - \chi E_{\text{inc},j} - \chi G_D o_j\|_D^2. \quad (7.32)$$

The first one of the two summands is called data equation $F_S(o)$ and is comparable to the one used for GNM. The second term is new and called object equation $F_D(o, \chi)$. Both terms will be explained in the following:

Data Equation Starting at the Lippmann-Schwinger Equation (7.30) by utilizing the G -operator and rearranging the terms results in the following equation:

$$E_j(p) - E_{\text{inc},j}(p) - Go_j(p) = 0. \quad (7.33)$$

$E_j(p) - E_{\text{inc},j}(p)$ is exactly the value which will be measured later.

If we replace $E_j(p) - E_{\text{inc},j}(p) = f(p)$ equation (7.33) can be written as

$$f_j(p) - Go_j(p) = 0. \quad (7.34)$$

As such equations usually do not hold exactly, an error term ρ is needed:

$$\rho = f_j - Go_j \quad (7.35)$$

For the so-called data equation all those errors are summed up and the following equation is reached:

$$F_S(o) = \eta_S \sum_j^N \|f_j - Go_j\|_S^2, \quad (7.36)$$

with N , the number of antennas and η_S , as a factor for normalization:

$$\eta_S = \frac{1}{\sum_j \|f_j\|_S^2}. \quad (7.37)$$

Verbalized, the data equation states that the scattered field of all contrast sources should have exactly the same value as the one obtained by measuring the fields of an empty setup, subtracted from a measurement with a setup containing an object.

Object Equation The so called object equation can also be obtained by modifying equation (7.30). For this, equation (7.30) is also rearranged and afterwards multiplied by the contrast:

$$\chi E_j(p) - \chi E_{\text{inc},j}(p) - \chi Go_j(p) = 0. \quad (7.38)$$

The first term is already known as the contrast source. Hence, we replace it and achieve

$$o_j(p) - \chi E_{\text{inc},j}(p) - \chi Go_j(p) = 0. \quad (7.39)$$

Since, such an equation does not hold exactly, an error term

$$\delta = o_j(p) - \chi E_{\text{inc},j}(p) - \chi G o_j(p) \quad (7.40)$$

is needed. At last we have to sum up the δ 's and arrive at the object equation:

$$F_D(o, \chi) = \eta_D \sum_j^N \|o_j - \chi E_{\text{inc},j} - \chi G o_j\|_D^2 \quad (7.41)$$

This formula is quite more difficult to understand. Verbalized it means that the contrast sources are the sources induced by the incident field as well as the total field. As the contrast sources contain the total field, this formulation is able to regard multiple reflections.

7.3.2.2 Regularization and Additional Constraints

To achieve optimal results it is often useful to include additional knowledge. In the publication of van den Berg et al. the total variation was used to improve imaging results. Especially if the measurement data contained noise the total variation showed great benefit [53–55]. The main hypothesis to use the total variation can be derived from natural features: Natural images are usually sparse in some domains and therefore only a few dominant coefficients are needed to represent all the information [56]. Interestingly, most of the noise an image contains is found with other coefficients. Hence, a regularization must be used that forces these other coefficients to be near to zero if noise should be reduced.

A domain where natural images are usually sparse can be reached by the calculation of the finite differences between neighboring pixels. As regularizations based on the $L1$ -norm $\|\cdot\|_1$ usually penalize non-sparse vectors, the result vectors are sparse. Hence, the $L1$ -norm of the differences is the regularization term that should be used.

Mathematically, we can write the total variation as

$$TV(\chi) = \|\nabla \chi\|_1 = \int_D |\nabla \chi(p)| dv, \quad p \in D. \quad (7.42)$$

Unfortunately, the $L1$ -norm is not continuously differentiable and therefore the total variation term is also not continuously differentiable. To overcome

that, a small value δ to smooth the kink of the absolute value $|\nabla\chi| = \sqrt{(\nabla\chi)^2 + \delta^2}$ can be added. This was also proposed by Abubakar et al.[52]. Then a derivable total variation term is obtained:

$$TV(\chi) = \int_D \sqrt{|\nabla\chi(p)|^2 + \delta^2} dv. \quad (7.43)$$

This definition still had a disadvantage: Abubakar et al. were not able to show that the problem stays convex after a modification of this kind. Their solution for this problem was to use the $L2$ -norm instead:

$$TV(\chi) = \sqrt{\int_D |\nabla\chi(p)|^2 + \delta^2} dv. \quad (7.44)$$

The regularization term defined in that way was not used as an additive term by the authors because this would require the finding of a suitable scalar value α to adjust the influence of the term

$$F = F_S(o) + F_D(o, \chi) + \alpha TV(\chi). \quad (7.45)$$

However, the term was used in a multiplicative way instead:

$$F = [F_S(o) + F_D(o, \chi)] TV(\chi). \quad (7.46)$$

Usually, a regularization is configured in such a way that its influence vanishes if the correct residuum is reached. When a multiplicative regularization is used, the regularization has to reach a value of one. Hence, the total variation term needs another modification. The modification was to normalize the term with the derivative from the previous step

$$TV(\chi) = \frac{\int_D |\nabla\chi(p)|^2 + \delta_n^2 dv}{\int_D |\nabla\chi_n(p)|^2 + \delta_n^2 dv}. \quad (7.47)$$

As the changes within the contrast would get very small near the residuum this term does indeed vanish if a minimum is reached. The square root was neglected to simplify the gradient of this term. But there still was an unwanted behavior: The $L2$ -norm, as used here, would penalize large values more than smaller ones and the sparsity would be lost. Hence, the term as written here would smooth out the sharp edges, which are

usually wanted in the images. The solution is: if the integral is taken out of the fraction

$$TV(\chi) = \frac{1}{V} \int_D \frac{|\nabla\chi(p)|^2 + \delta_n^2}{|\nabla\chi_n(p)|^2 + \delta_n^2} dv \quad (7.48)$$

the weighting is no longer global, but becomes a local one. Each point derivative is weighted with the prior derivative at the same point. Hence, even a large step will deliver a small value near the residuum. V denotes the volume of the object domain.

The value δ_n is still undefined and was set to

$$\delta_n^2 = F_{D,n-1} \frac{1}{dv_D}, \quad (7.49)$$

where dv_D is the size of a volume element of the discretized object domain and $F_{D,n-1}$ is the value of the object equation of the previous iteration step. The multiplicative regularized contrast source inversion (MR-CSI) as described here was originally introduced by van den Berg, Abubakar et al. [53–55].

Natural Limits The permittivity of the material that should be imaged does have natural limits. The complex relative permittivity would neither have a positive imaginary part nor a real part smaller than one. Hence, we calculated a minimal contrast

$$\chi_{min} = \frac{\epsilon_{min} - \epsilon_b}{\epsilon_b} \quad (7.50)$$

with a minimal complex permittivity

$$\epsilon_{min} = \epsilon_0 \left(1 - i \frac{0}{\omega\epsilon_0} \right) = \epsilon_0 + 0i. \quad (7.51)$$

This minimal contrast was afterwards enforced with each iteration. A comparable idea was used by van den Berg et al. [54].

7.3.2.3 The Update Procedures

By observing the full objective function

$$F(\chi, o) = [F_S(o) + F_D(o, \chi)] F_R(\chi) \quad (7.52)$$

$$= \left(\eta_S \sum_j \|f_j - G_S o_j\|_S + \eta_D \sum_j \|\chi E_{\text{inc}} - o_j + \chi G_D o_j\|_D \right) F_R(\chi) \quad (7.53)$$

with

$$F_R(\chi) = \frac{1}{V} \int_{\mathbb{D}} \frac{|\nabla \chi(p)|^2 + \delta_n^2}{|\nabla \chi_n(p)|^2 + \delta_n^2} dv, \quad (7.54)$$

which is used by the algorithm, it is obvious that an update formula is quite complicated. This was also the idea which the original authors of the algorithm had. Hence, they introduced another simplification: As the algorithm needs an update for the contrast and the contrast sources, respectively, they intended to split the update [55]. In a first step only the contrast sources o were updated and the contrast χ was hold fix. In a second step the problem was reversed and the contrast source o was fixed where an update for the contrast χ was made.

Updating the Contrast Sources To update the contrast sources a CG-method was used. The update formula

$$o_{j,n} = o_{j,n-1} + \alpha_n^o v_{j,n} \quad (7.55)$$

looks quite similar to the one known from the GNM where $v_{j,n}$ is the update direction and α is the step size. However, the way to obtain the direction is different. The direction was calculated by the so-called Polak-Ribière conjugate gradient direction:

$$v_{j,n} = \begin{cases} g_{j,n}, & n = 0 \\ g_{j,n} + \frac{\sum_k \langle g_{k,n}, g_{k,n} - g_{k,n-1} \rangle_D}{\sum_k \langle g_{k,n-1}, g_{k,n-1} \rangle_D} v_{j,n-1}, & n > 0 \end{cases} \quad (7.56)$$

with the gradient

$$g_{j,n} = -\eta_S G_S^* \rho_{j,n-1} - \eta_D [r_{j,n-1} - G_D^* (\overline{\chi_{n-1}} r_{j,n-1})]. \quad (7.57)$$

Here G_S^* and G_D^* are the adjoint operators of G_S and G_D respectively (more in Appendix B) and $\langle \cdot, \cdot \rangle_D := \int_D \dots dv$ denotes the dot product on the domain D. The step size α was determined by a line search along the direction $v_{j,n}$:

$$\alpha_n^o = \arg \min [F_S(o_{n-1} + \alpha^o v_n) + F_D(o_{n-1} + \alpha^o v_n, \chi_{n-1})] \quad (7.58)$$

Multiple complex results and one real valued result are possible with that equation but the real valued one is the one wanted. The correct result is delivered by the following equation:

$$\alpha_n^o = \frac{\text{real}(\sum_j \langle g_{j,n}, v_{j,n} \rangle_D)}{\eta_S \sum_j \|G_S v_{j,n}\|_S^2 + \eta_D \sum_j \|v_{j,n} - \chi_{n-1} G_D v_{j,n}\|_D^2}. \quad (7.59)$$

Updating the Contrast on CSI The problem to be solved here is more simple than the update of the contrast sources. The objective function for this part of the problem is

$$\min_{\chi} F_D(o_n, \chi). \quad (7.60)$$

This problem does have an analytic solution

$$\chi_n = \frac{\sum_j o_{j,n} \overline{E_{j,n}}}{\sum_j |E_{j,n}|^2}. \quad (7.61)$$

This is possible due to the fact that the data equation F_S does not directly depend on χ . The therefore needed field $E_{j,n}$ is calculated by the Lippman-Schwinger equation (7.30).

Updating the Contrast on MR-CSI If the multiplicative regularization term is used, the updating of the contrast for the objective function is not as easy as it is without it.

Due to the dependency of the regularization term F_R on χ , the data equation cannot be neglected and the update enforces the consideration of the whole objective function

$$\min_{\chi} [F_S(o_{j,n}) + F_D(o_{j,n}, \chi)] F_R(\chi). \quad (7.62)$$

As here the CG method was also used the gradient of the objective function

$$g_{R,n} = \frac{\partial[(F_{S,n} + F_{D,n})F_{R,n}]}{\partial\chi} \quad (7.63)$$

is needed for the update. It can be noted that the arguments for the functions were omitted to improve the readability. By applying the product rule we achieve

$$g_{R,n} = \frac{\partial(F_{S,n} + F_{D,n})}{\partial\chi} F_{R,n} + (F_{S,n} + F_{D,n}) \frac{\partial F_{R,n}}{\partial\chi} \quad (7.64)$$

and if the independence of $F_{S,n}$ from χ is regarded, we achieve

$$g_{R,n} = \frac{\partial F_{D,n}}{\partial\chi} F_{R,n} + (F_{S,n} + F_{D,n}) \frac{\partial F_{R,n}}{\partial\chi}. \quad (7.65)$$

At this point we can use the formulations used before, introduced to only update the contrast on CSI. By using equation (7.61) a new contrast χ_n minimizing (7.60) can be obtained. Hence, the partial derivative $\frac{\partial F_{D,n}}{\partial\chi}$ will be zero at this point [55] and thus, the gradient simplifies to

$$g_{R,n} = (F_{S,n} + F_{D,n}) \frac{\partial F_{R,n}}{\partial\chi}. \quad (7.66)$$

The partial derivative of the regularization term needed now is

$$\frac{\partial F_R(\chi)}{\partial\chi}(p) = \frac{1}{V} \nabla \cdot \left[\frac{\nabla\chi(p)}{|\nabla\chi_n(p)|^2 + \delta_n^2} \right], \quad (7.67)$$

where $\nabla\chi := \left[\frac{\partial\chi}{\partial x}, \frac{\partial\chi}{\partial y} \right]$ denotes the spatial gradient. More details about the computation of the partial derivative of the $F_R(\chi)$ can be found in the appendix C.

Here it should be noted that the numerator is now due to the spatial derivative a vector and because of this the ∇ -operator in front of the brackets stands for the divergence operator. By having the gradient we can now calculate an update direction by using the CG method:

$$v_{R,n} = \begin{cases} g_{R,n}, & n = 0 \\ g_{R,n} + \frac{\langle g_{R,n}, g_{R,n} - g_{R,n-1} \rangle_D}{\langle g_{R,n-1}, g_{R,n-1} \rangle_D} v_{R,n-1}, & n > 0 \end{cases} \quad (7.68)$$

As a last step a line search is needed to determine a sufficient step size β_R for the updated equation

$$\chi_{R,n} = \chi_n + \beta_R v_{R,n}. \quad (7.69)$$

As published by van den Berg et al. a suitable value for β_R can be calculated analytically [55]. Unfortunately, our test showed that the analytic solution for β_R contains large exponents and involves large numbers, causing the solution process to be numerically unstable. To overcome that we decided to use a numeric minimization procedure as provided by MATLAB. Our implementation of the line search involved the function `fminbnd` which is based on a golden section search. This showed similar results for the numerically calculated step size if compared to the analytic solution.

7.3.2.4 Starting with an Initial Guess

The convergence of the algorithm depends beside other facts also on proper initial values for the contrast sources o_j and the contrast χ [54]. A good initial guess for the contrast source can be achieved by

$$o_{j,0} = \frac{\|G_S^* f_j\|_D^2}{\|G_S G_S^* f_j\|_S^2} G_S^* f_j. \quad (7.70)$$

where the term $G_S^* f_j$ can be understood as a back propagation of the measurement to the object domain. The rest of the expression is a scalar weighting in order to achieve results independent from the measured amplitude. With initial contrast sources achieved that way, an initial contrast is calculated:

$$\chi_0 = \frac{\sum_j o_{j,0} \bar{E}_{j,0}}{\sum_j |E_{j,0}|^2}. \quad (7.71)$$

The overall initial field $E_{j,0}$ is calculated, as introduced before, by using the Lippmann-Schwinger equation (7.30).

7.3.3 Test Data from Forward Calculations

Due to the two-dimensional test setup used, an also two-dimensional forward calculation was desirable. Thus, the already existing simulation

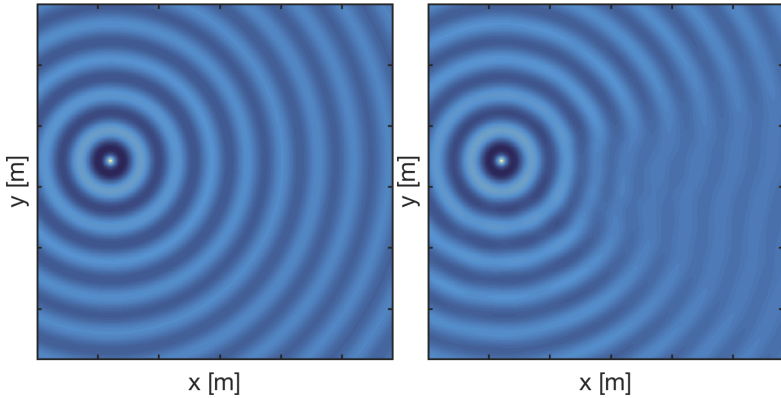


Figure 7.28: The field obtained by the implemented FDTD-Meep-Solver. The images show the field obtained by the subsimulation of antenna 24. The left image shows the real part of the incident field (i.e. $E_{\text{inc},24}$) and the right image shows the field after having added an object, E_{24} . The background medium used here was air. Thus, the attenuation within the background medium was almost zero. It can be noted that only the field values measured at the antennas were used for the reconstruction but not the entire field distributions which are shown here. For the reconstruction the incident field was approximated using an analytic function and the field with the object was considered to be unknown (because it would be unknown when it comes to real measurements).

tools utilizing the Meep-solvers, which were implemented for the Gauss-Newton Algorithm (compare section 7.2.2) were reused. The benefit of using Meep was the fact that Meep provides point sources which was not the case for the more advanced simulation environments CST and SEMCAD. For CST and SEMCAD antennas were necessary for a field excitation. However, with the inclusion of antennas other effects also have to be regarded, like coupling between antennas and a non-omnidirectional radiation pattern.

Similar to the simulations made for the Gauss-Newton method an empty simulation and a simulation containing the object of interest was needed. The empty simulation was not really empty, but the whole space was filled with the permittivity of the background medium.

Even the simulation procedure was equal to the one I did for the Gauss-Newton method. N subsimulations were performed with only one source

switched on in each case. A simulated example (subsimulation 24) can be observed in Figure 7.28.

7.3.3.1 Sub-Voxel Permittivity Values and Interpolation

As indicated before (section 7.2.2), Meep uses a spatial resolution for the simulations, which was independent of the voxel grid where the permittivity values were stored. Moreover, Meep uses the common known Yee's lattice for the spatial discretization of the simulated space. Due to the shift of a half voxel size between the electric and the magnetic field as defined by Yee's lattice, values of the permittivity for half and full voxels are required. During the first implementation of the class holding the object, this was regarded by just rounding the input point to the next full voxel. Since this shifted the model and thus influenced the results of the CSI a bi-linear interpolation for the permittivity was introduced. A similar interpolation is used inside the Meep framework for the freely positionable sources and the function to acquire the field which also supports freely defined positions.

7.3.4 Calibration

As already mentioned for the CSI algorithm the basis of the field calculation is a superposition of the fields from multiple point sources at the CSI algorithm. All point sources are the result of a convolution (the G-Operator) between a fundamental solution (Green's function) and the overall permittivity distribution. Since this formulation was also used to propagate errors from the data domain through the object domain and vice versa the algorithm works at its best when the incident fields are also analytically approximated.

Due to the ability of the Meep framework to simulate near ideal point sources it should be assumed that a calibration is not necessary. Unfortunately, this is not exactly true, as a closer look showed a phase shift between the fields propagating along the main diagonals and the ones propagating along the axis direction (compare Figure 7.29).

However, the discovered phase shift reduced the quality of the reconstructions. Fortunately, this can be compensated by a correction factor

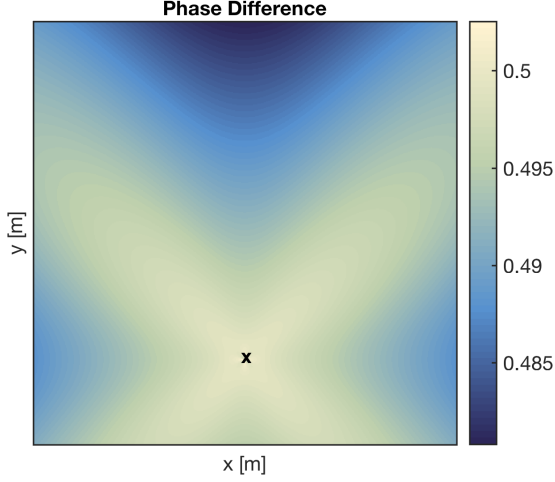


Figure 7.29: If the analytically calculated field of a point source (equation (2.18)) is compared to the field obtained by a simulation with the FDTD-Solver of Meep a phase difference between the axis direction and a diagonal propagation could be observed. The reason for this is seen in the discretization of quadratic voxels and indeed the effect is reduced in higher spatial resolutions. The difference is noted in [rad].

defined by

$$K_{j,l} = \frac{E_{inc,j}^{an}(p_l)}{E_{inc,j}^{sim}(p_l)}, \quad (7.72)$$

where $E_{inc,j}^{an}(p_l)$ denotes an analytic field and $E_{inc,j}^{sim}(p_l)$ the simulated field at the receiver position p_l . The correction is then done by

$$f_{j,l}^{cal} = K_{j,l} f_{j,l} \quad (7.73)$$

$$= K_{j,l} [E_j(p_l) - E_{inc,j}^{sim}(p_l)] \quad (7.74)$$

$$= K_{j,l} E_j(p_l) - E_{inc,j}^{an}(p_l) \quad (7.75)$$

where $f_{j,l}^{cal}$ denotes the calibrated input values. By the way this calibration procedure could also be used to calibrate real measured input data.

Usually, a network analyzer is used to measure and hence, the input data are not fields but S-parameters. Fortunately, the conversion can be done by the same procedure as Ostadrahimi et al. showed 2011[57]. Therefore the simulated field $E_{inc,j}^{sim}(p_l)$ is replaced by the corresponding scattering

parameter $S_{l,j}$. Thus, the equation (7.72) is written by

$$K_{j,l} = \frac{E_{inc,j}^{an}(p_l)}{S_{j,l}}. \quad (7.76)$$

As an alternative to the calibration the incident fields taken from the simulation could be used which we had done before the discovery of the phase shift.

7.3.5 Three Test Objects

In total the algorithm was tested on three objects, sometimes called models. Here the objects were distributions of complex permittivity, including the background medium and the discretization of the S and D domains. If it is not stated differently the data domain always contained 32 antennas.

7.3.5.1 Concentric Squares

The first of the models (the concentric squares model) was defined to be dependent on the frequency used for reconstruction and the background medium. Therefore the spatial shaping was defined to be of the size $2\lambda \times 2\lambda$ with a step inside to a smaller square of $\lambda \times \lambda$. The dimension of the object domain with a size of $3\lambda \times 3\lambda$ was also defined in that way. The contrast of the inner square was selected to be $\chi_1 = 0.3 + i0.4$, the outermost square had a contrast of $\chi_2 = 0.6 + i0.2$ and the background contrast was zero. A picture of the model is given in Figure 7.30. The radius of the data domain was selected to be 3λ . The frequency with which the model was defined was selected to be 0.5 GHz and the background medium had the permittivity and conductivity of air ($\epsilon_r = 1$ and $\sigma = 3 \times 10^{-15} \text{ S/m}$). Due to the relative definition of the squares the morphology of the model depended on the selected background medium. As an example for this Figure 7.31 shows an image of the model having air as its background in the upper row and in the lower row of the image matching liquid ($\epsilon_r = 50$ and $\sigma = 0.8 \text{ S/m}$) was selected.

The model, as defined here, was also used by the original authors of this algorithm [54, 55]. This was the reason why we needed it to compare

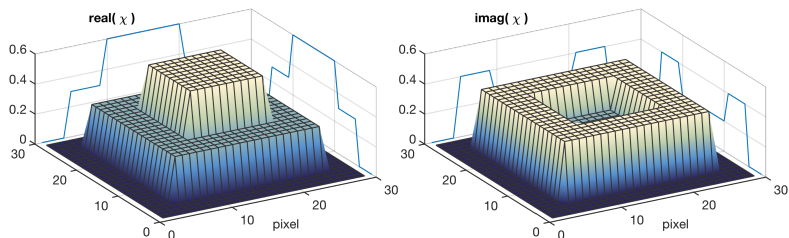


Figure 7.30: The concentric squares object defined at a frequency of 0.5 GHz as introduced by Abubakar and van den Berg [54]. The contrast is shown of the $3\lambda \times 3\lambda$ object domain, with real part (left) and imaginary part (right). The domain was discretized into 29×29 voxels.

the performance of the implementation. One thing should be noted here: we did not redesign the model, when switching the frequency. This means that the reconstruction of greatly differing frequencies would look different, too. This is not only related to the differing dimension in relation to the wave length of the object, but it is also related to the frequency dependence of the imaginary part.

7.3.5.2 A Simplified Head Model

After the tests with the first abstract test object a second object more closely linked to reality was introduced. Realistic dimension and realistic permittivities were therefore defined for the model.

Table 7.3: Permittivities used for the simple head phantom. The values were taken from [22] at 1.0 GHz . The same permittivity values were also used when the model was simulated and reconstructed in other frequencies (i.e. the frequency-dependency of the relative permittivity and conductivity was ignored). By ignoring the frequency-dependency the reconstructions of differing frequencies were easier to compare.

| Material | Rel. Permittivity ϵ_r | Conductivity σ (S/m) |
|----------|--------------------------------|-----------------------------|
| Skin | 40.9 | 0.9 |
| Bone | 20.6 | 0.364 |
| Brain | 48.9 | 1.31 |
| Blood | 61.1 | 1.58 |

As we intended to use a frequency of 1 GHz for the simulation (a frequency selected by regarding the frequency range of the antennas and

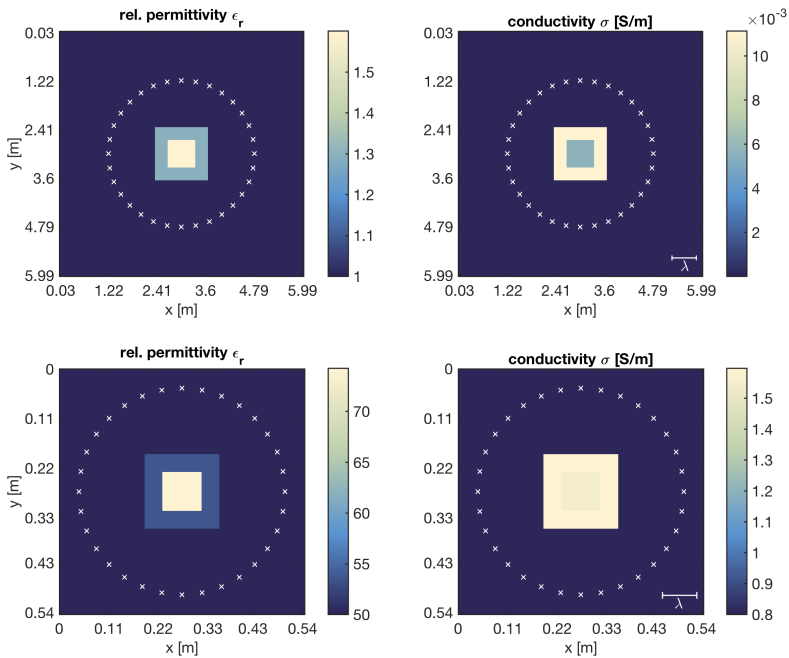


Figure 7.31: The concentric squares model with a background material of air is visible in the upper row and with a background material of matching liquid in the lower row. Due to the different background media the wavelength (shown in the bottom right corner of the conductivity images) varies greatly. Since this model is defined to have an object domain of 3λ by 3λ the size of the whole model also changes drastically with the change in background medium. The crosses mark the antenna positions.

previous studies) we also selected the permittivity of the materials for this frequency (Table 7.3). The basic shape, similar to that of the other phantoms, was circled with an outermost diameter of 20 cm . It included a skin layer of 1 cm thickness and a bone layer of also 1 cm thickness. The inside was filled with general brain tissues. The model contained a hemorrhage, a small non-centered circle of diameter 4 cm , filled with a material having a blood-like permittivity.

Due to the simplicity of the model it is ideal to study effects, inherent to the algorithm, as for example the influence of the huge contrast at the

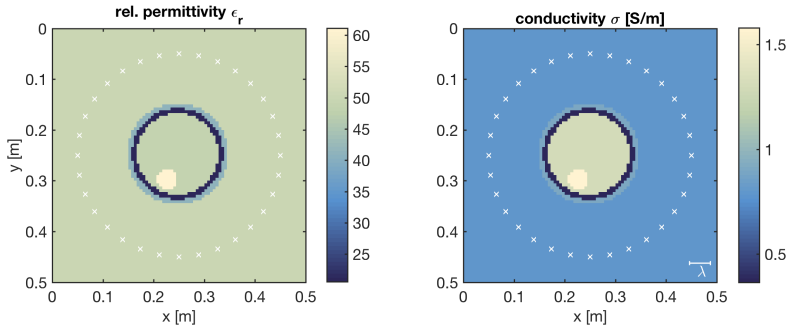


Figure 7.32: A simplified head phantom model containing skin, skull and brain, the relative permittivity (left) and the conductivity (right) are shown. The small non-centered circle was used to simulate a hemorrhage and the small bar in the lower right corner shows the wavelength at 1.0GHz in matching liquid.

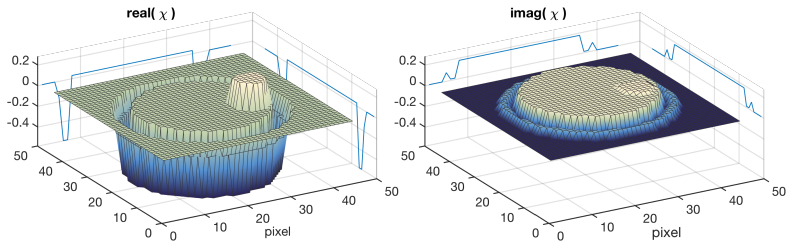


Figure 7.33: Contrast of the simple head phantom model at 1.0GHz with matching liquid as background material. The outermost layer represents the skin. Its permittivity is close to that one of the matching liquid and hence, the contrast is small (around $0.1 + 0.1i$). The next layer is representing the skull. There a very large jump in the real part of the contrast is generated. In this setup the bleeding area is hardly visible in the image of the imaginary part of the contrast but it leaves a high value in the real part.

skin-skull-brain interface. To study those effects the model was simulated and reconstructed with various background materials. The most notable ones were air and matching liquid. Figure 7.33 contains the contrast of the object domain and Figure 7.32 offers a full view of the model. In both cases matching liquid was used as background material.

7.3.5.3 Realistic Head Model

In the end the algorithm should also work sufficiently in realistic conditions. Hence, we introduced a realistic object. The setup for it was similar to the

one containing the simplified head, except from the head phantom. The head phantom used was constructed from MRI data by Michel et al. [58]. They used T_1 -weighted MRI scans to reconstruct permittivity maps of the brain. To do so a water-content map was derived from the T_1 – *image* and afterwards used to calculate a permittivity map. The premise to do so was that they assumed that the water content is a good indicator for the measurable permittivity at the utilized frequency range. As the procedure did not include segmentation or comparable steps all the details of the inside head could be maintained. Due to this a very realistic view of the head could be utilized for our model. It included cerebrospinal fluid and very fine structures lying between grey and white matter. Even the liquid filled ventricles were observable. A view of the setup can be seen in Figure 7.34 and a view of the object domain and its contrast in Figure 7.35. This time the object domain was visualized from above. This was done due to the fact that the high steps in contrast were leading to 3D-surface-views which were not easily interpretable.

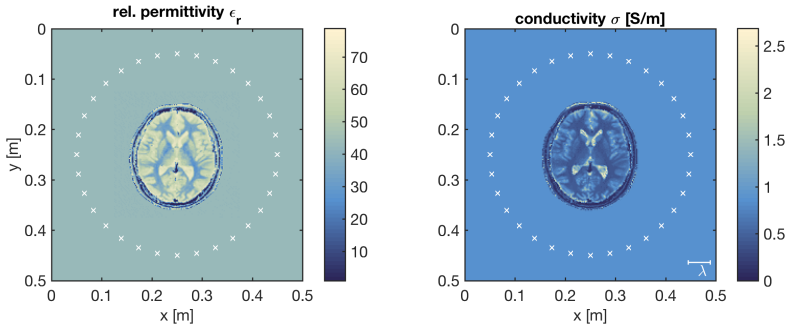


Figure 7.34: The object derived from MRI within the setup. For the simulation and reconstruction 1 GHz was used and a background material consisting of matching liquid.

Finally, a setup including a simulated hemorrhagic stroke was introduced. This was done to examine the ability of this algorithm to diagnose intracerebral bleeding. Figure 7.36 shows the contrast of the object domain of this setup. This was similar to the stroke region of the simplified phan-

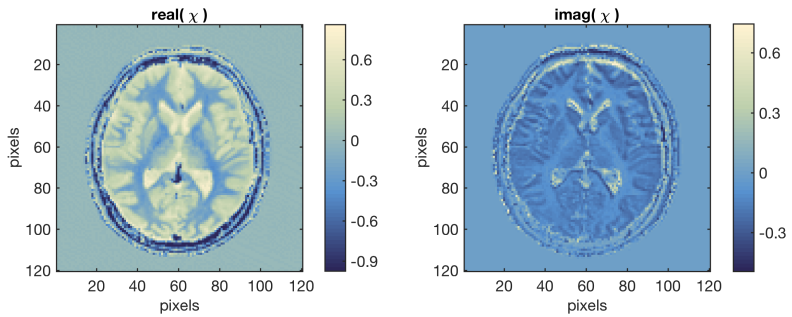


Figure 7.35: The contrast view of the object domain. Shown is the advanced head phantom at 1 GHz . The range of the contrast is significantly higher than the one of other models.

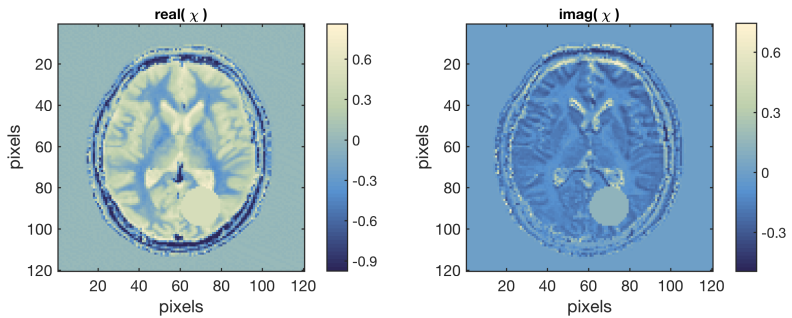


Figure 7.36: Modified model with a simulated hemorrhage having a diameter of 4 cm . The permittivity at the location of the hemorrhage was replaced by the permittivity of pure blood.

tom. It contained a circular region of 2 cm radius having a permittivity of blood.

7.3.6 Frequency Hopping

Since the spatial resolution is among other things depending on the utilized frequency the details of the head are smoothed out. This is a way how a reconstruction using higher frequencies could add important information. Unfortunately, the probability of converging into a wrong minimum grows with higher frequencies. Due to that fact a convergence in high frequencies depends on an initial guess, close to the correct minimum.

Starting from blank space such a sufficient initial guess could be reached by previous reconstructions with lower frequencies. Such a procedure was also introduced by van den Berg and Abubakar [54]. They described a stepwise increase of the frequency after every reconstruction. As both the contrast and the contrast sources are strongly depended on the frequency they cannot be used as yielded by the algorithm, instead the values must be transformed.

7.3.6.1 Transform the Contrast for a New Frequency

The easiest way to transform the contrast would be achieved by first calculating the relative permittivity and the conductivity of the model and then calculating the new contrast of those values. To achieve the complex permittivity from the current contrast the rearranged equation (7.28)

$$\varepsilon_{f_0} = \chi_{f_0} \varepsilon_b + \varepsilon_b \quad (7.77)$$

can be used. The relative permittivity is then

$$\varepsilon_r = \frac{\operatorname{Re}\{\varepsilon_{f_0}\}}{\varepsilon_0} \quad (7.78)$$

and the conductivity

$$\sigma = -\operatorname{imag}(\varepsilon_{f_0}) \omega_{f_0}, \quad (7.79)$$

where f_0 denotes the current frequency. After updating the background permittivity the new contrast for f_1 can be calculated by

$$\chi_{f_1} = \frac{\varepsilon_{f_0} - \varepsilon_b}{\varepsilon_b} = \frac{\varepsilon_0 \left(\varepsilon_r - i \frac{\sigma}{\omega_{f_0} \varepsilon_0} \right) - \varepsilon_b}{\varepsilon_b}. \quad (7.80)$$

Here it should be noted that almost all biological materials are dispersive and due to this they have a frequency-dependent relative permittivity and conductivity. With sufficiently small frequency steps this feature can be neglected as the algorithm is able to compensate these small errors.

7.3.6.2 A Transformation for the Contrast Sources?

Unfortunately, the contrast sources are not as easy to transform as the contrast itself. By observing equation (7.29), their dependence on the electric field is observable. Due to the fact that it contains all the reflections and refraction it is strongly nonlinear concerning frequency changes. Hence, there cannot be a transformation as easy as the one for the contrast.

Some examinations on this topic showed that using the new incident field $E_{\text{inc},f_1,j}$ and the old contrast χ_{f_0} to generate new contrast sources

$$o_{j,f_1} = \chi_{f_0} E_{\text{inc},f_1,j} \quad (7.81)$$

was not a sufficient initial guess. If this was used as initial guess the algorithm was not converging into the correct minimum. As an alternative we then used the reconstructed contrast within a simulation to generate the new field. By doing so the correct minimum could be found (compare 7.3.8.5).

7.3.7 A Few Details of the Implementation

As indicated before we used MATLAB to implement the algorithm. Due to the wide variety of tools to image and review results it is a good platform to develop and debug such algorithms. We often described the G and G^* operations as convolutions. This fact was used to improve the performance and hence, the operator was carried out in the frequency domain. The convolution can be calculated by a simple multiplication. Due to the fact that the Green's function was independent from all iterations it could be calculated and cached before the algorithm was started. Finally, the ability to perform parallel calculation of MATLAB was used to increase the performance in a further way.

7.3.8 Reconstruction Results of the Contrast Source Inversion Algorithm

All three test objects were used in various setups. The simulations were made with the FDTD-Meep-Solver and the reconstructions either with the CSI method or with the MR-CSI method.

7.3.8.1 Reconstruction Results of the Concentric Squares

The spatial dimensions of the model were designed for a frequency of 0.5 GHz . The dimensions were hold fix even if the frequency was changed. Hence, the model with air as its background material was constructed with a λ of approximately 60 cm and the model with the matching liquid with $\lambda \approx 6.7\text{ cm}$. The permittivity distribution of the object was determined by the predefined contrasts and the permittivity of the background medium.

Reconstructions in Air When air was used as background medium both algorithms (CSI and MR-CSI) were able to deliver good results. The simulated measurements for this case can be observed in Figure 7.37.

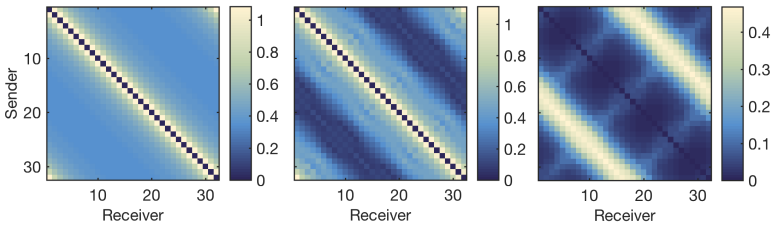


Figure 7.37: Results of the simulations with air as background medium and at a frequency of 0.5 GHz . The left image illustrates the results of the reference simulation without an object and the center image illustrates the results of the simulation with the concentric squares. The right image shows the input data f (the difference between the right and the center image). Each row contains the measurement of a subsimulation, whereas the values on the main diagonal would contain the measurement at the source point. As this point was neglected the value is zero.

Each row of the image contains the measurement of a single subsimulation where the value for the source (main diagonal) was set to zero. The left

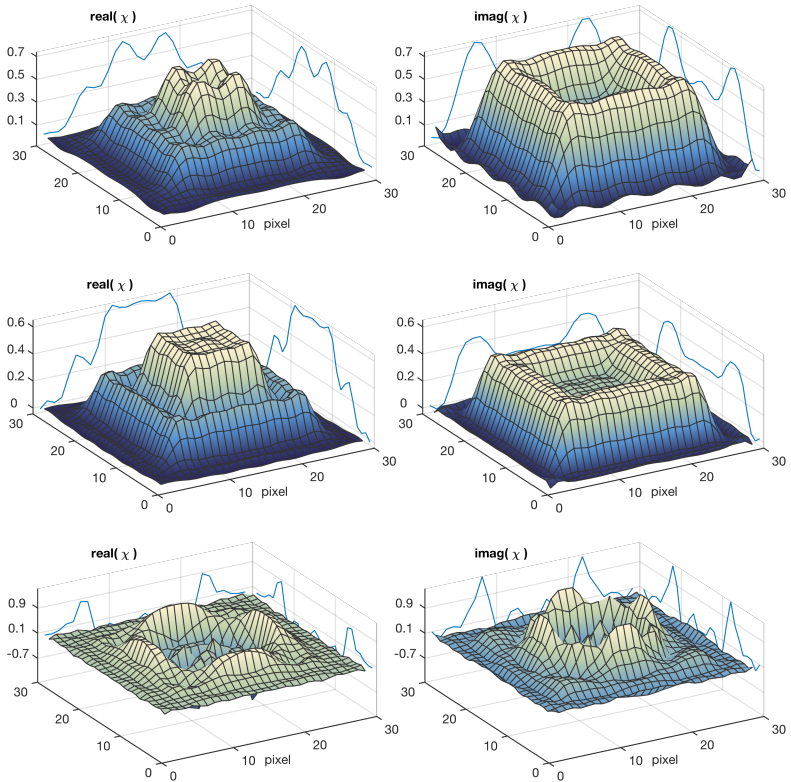


Figure 7.38: Reconstruction results of the concentric squares model with air as its background material. As described before the model was designed for a frequency of 0.5 GHz . It shows the results achieved the MR-CSI algorithm. On the left the real part of the contrast and on the right the imaginary part. Three different frequencies were tested, 0.3 GHz (top row), 0.5 GHz (the central row) and at 0.7 GHz (the lowermost row). For these reconstructions 1024 iterations were carried out.

image shows the measured fields for the empty setup, the centered image contains the measurements achieved by the setup containing the concentric squares and the right image shows the input data f (the difference between the left and the center image).

By looking at the input data (right image) high values on the minor diagonals can be observed. These diagonals contain the transmitted signals.

Because of those it can be observed that the main information for the reconstructions comes from the antennas opposite of the source.

Three different frequencies were tested. The results achieved by the frequency, which was also used to design the model, were by far the best ones and the results for the lower frequency were simply smoothed out. Conspicuously, the results of the higher frequency are quite bad. We assumed that the reason for this was the fact that the algorithm was converging to a wrong minimum. If our results are compared with the results published by van den Berg and Abubakar [54] it can be noted that their results look slightly better. Especially the contours are more sharp. The result seems to be almost equal to the input model. We assume that the reason for this is that our simulations were made on a Yee's lattice with interpolated permittivities which led to an input profile with smoothed edges.

Concentric Squares in Matching Liquid As mentioned before matching liquid is usually used to improve the coupling between antennas and the object of interest so that the energy transmitted though the object is at its best. Due to the way the permittivity was defined (over the contrast)

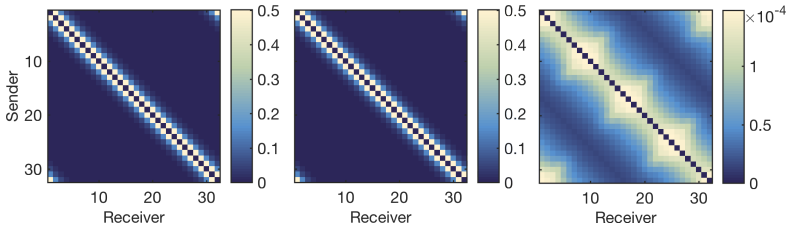


Figure 7.39: Simulated input data form the concentric squares with matching liquid as its background material. In the left the results of the reference simulation without an object. The center image is the result of the same setup with the difference that an object was present and the right image contains the input data, which is the difference between the left and the center image. It can be observed that here the minor diagonal no longer contains the main information. Now the main diagonal is stronger. Hence, the reflection became more important for the reconstruction.

a better match was not achievable. Our intention concerning the test case

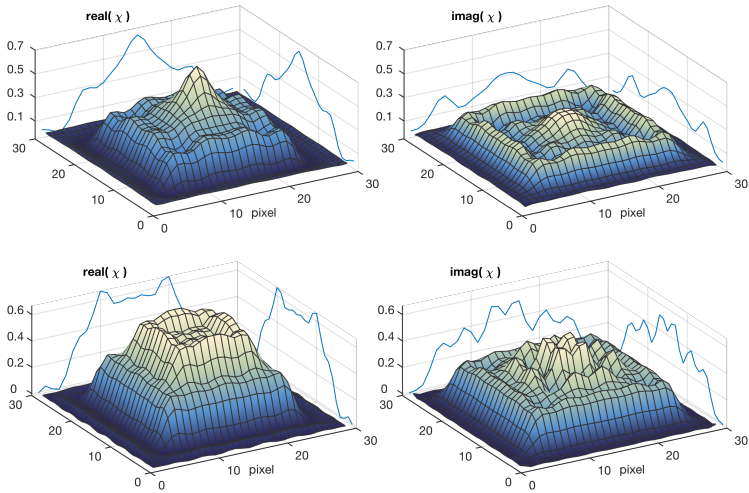


Figure 7.40: CSI reconstruction of the concentric squares model with matching liquid as its background medium at a frequency of 0.5 GHz . The top row shows the 512th iteration and the results imaged at the lowermost row are achieved after 10000 iterations.

was to see if the algorithm could handle a medium with a significantly higher conductivity. In addition to the high conductivity in the background medium the conductivity within the object was also increased. Hence, the attenuation over the object domain was larger and grew from formerly 8 dB with air up to 30 dB with the matching liquid. This was also observable with the results from simulation (Figure 7.39).

The differences between the left and central image cannot be perceived by the human eye. Another significant change was perceivable on the input data (the right image) the highest values are now no longer on the minor diagonal. That means that the main information is now provided by reflections and no longer by the transmissions, as it was the case for the setup with air as its background medium.

One result of all this was that the contours were reconstructed first and comparably fast. But to achieve results for the inside of the object a lot more iterations were required. Good points to observe this effect were iteration 512 and iteration 10,000 (compare Figure 7.40).

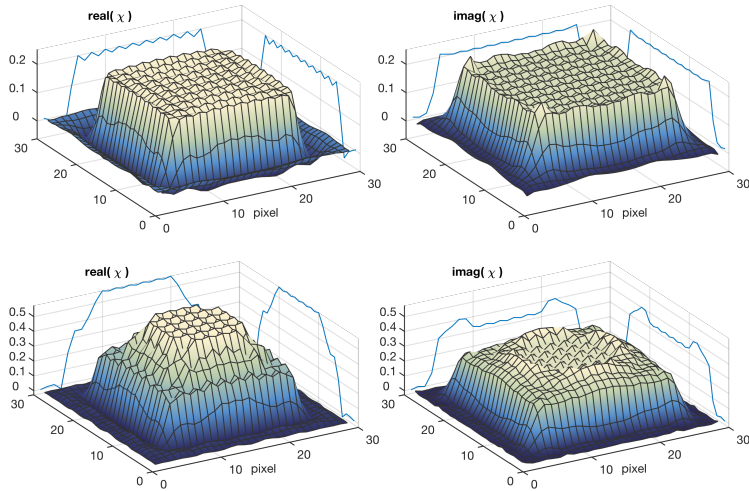


Figure 7.41: MR-CSI Reconstruction of the concentric squares model with matching liquid as its background medium at a frequency of 0.5 GHz . The result after 512 is visible in the top row and the result after 10000 iterations in the lowermost row. The final result is remarkably close to the original object.

A significant improvement was achieved with a switched-on multiplicative regularization. The results of the MR-CSI algorithm are observable in Figure 7.41. The MR-CSI method was effectively flattening the reconstructed object. This was especially the case with the first thousand iterations. With a growing number of iteration and decreasing errors this effect became less effective and the original profile was sufficiently reconstructed. However, a strange effect remained with the results of the MR-CSI, namely a rippled pattern in the middle of the objects. Unfortunately, we were not able to identify the origin of this ripple till now.

7.3.8.2 Reconstructing the Simple Head Phantom

For the reconstruction of the simplified head phantom multiple frequencies were tested, too. As examples, the results of the setup for 0.5 GHz (Figure 7.42) and 0.7 GHz (at Figure 7.43) are presented here. Due to the naturally high conductivity inside biological tissues and the also high conducting

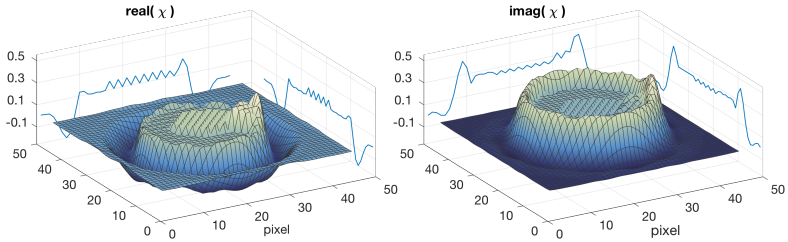


Figure 7.42: Resulting reconstruction of the setup for 0.5 GHz when using MR-CSI after 10000 iterations. The simulated bleeding is clearly observable, even if the reconstructed permittivities are not perfectly matching. This was especially the case inside the skull. The ripple pattern with unclear origin, which is known from the test before, is observable, too.

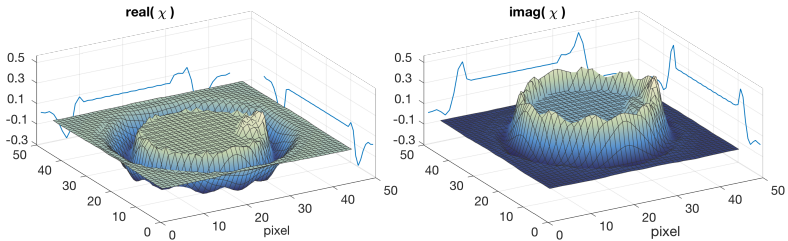


Figure 7.43: Reconstruction of the setup containing the simplified head phantom after 10000 iterations. The selected frequency was 0.7 GHz . Similar to the reconstruction at 0.5 GHz the bleeding is clearly observable. Here the unclear ripple pattern is not as strong as it was for the lower frequency, but it is still visible.

matching liquid similar effects were observable in this reconstruction, as could be observed for the concentric squares with high conductivity. The reconstruction was started at the outermost contours of the object and the inner structures were not visible for a long time. Only after a minimum of 5000 iterations a vague impression of the inside became apparent.

An interesting, but not very surprising, observation of these results is related to the deep fold the skull was causing in the contrast image (Figure 7.33). The algorithm was not able to reconstruct this feature correctly. The small thickness of the skull (about a quarter wave length) was probably outside the available spatial resolution. It is of interest that the algorithm compensated the error caused by the missing skull by adding a high conducting area to the inside of the head, adjacent to the

imperfect skull (visible in both Figures 7.42 and 7.43). To verify that this

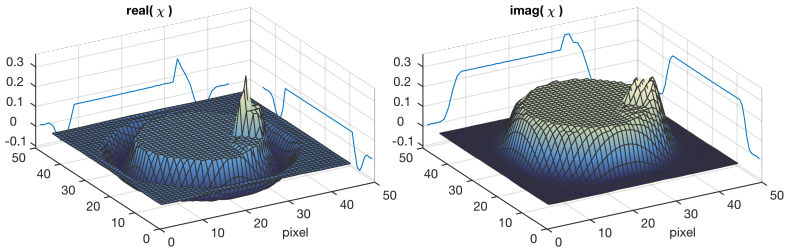


Figure 7.44: The reconstructed phantom after the replacement of the permittivity of the skull by the permittivity of the skin. As expected the ring of high permittivity in the imaginary part of the contrast was vanished.

is indeed an error caused by the skull the same setup was simulated and reconstructed again but this time the permittivity of the skull was replaced by the permittivity of the skin. The results indeed showed the expected effect (Figure 7.44). The imaginary part did not show the high conducting area. This is an error we could not avoid and an error that would probably occur in all reconstructions containing a head or a head-like phantom.

7.3.8.3 Results with the Realistic Head Phantom

The last of the three test objects (the realistic head phantom) was reconstructed and simulated for multiple frequencies, similar to the simplified phantom. Surprisingly, the total variation term was not of benefit here. The regularization flattened the inner head up to unrecognizable conditions. This was probably caused by a too strong influence of the regularization term. Hence, the regularization was disabled for these reconstructions. The result of a reconstruction without the regularization can be observed in Figure 7.45. The skull was not correctly reconstructed. But here the positive slope of the imaginary part is not easily separable from the anyway existing positive slopes caused by the cerebrospinal fluid. Anyhow, some of the inner structures are well identifiable, such as for example the ventricular system filled with high conducting cerebrospinal fluid.

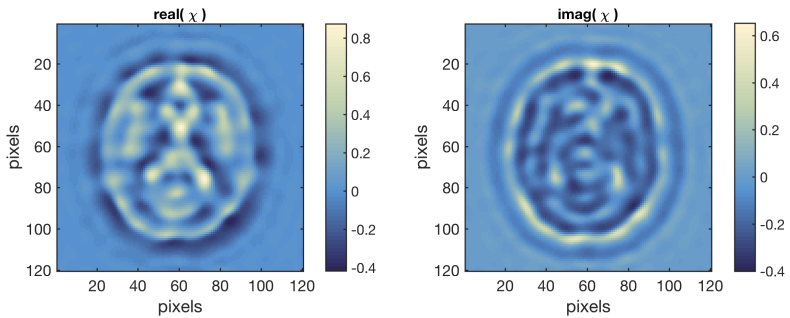


Figure 7.45: Result of a CSI reconstruction with a setup containing a realistic head phantom. The phantom was derived from MRI images. For the simulation as well as the reconstruction a frequency of 1.0GHz was used. A few physiologic structures are clearly observable (compare also Figure 7.35).

An Artificial Hemorrhage Inside the Realistic Head Phantom As a final experiment with the realistic head model and also due to the fact that on a later state a stroke diagnosis should be possible the setup was supplemented with an artificial hemorrhage, as described in section 7.3.5.3. Therefore a circular section of the brain was replaced by the permittivity of blood. The result of this experiment is visible in Figure 7.46. To exclude

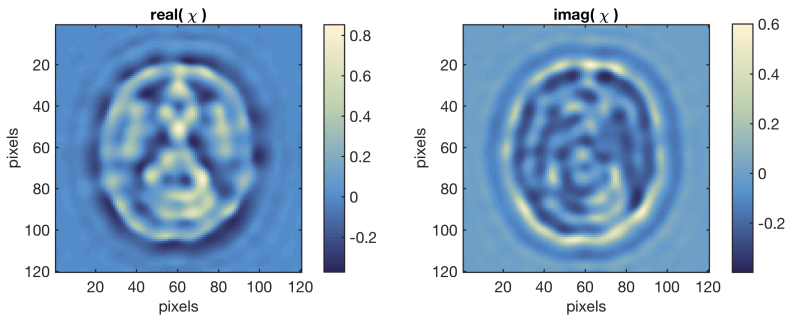


Figure 7.46: Reconstructions on a realistic head model including a hemorrhagic stroke. The setup was simulated at 1.0GHz . The blood is sufficiently visible on both parts of the complex contrast.

side effects and shadows within the reconstruction the difference between this reconstruction and the reconstruction without the stroke was also

observed. Figure 7.47 illustrates this difference. It is clearly observable

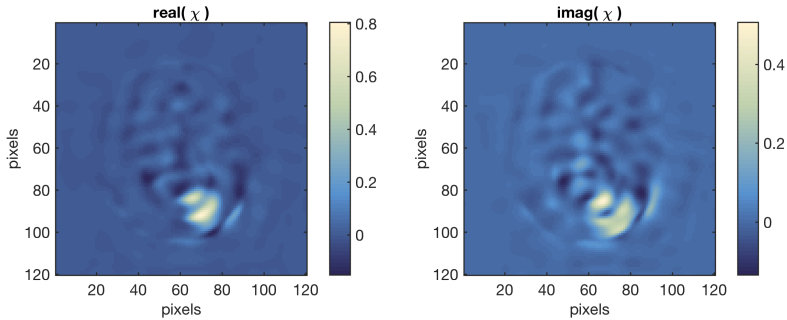


Figure 7.47: The difference between the reconstruction of the setups with the realistic head phantom. One of the setups included an artificial hemorrhage. Except from small artifacts the difference can be found in the high values of the correct location and in the expected spatial expansion.

that the bleeding is in the correct location with almost the exact spatial expansion. However, minor artifacts caused by the algorithm breaking through the stroke region are also visible.

7.3.8.4 Results on Noisy Input Data

Beside numerical errors no errors were considered with the examination so far. As this is impossible if dealing with real measured data the performance of the CSI algorithm was also tested with noisy input data. Thus, the simulated input data was modified by

$$f_{j,l}^{noise} = f_{j,l} + \gamma [r \operatorname{Re}(f_{j,l}) + ir \operatorname{Im}(f_{j,l})], \quad (7.82)$$

where r stands for a random value between -1 and 1 , and γ denotes a determinable value controlling the fractal proportion of the noise. Figure 7.48 shows the results for the input data with up to 20% additional noise. Surprising was the fact that there was almost no difference between the final result obtained by the CSI method and the final results the MR-CSI algorithm yielded. We assumed that somehow the results described a distribution that really solved the problem and that therefore the influence of the regularization term vanished in the end.

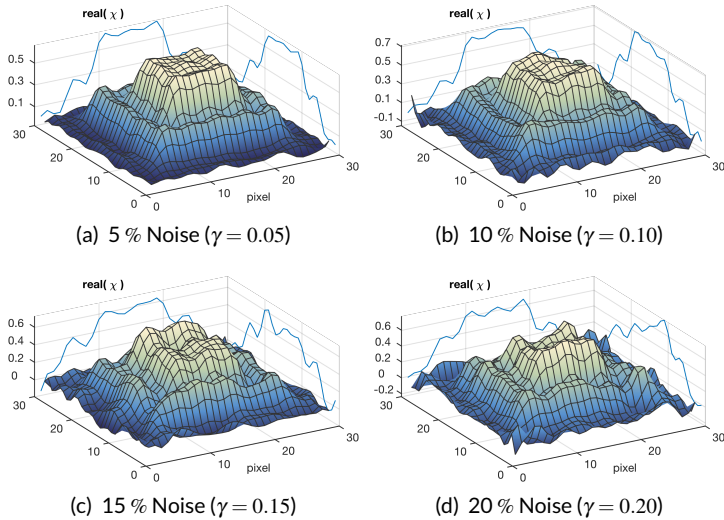


Figure 7.48: Results when noise was added to the input values f . The images were reconstructed by using the CSI algorithm at 0.5 GHz .

7.3.8.5 Improvements Obtained with Frequency Hopping

Due to the simple structure of the concentric squares object it is an ideal test subject for further examinations. Hence, it was selected to examine the benefit of frequency hopping. Therefore the well-known setup up was reconstructed with 0.3 GHz . After that the frequency hopping was performed with a first step of 0.2 GHz and afterwards a step of 0.3 GHz up to a last frequency of 1.0 GHz . The obtained results of 0.7 GHz and 1.0 GHz are illustrated in Figure 7.49. What was clearly observable was the fact that the results were by far better than without the initial guess of the previous reconstruction. Not as clear as that but still observable was the fact that the results also improved with the spatial resolution. However, as mentioned before, this procedure is only possible if the fields were taken from simulations, made between every hop. As this is linked to a simulation consuming high resources (which is especially true if the simulation should be compared to real measurements) this will compensate the main benefit of the method: Simulations containing for example a

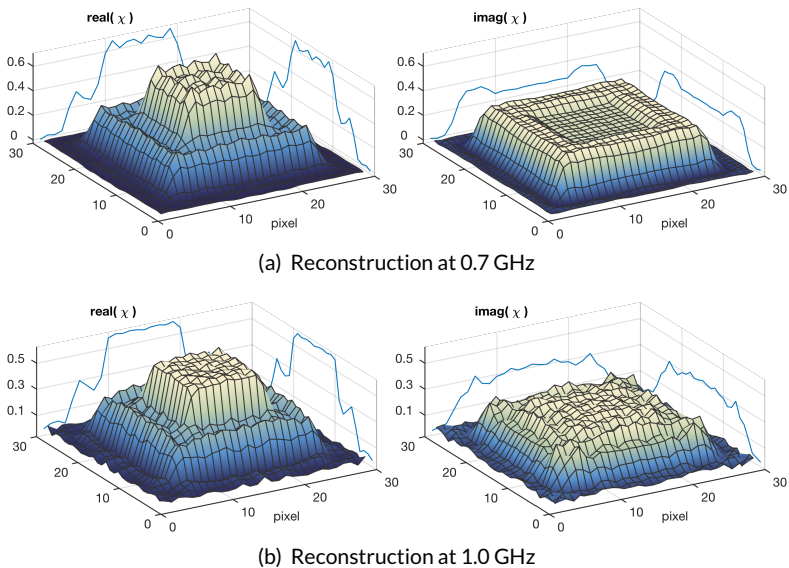


Figure 7.49: Frequency hopping results of the MR-CSI algorithm with the concentric squares object. The results are significantly improved if compared to the direct reconstruction in higher frequencies. However, the necessary simulation between the hops consume all the benefit of the method (compare also Figure 7.38).

complete antenna array need hours even with fast cluster computers. Since only the final image (achieved by the highest frequency) is needed, it is possible that a good initial guess with a predefined model would probably reach similar improvements for higher frequencies.

7.3.9 Time is Brain

As doctors keep to say *time is brain* the performance of the algorithm is an important feature. This was the reason for us to examine the performance, too. As mentioned before some of the routines were parallelized to improve performance.

By utilizing the profiling function provided by MATLAB a speed test of the algorithm was made. The results achieved can be observed in Table 7.4. Due to the huge number of iterations necessary to reach these results

Table 7.4: The speed of the algorithm. Naturally, the MR-CSI algorithm takes significantly longer per iteration as the pure CSI algorithm. Due to performance declines from overhead communications the concentric squares model and the simple head phantom needed almost the same time per iteration even despite of the different image sizes. The frequency for which the image was reconstructed had no remarkable impact on the timings. (The size of the domain D is expressed in voxels and the unit of the time is seconds)

| Model | Domain D | Algorithm | Time/Iteration |
|-----------------------|------------------|-----------|----------------|
| Concentric Squares | 29×29 | CSI | 0.1862 |
| | | MR-CSI | 0.2423 |
| Simple Head Phantom | 45×45 | CSI | 0.1894 |
| | | MR-CSI | 0.2486 |
| Advanced Head Phantom | 120×120 | CSI | 0.6587 |
| | | MR-CSI | 0.8633 |

(at best 5000 for the realistic head model), a reconstruction took nearly an hour in total.

7.3.10 Stroke Imaging Using Contrast Source Inversion?

When looking at the results it is obvious that there is still a gap between the reconstructions of real measurements and the examples presented here. However, due to the enormous performance compared to the other examined reconstruction algorithms this seems to be the most promising approach to reach a successful stroke diagnosis. Better hardware and a performant implementation, together with a clever way of integrating the antennas could lead to sufficient and fast enough results.

Conclusion

A significant step in the direction of microwave stroke imaging was done. This work presents a wide range of algorithms related to this topic. All of them were implemented and tested for their ability of diagnosing strokes. Only one possibility of solving the problem was not addressed: The one Person et al. mentioned in the Strokefinder project [59]. They used a computer learning algorithm to diagnose strokes. However, this was not possible for our research team because a huge amount of data sets would have been necessary for training those algorithms. In addition to that it is hard to show that those algorithms always deliver good results which is especially true for neuronal networks.

However, the findings show that a stroke diagnostic with all implemented algorithms would be possible even if some of them had been excluded because they were either not robust or the computational effort was too large.

In the end I came to the conclusion that only the contrast source inversion algorithm sufficiently fulfilled all requirements. The algorithm was capable of imaging coarse objects inside the head and it delivered sufficient results after an acceptable time. The algorithm was also able to reconstruct full three-dimensional regions and it was able to reconstruct the two-dimensional slices within an hour. Finally I think that an improvement of the performance can be reached by a parallel calculation on GPUs. Here

it must be mentioned that all introduced algorithms were implemented on a basic status.

For example, there were many improvements intended for the DAS algorithm by other authors. Some of them suggested to remove the reflections from the skin or others wanted to improve the robustness. However, due to the spatial expansion of the signals and the poor results I obtained under nearly ideal conditions I excluded these types of algorithms.

By looking at the implemented Gauss-Newton-Algorithm the setup up does still need some modifications. For example, until now real antennas have not been integrated and the algorithm is only implemented for two-dimensional problems. However, we should keep in mind that when switching to a three-dimensional setup the number of unknowns will grow significantly. But even if these drawbacks were compensated by defining fewer and bigger areas, where the permittivity should be changed, the simulation time would significantly increase by switching to full 3D simulations. This is a disadvantage that does not commonly exist for the CSI algorithm, as there the 2D Green's function can be simply replaced by the 3D fundamental solution of a point source. This, in combination with an antenna with a flat radiation pattern (e.g. a vivaldi antenna), probably makes a reconstruction of a single 2D slice of the observed 3D scene possible. Unfortunately, due to the spherical spreading of 3D waves the attenuation will be stronger and therefore even more iterations will be necessary for sufficient results.

Finally, I believe that a major step towards stroke diagnosis via microwave imaging was reached with this work. The CSI algorithm and its good performance is the best candidate for further investigations and is the one able to facilitate a fast, reliable and transparent stroke diagnosis. By finding a sufficient resolution in combination with ideal hardware the necessary performance to compute results within minutes would be reachable. As such a device could greatly improve the clinical outcome of victims suffering from a stroke, a further development is recommended.

Outlook

Now, the question of interest is how could this project be continued? This question is easy to answer. To continue the project the next step would be to integrate the antennas into the CSI algorithm and reconstruct two-dimensional slices from 3D simulations.

I intended to use multiple point sources mimicking a real antenna. The superposition of those point sources can then generate a field similar to the one the antenna would provide. Beside that this would also be a suitable solution for the Gauss-Newton-Algorithm. The benefit for this algorithm would be that no antennas, which contain small metallic parts, would be present and therefore the forward calculations would be fast.

Replacing Antennas by Point Sources A small pre-study was made to examine whether a few point sources can sufficiently represent the field of a complex antenna. To examine this, a CST simulation with a single Vivaldi antenna was made and the field was exported. By using 15 point sources the field was reconstructed. Figure 9.1 shows the reconstructed field in the right image and the residual between the simulated and the reconstructed field in the left image.

To achieve this result, a quasi-newton optimization algorithm was used to fit the complex amplitudes as well as the positions of the source. To prevent the sources from drifting too far, an additive penalty term was used.

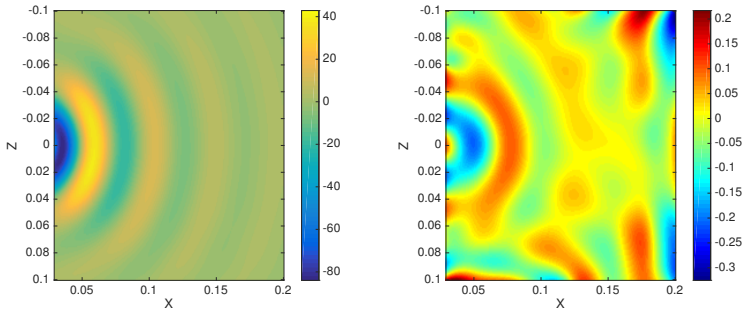


Figure 9.1: Results of an optimization performed by a Quasi-Newton method. The images show a combination of point sources. The original field was taken from an FDTD-simulation performed by Microwave Studio from CST. The left image shows the reconstructed field and the right image the residual field.

This was done by selecting a point on the antenna and then calculating the differences \mathbf{d} between this point and the actual points of the sources. They were included in an L_2 -norm punishing term. The term was weighted

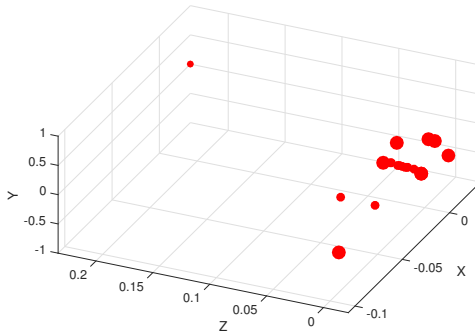


Figure 9.2: The resulting distribution of the point sources. The size of the dots are scaled by the absolute values of the complex amplitude.

with the squared value of the current residuum. Hence, the influence grew smaller with the decreasing residuum. The distribution of the sources can be observed in Figure 9.2.

Here it should be mentioned that for the CSI algorithm even simulated fields could be used instead of fields reproduced by point sources. However, studies showed that the reconstructions with simulated fields were not as good as those with analytic fields.

Anyhow, the integration of these features has not been completed until today.

A Flexible and Easy Extendable Framework One last thing should be mentioned here: I am convinced that further developments of those algorithms can profit from a framework containing all parts of all the implemented methods as this would enable the user to combine the findings and develop any kind of hybrid algorithms. For example, a simulation between reconstructions with the CSI algorithm can be used to calculate the fields, such as it was done for the frequency hopping test. When using the Gauss-Newton approach the calculation of the full Jacobi matrix in each iteration would be avoidable by the findings of the CSI algorithm.

For this purpose a flexible and easily extendable framework was developed. The framework was a product of the bachelor thesis of Andreas Baumeister [60].

The framework encapsulates the functionality of the algorithms included into logical-nodes. It also provides a structure to load and to distribute data over multiple computation nodes. The concept of the logical-node enables a modular development of algorithms. Additionally, the developed algorithm can be easily rearranged without modifying the interfaces. It must be mentioned that until now, only the DAS algorithm is already integrated.

Final Thoughts A parametrizable head model could possibly be used to minimize the number of free parameters and therefore minimize the number of iterations in the Gauss-Newton-Algorithm. The head model could also be used for an investigation of a fitting scenario with the DAS-algorithm to minimize the reflections of the known head morphology. It could also be used to calculate a good initial guess for a higher frequency when using the CSI or MR-CSI. Thus, in my opinion, another path that should be followed is the development of such a model.

Finally, a pending task would be to develop antennas with a better isolation between each other because this would reduce mutual coupling and improve the spatial resolution.

The mentioned developments are by far not all possible ways to go. This only shows that this project is still in an early state of development.

The Complex Root of the Permittivity

To separate the root of the complex permittivity into the imaginary and the real part the complex number is written in different representations:

$$\underline{\varepsilon}_r = \varepsilon' - j\varepsilon'' = |\underline{\varepsilon}_r| \cdot (\cos(\arg\{\underline{\varepsilon}_r\}) + j \sin(\arg\{\underline{\varepsilon}_r\})) = |\underline{\varepsilon}_r| \cdot e^{j \arg\{\underline{\varepsilon}_r\}} \quad (\text{A.1})$$

We start with the polar representation. There it is easy to understand that the square-root is simply the square-root of the absolute value of the complex permittivity and its argument is the half of the original argument:

$$\sqrt{\underline{\varepsilon}_r} = \sqrt{|\underline{\varepsilon}_r|} \cdot e^{j \frac{\arg\{\underline{\varepsilon}_r\}}{2}} \quad (\text{A.2})$$

We can use that now to write the square-root in the Euler form:

$$\sqrt{\underline{\varepsilon}_r} = \sqrt{|\underline{\varepsilon}_r|} \cdot \left(\cos\left(\frac{\arg\{\underline{\varepsilon}_r\}}{2}\right) + j \sin\left(\frac{\arg\{\underline{\varepsilon}_r\}}{2}\right) \right) \quad (\text{A.3})$$

In general the argument of a complex number can be calculated by the arc tangent but the right quadrant has to be chosen. We know that the imaginary part is always negative and the real part is always positive as well as larger than one. That is true for nearly all the materials. This means

that we can use

$$\arg\{\underline{\varepsilon}_r\} = \arctan\left\{\frac{-\varepsilon''}{\varepsilon'}\right\} = -\arccos\left\{\frac{1}{\sqrt{1 + \left(\frac{\varepsilon''}{\varepsilon'}\right)^2}}\right\} = -\pi + \arccos\left\{-\frac{\varepsilon'}{|\underline{\varepsilon}_r|}\right\} \quad (\text{A.4})$$

to calculate the argument of $\underline{\varepsilon}_r$. At this point we can use the half-angle formulas

$$\sin \frac{\alpha}{2} = \pm \sqrt{\frac{1 - \cos(\alpha)}{2}} \quad (\text{A.5})$$

$$\cos \frac{\alpha}{2} = \pm \sqrt{\frac{1 + \cos(\alpha)}{2}}$$

to replace the argument at (A.3) and set (A.4) for α . The sign of the root depends on the quadrant, too. In our case we achieve:

$$\sqrt{\underline{\varepsilon}_r} = \sqrt{|\underline{\varepsilon}_r|} \cdot \left(\sqrt{\frac{1}{2} \cdot \left(1 + \frac{\varepsilon'}{|\underline{\varepsilon}_r|}\right)} - j \sqrt{\frac{1}{2} \cdot \left(1 - \frac{\varepsilon'}{|\underline{\varepsilon}_r|}\right)} \right) \quad (\text{A.6})$$

or

$$\sqrt{\underline{\varepsilon}_r} = \sqrt{\frac{1}{2} \cdot (|\underline{\varepsilon}_r| - \varepsilon')} - j \sqrt{\frac{1}{2} \cdot (|\underline{\varepsilon}_r| + \varepsilon')}. \quad (\text{A.7})$$

The G Operators of CSI

The operator

$$Go_j(p) = k_b^2 \int_D g(p, q) o_j(p) dv \quad (\text{B.1})$$

of the Contrast Source Inversion (CSI) method can be used to determine the field at a point $p \in \{D \cup S\}$, generated by the contrast sources o_j in the domain D . Since it uses the Green's function of the background medium it can be thought that the wave propagation is caused by the sources when no other medium is present.

Depending on whether the point p lies in the object domain D or the measurement domain S the operator G will be called G_D and G_S respectively.

The Green's functions for a homogeneous infinite background medium with the wavenumber k_b in two and three dimensions can be written as [61, p. 295]

$$\text{2D: } g(p, q) = -\frac{i}{4} H_0^{(1)}(k_b |p - q|)$$

$$\text{3D: } g(p, q) = -\frac{\exp(ik_b |p - q|)}{4\pi |p - q|}.$$

In the two-dimensional case $H_0^{(1)}$ stands for the zero-order Bessel function of the first kind (which is a solution to the Bessel equation [61, p. 46]).

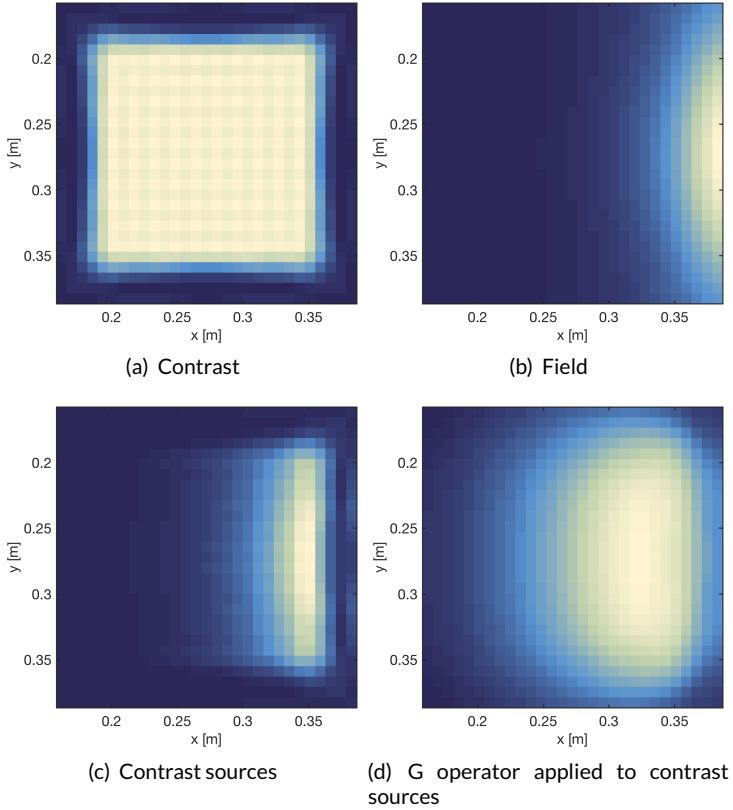


Figure B.1: Demonstration of the G_D operator. All images show the absolute values of the respective functions: (a) A contrast distribution inside the object domain. (b) The field generated by antenna 1 at the right side of the object domain. (c) The contrast sources obtained by $\rho_1 = \chi E_1$. (d) The result of applying the G_D operator to the contrast sources, $G_D \rho_1$.

An example of how the G operator works is given in Figure B.1.

For this algorithm, the adjoint operators for G_D and G_S are also needed. These can be calculated by [54]:

$$(G_S^* \rho_j)(p) = k_b^2 \int_S \overline{G(p, q)} \rho_j(q) dv \quad p \in D \quad (\text{B.2})$$

$$(G_D^* \phi_j)(p) = k_b^2 \int_D \overline{G(p, q)} \phi_j(q) dv \quad p \in D. \quad (\text{B.3})$$

The G_S^* operator is used to transform its input from the data domain S to the object domain D , whereas the G_D^* operator converts an input from the object domain to the same domain.

B.1 Calculation Time

A run-time analysis of the code showed that in each iteration most of the time is spent on calculating the G_D and G_D^* operators. This is why decreasing the cost of calculating these operators would benefit the reconstruction time as well.

We note that the Green's function both in 2D and 3D only contains the difference between its arguments p and q . Thus, we could also use the notation

$$G(p, q) = G(p - q). \quad (\text{B.4})$$

When using this it can be seen that the operators contain a convolution. For example, the G_D operator is now changed to¹

$$G_D o_j(p) = k_b^2 \int_D G(p - q) o_j(p) dv \quad (\text{B.5})$$

$$= k_b^2 G(p) * o_j(p). \quad (\text{B.6})$$

Using the *convolution theorem* the convolution can be calculated in the frequency domain:

$$\mathcal{F}\{u * v\} = \mathcal{F}\{u\} \mathcal{F}\{v\} \quad (\text{B.7})$$

$$u * v = \mathcal{F}^{-1}\{\mathcal{F}\{u\} \mathcal{F}\{v\}\} \quad (\text{B.8})$$

¹This can also be applied to the other operators in the same way

where $\mathcal{F}\{\cdot\}$ denotes the Fourier transform and $\mathcal{F}^{-1}\{\cdot\}$ denotes the inverse Fourier transform. Since in the frequency domain the convolution is replaced by a multiplication it can be calculated much faster.

As an example applying this to the G_D operator it yields:

$$G_D o_j(p) = k_b^2(G(p) * o_j(p)) \quad (\text{B.9})$$

$$= k_b^2 \mathcal{F}^{-1}\{\mathcal{F}\{G(p)\} \mathcal{F}\{o_j(p)\}\} \quad (\text{B.10})$$

To use this method the input vector o_j as well as the Green's function $G(p, q)$ must be Fourier-transformed. The latter does not change during the reconstruction so that its Fourier transform can be calculated once at the start. The input vector needs to be Fourier-transformed in each iteration which is done by using the FFT. Both the G_D and the G_D^* operators are calculated in the frequency domain which greatly decreased their calculation times.

Differentiation of the MR Term

In this section, the derivation of the Multiplicative Regularization (MR) term $F_R(\chi)$ is described. Since this term is a functional (because χ is a function of the position p) methods from the calculus of variations will be used. More specifically, the Euler-Lagrange equation will be used to find the derivative of the functional $F_R(\chi)$ with respect to χ .

We start by moving the constant volume V into the denominator of the fraction inside the integral. Afterwards, the denominator can be replaced with W because it can be considered constant. This is valid as it only depends on the constant χ_n which has already been found and will not change any more. The replacement makes the following notations simpler.

$$F_R(\chi) = \frac{1}{V} \int_D \frac{|\nabla\chi(p)|^2 + \delta_n^2}{|\nabla\chi_n(p)|^2 + \delta_n^2} dv \quad (\text{C.1})$$

$$= \int_D \frac{|\nabla\chi(p)|^2 + \delta_n^2}{W} dv \quad (\text{C.2})$$

As a next step the absolute value is rewritten with the inner product (as $\|\cdot\|^2 = \langle \cdot, \cdot \rangle$). Since we work in the two-dimensional case the gradient operator ∇ denotes a vector of two partial derivatives, in x and y directions:

$$F_R(\chi) = \int_D \frac{\left\| \begin{bmatrix} \frac{\partial \chi}{\partial x} \\ \frac{\partial \chi}{\partial y} \end{bmatrix} \right\|^2 + \delta_n^2}{W} dv \quad (C.3)$$

Now the inner product is evaluated:

$$F_R(\chi) = \int_D \frac{(\frac{\partial \chi}{\partial x})^2 + (\frac{\partial \chi}{\partial y})^2 + \delta_n^2}{W} dv \quad (C.4)$$

This functional is of the form

$$F(\chi) = \int L(x, y, \chi, \chi_x, \chi_y) dv \quad (C.5)$$

where χ_x and χ_y are the partial derivatives of χ with respect to x and y . In this notation the function χ and its partial derivatives are treated like variables of L .

According to the Euler-Lagrange equation the derivative of the functional $F_R(\chi)$ can then be written as

$$\frac{\partial F_R(\chi)}{\partial \chi} = \frac{\partial L}{\partial \chi} - \frac{\partial}{\partial x} \frac{\partial L}{\partial \chi_x} - \frac{\partial}{\partial y} \frac{\partial L}{\partial \chi_y}. \quad (C.6)$$

As L does not directly depend on χ , the term $\partial L / \partial \chi$ is zero. For the other two adds the derivatives of L with respect to the partial derivatives of χ are required:

$$\frac{\partial L}{\partial \chi_x} = \frac{\partial}{\partial \chi_x} \left(\frac{(\frac{\partial \chi}{\partial x})^2 + (\frac{\partial \chi}{\partial y})^2 + \delta_n^2}{W} \right) = \frac{2 \left(\frac{\partial \chi}{\partial x} \right)}{W} \quad (C.7)$$

$$\frac{\partial L}{\partial \chi_y} = \frac{\partial}{\partial \chi_y} \left(\frac{(\frac{\partial \chi}{\partial x})^2 + (\frac{\partial \chi}{\partial y})^2 + \delta_n^2}{W} \right) = \frac{2 \left(\frac{\partial \chi}{\partial y} \right)}{W} \quad (C.8)$$

Lastly, according to equation (C.6), the first of these equations needs to be derived with respect to x and the second with respect to y . This results in

$$\frac{\partial F_R(\chi)}{\partial \chi} = -2 \left(\frac{\frac{\partial^2 \chi}{\partial x^2} + \frac{\partial^2 \chi}{\partial y^2}}{W} \right). \quad (\text{C.9})$$

The numerator of this ratio is simply the Laplace operator of the contrast, $\Delta\chi$, which can be written as $\Delta = \nabla\nabla$. Doing this leads to the form which is used in the description of the algorithm in section 7.3.2.3:

$$\frac{\partial F_R(\chi)}{\partial \chi}(p) = -2\nabla \left[\frac{\nabla\chi(p)}{W} \right]. \quad (\text{C.10})$$

The difference between this function and the one used by the authors in the CSI algorithm (equation (7.67)) is the constant factor of -2 . Since the derivative found here is used in a line search where the updated step-size is β_R , we can assume that β_R will contain the factor and if neglected it will not change the final results.

References

- [1] G. Herold and et al., *Innere Medizin*. Dr. med. Gerd Herold, 2015.
- [2] L. J. Broome, C. E. Battle, M. Lawrence, et al., “Cognitive outcomes following thrombolysis in acute ischemic stroke: a systematic review,” *Journal of Stroke and Cerebrovascular Diseases*, pp. 1052–3057, 2016.
- [3] World Health Organization. The top 10 causes of death. Internet: <http://www.who.int/mediacentre/factsheets/fs310/en>, 2012 [2016-08-31].
- [4] M. Persson, A. Fhager, H. D. Trefná, et al., “Microwave-based stroke diagnosis making global prehospital thrombolytic treatment possible,” *IEEE Transactions on Biomedical Engineering*, vol. 61, no. 11, pp. 2806–2817, 2014.
- [5] Micrima Limited. Micrima Limited Homepage. Internet: <http://www.micrima.com>, 2016 [2016-08-31].
- [6] B. Mohammed, A. Abbosh, B. Henin, et al., “Head phantom for testing microwave systems for head imaging,” *2012 Cairo International Biomedical Engineering Conference (CIBEC)*, pp. 191–193, 2012.
- [7] D. Griffiths, *Introduction to Electrodynamics*, Always learning. Pearson, 2013.
- [8] K. S. Yee et al., “Numerical solution of initial boundary value problems involving Maxwell’s equations in isotropic media,” *IEEE Trans. Antennas Propag*, vol. 14, no. 3, pp. 302–307, 1966.
- [9] M. Chari and S. Salon, Eds., *Numerical Methods in Electromagnetism*, Electromagnetism. San Diego: Academic Press, 2008.
- [10] W. Sun, K. Liu, and C. A. Balanis, “Analysis of singly and doubly periodic absorbers by frequency-domain finite-difference method,” *IEEE Transactions on Antennas and Propagation*, vol. 44, no. 6 PART 1, pp. 798–805, 1996.

- [11] R. C. Rumpf, "Simple implementation of arbitrarily shaped total-field/scattered-field regions in finite-difference frequency-domain," *Progress In Electromagnetics Research B*, vol. 36, pp. 221–248, 2012.
- [12] D. Colton, *Inverse Acoustic and Electromagnetic Scattering Theory*, 3rd ed., Applied Mathematical Sciences, R. Kress, Ed. New York, NY: Springer, 2013.
- [13] S. Eisová, G. Rangel de Lázaro, H. Pířová, et al., "Parietal bone thickness and vascular diameters in adult modern humans: a survey on cranial remains," *The Anatomical Record*, vol. 299, no. 7, pp. 888–896, 2016.
- [14] M. F. Bear, B. W. Connors, and M. A. Paradiso, *Neurowissenschaften: Ein grundlegendes Lehrbuch für Biologie, Medizin und Psychologie*, 3rd ed., A. K. H. Engel, Ed. Heidelberg: Spektrum Akademischer Verlag, 2009.
- [15] C. Francks, *Genetics of left-right differences in the brain*. Max Planck Institute for Psycholinguistics, 2015.
- [16] R. v. H. Kummer and T. H. Back, *Magnetic Resonance Imaging in Ischemic Stroke*, Medical Radiology, Diagnostic Imaging. Berlin, Heidelberg: Springer Berlin Heidelberg, 2006.
- [17] G. Schmid, G. Neubauer, U. M. Illievich, et al., "Dielectric properties of porcine brain tissue in the transition from life to death at frequencies from 800 to 1900 MHz." *Bioelectromagnetics*, vol. 24, no. 6, pp. 413–22, 2003.
- [18] E. C. Burdette, P. G. Friederich, R. L. Seaman, et al., "In situ permittivity of canine brain: regional variations and postmortem changes," *IEEE Transactions on Microwave Theory and Techniques*, vol. 34, no. 1, pp. 38–50, 1986.
- [19] G. Schmid, G. Neubauer, and P. R. Mazal, "Dielectric properties of human brain tissue measured less than 10 h postmortem at frequencies from 800 to 2450 MHz," *Bioelectromagnetics*, vol. 24, no. 6, pp. 423–430, 2003.
- [20] J. Nocedal and S. J. Wright, *Numerical optimization*, 2nd ed., Springer series in operation research and financial engineering. New York, NY: Springer, 2006.
- [21] R. Penrose, "A generalized inverse for matrices," *Mathematical Proceedings of the Cambridge Philosophical Society*, vol. 51, no. 3, pp. 406–413, 1955.
- [22] P. Hasgall, F. Di Gennaro, C. Baumgartner, et al. IT'IS Database for thermal and electromagnetic parameters of biological tissues. Version 3.0, Internet: <http://www.itis.ethz.ch/virtual-population/tissue-properties/>, 2015 [2015-08-21] DOI: 10.13099/VIP21000-03-0.

-
- [23] C. C. Marzi, "Entwicklung von Phantomen des menschlichen Kopfes zur experimentellen Verifikation von UWB-Mikrowellen-basierten-Diagnose-Systemen," Master's thesis, Institute of Biomedical Engineering, Karlsruhe Institute of Technology (KIT), 2014.
- [24] N. Bauer, "Verifikation und Optimierung eines Gelatine-Zucker-basierten Kopfphantoms für die mikrowellenbasierte Bildgebung," Master's thesis, Institut für Biomedizinische Technik, Karlsruher Institut für Technologie (KIT), Karlsruhe, 2015.
- [25] C. Marchal, M. Nadi, a. J. Tosser, et al., "Dielectric properties of gelatine phantoms used for simulations of biological tissues between 10 and 50 MHz," *International journal of hyperthermia : the official journal of European Society for Hyperthermic Oncology, North American Hyperthermia Group*, vol. 5, no. 6, pp. 725–732, 1989.
- [26] K. M. Chew, R. Sudirman, N. Seman, et al., "Human brain phantom modeling: concentration and temperature effects on relative permittivity," *Advanced Materials Research*, vol. 646, pp. 191–196, 2013.
- [27] R. A. Parker, "Static dielectric constant of rutile (TiO₂), 1.6–1060° K," *Phys. Rev.*, vol. 124, pp. 1719–1722, 1961.
- [28] L. Ramajo, M. Reboredo, and M. Castro, "Dielectric response and relaxation phenomena in composites of epoxy resin with BaTiO₃ particles," *Composites Part A: Applied Science and Manufacturing*, vol. 36, no. 9, pp. 1267–1274, 2005.
- [29] B. Riddle, J. Baker-Jarvis, and J. Krupka, "Complex permittivity measurements of common plastics over variable temperatures," *IEEE Transactions on Microwave Theory and Techniques*, vol. 51, no. 3, pp. 727–733, 2003.
- [30] F. Ciuprina, T. Zaharescu, S. Jipa, et al., "Dielectric properties and thermal stability of Îš-irradiated inorganic nanofiller modified {PVC} ," *Radiation Physics and Chemistry*, vol. 79, no. 3, pp. 379–382, 2010.
- [31] M. Jalilvand, X. Li, J. Kowalewski, et al., "Broadband miniaturised bow-tie antenna for 3D microwave tomography," *Electronics Letters*, vol. 50, no. 4, pp. 244–246, 2014.
- [32] E. Zastrow, S. C. Hagness, B. D. V. Veen, et al., "Time-multiplexed beamforming for noninvasive microwave hyperthermia treatment," *IEEE Transactions on Biomedical Engineering*, vol. 58, no. 6, pp. 1574–1584, 2011.
- [33] E. J. Bond, X. Li, S. C. Hagness, et al., "Microwave imaging via space-time beamforming for early detection of breast cancer," *IEEE Transactions on Antennas and Propagation*, vol. 51, no. 8, pp. 1690–1705, 2003.

- [34] M. Jalilvand, X. Li, T. Zwick, et al., “Hemorrhagic stroke detection via UWB medical imaging,” in *Proc. 5th Eur. Conf. Antennas and Propagation*, 2011.
- [35] X. Li, M. Jalilvand, Y. L. Sit, et al., “A compact double-layer on-body matched bowtie antenna for medical diagnosis,” *IEEE Transactions on Antennas and Propagation*, vol. 62, no. 4, pp. 1808–1816, 2014.
- [36] M. Jalilvand, X. Li, J. Kowalewski, et al., “Broadband miniaturised bow-tie antenna for 3D microwave tomography,” *Electronics Letters*, vol. 50, no. 4, pp. 244–246, 2014.
- [37] T. Rubaek, P. M. Meaney, P. Meincke, et al., “Nonlinear microwave imaging for breast-cancer screening using Gauss-Newton’s method and the CGLS inversion algorithm,” *IEEE Trans. Antennas Propag.*, vol. 55, no. 8, pp. 2320–2331, 2007.
- [38] Massachusetts Institute of Technology. Meep acronym expansions. Internet: http://ab-initio.mit.edu/wiki/index.php/Meep_acronym_expansions, 2016 [2016-09-21].
- [39] A. F. Oskooi, D. Roundy, M. Ibanescu, et al., “MEEP: A flexible free-software package for electromagnetic simulations by the FDTD method,” *Computer Physics Communications*, vol. 181, pp. 687–702, 2010.
- [40] S. Balay, S. Abhyankar, M. F. Adams, et al. PETSc Web page. Internet: <http://www.mcs.anl.gov/petsc>, 2016 [2016-09-21].
- [41] S. Balay, S. Abhyankar, M. F. Adams, et al., “PETSc Users Manual,” Argonne National Laboratory, Tech. Rep. ANL-95/11 - Revision 3.7, 2016.
- [42] S. Balay, W. D. Gropp, L. C. McInnes, et al., “Efficient management of parallelism in object oriented numerical software libraries,” in *Modern Software Tools in Scientific Computing*, E. Arge, A. M. Bruaset, and H. P. Langtangen, Eds. Birkhäuser Press, 1997, pp. 163–202.
- [43] B. Schäling, *The Boost C++ libraries : a quickstart introduction with over 250 examples*, 1st ed. Laguna Hills, Calif.: XML Press, 2011.
- [44] M. Jalilvand, C. Wu, J. Schmid, et al., “Quantitative imaging of numerically realistic human head model using microwave tomography,” *Electronics Letters*, vol. 50, no. 4, pp. 255–256, 2014.
- [45] F. B. Sachse, C. Werner, M. Müller, et al., “Segmentation and tissue-classification of the visible man dataset using the computertomographic scans and the thin-section photos,” in *in Proc. First Users Conference of the National Library of Medicine’s Visible Human Project*, 1996, pp. 125–126.

-
- [46] M. Pfeiffer, “Investigation of the contrast source inversion method for microwave brain tomography,” Master’s thesis, Institute of Biomedical Engineering, Karlsruhe Institute of Technology (KIT), 2016.
- [47] P. Furlan, *Das gelbe Rechenbuch*, [nachdr.] ed., 3: Gewöhnliche Differentialgleichungen, Funktionentheorie, Integraltransformationen, partielle Differentialgleichungen. Dortmund: Furlan, 2008.
- [48] N. Joachimowicz, C. Pichot, and J. P. Hugonin, “Inverse scattering: an iterative numerical method for electromagnetic imaging,” *IEEE Transactions on Antennas and Propagation*, vol. 39, no. 12, pp. 1742–1753, 1991.
- [49] S. Geršgorin, “Über die Abgrenzung der Eigenwerte einer Matrix,” *Bulletin de l’Académie des Sciences de l’URSS. Classe des sciences mathématiques et na*, no. 6, pp. 749–754, 1931.
- [50] P. M. van den Berg and R. E. Kleinman, “A contrast source inversion method,” *Inverse Problems*, vol. 13, no. 6, p. 1607, 1997.
- [51] R. Chandra, H. Zhou, I. Balasingham, et al., “On the opportunities and challenges in microwave medical sensing and imaging,” *IEEE Transactions on Biomedical Engineering*, vol. 62, no. 7, pp. 1667–1682, 2015.
- [52] A. Abubakar and P. M. van den Berg, “A total variation enhanced contrast source inversion method for three-dimensional profile reconstruction,” *Proc. ECCOMAS 2000, Book of Abstracts*, pp. 11–14, 2002.
- [53] A. Abubakar, P. M. van den Berg, and J. J. Mallorqui, “Imaging of biomedical data using a multiplicative regularized contrast source inversion method,” *IEEE Transactions on Microwave Theory and Techniques*, vol. 50, no. 7, pp. 1761–1771, 2002.
- [54] P. van den Berg and A. Abubakar, “Contrast source inversion method: state of art,” *Journal of Electromagnetic Waves and Applications*, vol. 15, no. 11, pp. 1503–1505, 2001.
- [55] P. M. van den Berg, A. Abubakar, and J. T. Fokkema, “Multiplicative regularization for contrast profile inversion,” *Radio Science*, vol. 38, pp. VIC–23, 2003.
- [56] M. Lustig, D. Donoho, and J. M. Pauly, “Sparse MRI: the application of compressed sensing for rapid MR imaging,” *Magnetic Resonance in Medicine*, vol. 58, no. 6, pp. 1182–1195, 2007.
- [57] M. Ostadrahimi, P. Mojabi, C. Gilmore, et al., “Analysis of incident field modeling and incident/scattered field calibration techniques in microwave tomography,” *IEEE Antennas and Wireless Propagation Letters*, vol. 10, pp. 900–903, 2011.

- [58] E. Michel, D. Hernandez, and S. Y. Lee, "Electrical conductivity and permittivity maps of brain tissues derived from water content based on T1-weighted acquisition," *Magnetic Resonance in Medicine*, 2016, Available: <http://dx.doi.org/10.1002/mrm.26193> [2016-09-22].
- [59] M. Persson, A. Fhager, H. D. Trefna, et al., "Microwave-based stroke diagnosis making global prehospital thrombolytic treatment possible," *IEEE Transactions on Biomedical Engineering*, vol. 61, no. 11, pp. 2806–2817, 2014.
- [60] A. Baumeister, "Konzeption und Analyse eines erweiterbaren, skalierbaren und modularen Frameworks fur die Mikrowellen-Bildgebung," Master's thesis, Institut fur Biomedizinische Technik, Karlsruher Institut fur Technologie (KIT), 2016.
- [61] M. N. O. Sadiku, *Numerical Techniques in Electromagnetics*, 2nd ed. Boca Raton, Florida: CRC Press, 2001.

List of Publications and Supervised Theses

Journal Articles

- M. Jalilvand, C. Wu, **J. Schmid**, T. Zwick *Quantitative imaging of numerically realistic human head model using microwave tomography*, Electronics Letters 2014;50:255–256
- T. Oesterlein, **J. Schmid**, S. Bauer, A. Jadidi, C. Schmitt, O. Dössel, A. Luik *Analysis and visualization of intracardiac electrograms in diagnosis and research: Concept and application of KaPAVIE*, Computer Methods and Programs in Biomedicine 2016,127:165–173
- A. Loewe, M. Wilhelms, **J. Schmid**, M. J. Krause, F. Fischer, D. Thomas, E. P. Scholz, O. Dössel, G. Seemann *Parameter estimation of ion current formulations requires hybrid optimization approach to be both accurate and reliable*, In Frontiers in Bioengineering and Biotechnology, 2016;3:209

Refereed Conference Articles

- J. Schmid, O. Dössel, *An Electromagnetic Simulation Environment, to Construct Microwave Imaging Algorithms*, Biomedizinischer Technik 2013;47

- J. Schmid, C. Marzi, V. Lupici-Baltzer, M. Jalilvand, O. Dössel, *Influence of thin non-conducting layers in electromagnetic body-phantoms for imaging radar*, Biomedizinischer Technik 2014;48

Refereed Conference Abstracts

- J. Schmid, O. Dössel, *Toward Radar based Stroke Imaging by Integrating a Prior Knowledge* IEEE Engineering in Medicine and Biology (EMBC), 2015;37
- J. Schmid, N. Bauer, O. Dössel, *Verification of phantom materials and comparison with simulations based on literature data*, Biomedizinischer Technik 2015;49

Supervised Student Theses

- Carl Christian Marzi, *Entwicklung von Phantomen des menschlichen Kopfes zur experimentellen Verifikation von UWB-Mikrowellen-basierten Diagnose-Systemen*, Bachelor Thesis, Institute of Biomedical Engineering, Karlsruhe Institute of Technology (KIT), 2014
- Natalie Bauer, *Verifikation und Optimierung eines Gelatine-Zucker-basierten Kopfphantoms für die mikrowellenbasierte Bildgebung*, Bachelor Thesis, Institute of Biomedical Engineering, Karlsruhe Institute of Technology (KIT), 2014
- Axel Hahn, *Realisierung eines mikrowellenbasierten Tomographie-Systems zur Schlaganfalldiagnose*, Studienarbeit, Institute of Biomedical Engineering, Karlsruhe Institute of Technology (KIT), 2015
- Axel Hahn, *Optimization of the measurement setup and the guessed model of a microwave tomography system for imaging experimental measurement data*, Diplomarbeit, Institute of Biomedical Engineering, Karlsruhe Institute of Technology (KIT), 2015
- Micha Pfeiffer, *Investigation of the Contrast Source Inversion Method for Microwave Brain Tomography*, Master Thesis, Institute of Biomedical Engineering, Karlsruhe Institute of Technology (KIT), 2016

- Andreas Baumeister, *Konzeption und Analyse eines erweiterbaren, skalierbaren und modularen Frameworks für die Mikrowellen-Bildgebung*, Bachelor Thesis, Institute of Biomedical Engineering, Karlsruhe Institute of Technology (KIT), 2016

